Electromagnetic field dark spots

Vernon, Alex

Awarding institution:
King's College London

Electromagnetic field dark spots

Alex J. Vernon

Supervisor: Dr. Francisco Rodríguez-Fortuño

A thesis submitted for the degree of

Doctor of Philosophy

Department of Physics

King's College London

April 2024

Abstract

Due to destructive interference electromagnetic fields contain minima, counterpart to bright maxima. But because light is a vector wave it is rare that all components of a field, for instance the electric field, are completely eliminated in a wave superposition. An entity satisfying $\mathbf{E} = \mathbf{0}$ we call a dark spot and it can only be realised artificially by control of coherent monochromatic interfering fields, yet doing so embeds light with deeply rich topological structures beyond simple scalar dislocation lines. We study the imprints of vector dark spots in this thesis, including two-dimensional (2D) paraxial dark spots, three-dimensional (3D), point-like non-paraxial dark spots and propose a simple technique for their synthesis and position control. More specifically, paraxial dark spots are shown to always carry non-diverging polarisation structures infinitely into the far field (contrary to the universal phenomena of diffraction), point-like dark spots are reported to develop complex, possibly vortex-like flows of energy and momentum as well as one of six polarisation skeletons. Dark spots like these could be powerful experimental tools for topological control, atom traps and sub-wavelength optical microscopy. In the final chapter we present a decomposed representation of light's spin angular momentum density akin to the spin-orbit decomposition of the Poynting vector, a sum of two terms, the canonical spin and Poynting spin, whose physical meanings we lay out. The two terms relate to the difference in canonical and spin momenta carried by left- and right-handed photons and we apply the decomposition to a range of electromagnetic fields including a linearly polarised vortex beam. Unifying this thesis we predict that at the centre of the vortex beam, in its dark spot, a longitudinal chiral pressure force exists and presents a way for the beam's orbital angular momentum to couple to matter in a chiral interaction.

Acknowledgements

I have had a fantastic supervisor, Paco, whose guidance and support have been very important to the successes that I have had during my PhD. It is no small thing that from the beginning, I have been able freely experiment, find, and excitedly work on what interests me, and that is because of Paco's philosophy and unrivalled enthusiasm for and generosity with new ideas. So for all of this I would like to say a special thank you to him. I've really enjoyed my time at King's and I would like to acknowledge everyone in the Photonics & Nanotechnology group, past and present and in the two offices, for making the experience as good as it has been. Members of our smaller group lead by Paco—Lei, Michela, Jack, Sinuhé and Sebastian—I have learned a lot from over the last three and a half years, both about physics and academia more generally. Thank you to my collaborators on each of my research projects, Mark, Andrew, Andrei, Sebastian, Claire, Eugene and Paco. I'm grateful to my friends from home, Jayssen, Ben, Yousuf, Farhan, Rajan, Ahmed and Younis, as also to my friends from the University of Birmingham, throughout my PhD and my Master's degree. Lastly, thank you to my parents and Biff the cat during my time away from London, and particularly in the last month of writing this thesis.

Contents

Chapter 1

Pockets of darkness in light

That was not only a juxtaposition. Light waves, by virtue of their being waves, can superpose to develop complex interference patterns that contain local maxima and minima, spots of bright and dim light, and should these waves be polarised in just the right way minima can darken completely into pockets of pitch black, surrounded by light elsewhere in space. These zero-brightness minima, which we would generally identify by light's electric field being zero ($\boldsymbol{\mathcal{E}}(\mathbf{r}, t) = \mathbf{0}$), are what in this thesis we call dark spots, our principle topic. This work ranges from a deep study of a dark spot's shape and characteristic impact on light, both in purely propagating light and in far-stranger near fields, to a simple proposed method to move dark spots through real and parameter spaces.

It was in the early 19$^{\text{th}}$ century that Thomas Young, splitting sunlight into two beams using a card, saw apparent dark spots*—regions of destructive interference—amid the resulting diffraction pattern that led to the conclusion that light behaves as a wave [1]. That Young's cornerstone experiment is so well-known does not, however,

*Sunlight is unpolarised and the interference minima in each frequency component would not be aligned, though overall minima and maxima would be visible.

mean that true dark spots are at all ordinary. For light is a vector wave and only if the light that passes through each of Young's slits is of one frequency and vertically polarised, parallel to the slits, could a zero-intensity interference minimum emerge in the electric field; the field vectors of the cylindrical waves emanating from the slits are this way able to engage with each other and interfere without longitudinal polarisation components, normal to the screen capturing the interference pattern[†], remaining in the minimum (this too is assuming that the interfering light is of one colour, and that the slits' waves' amplitudes are equal at the minimum's position!). Polarised otherwise, even though obvious dark fringes appear, the electric or magnetic field in any one minima could never truly be zero in all components. Suppose a more general scenario: N single-colour electromagnetic waves, say plane waves randomly polarised and each propagating in a random direction, superpose and set up the total electric field $\boldsymbol{\mathcal{E}}(\mathbf{r},t) = \sum_{i=1}^{N} \boldsymbol{\mathcal{E}}_i$. Trying then to identify a location $\mathbf{r}_\mathrm{z}$ where the combined electric field is exactly and constantly zero, that is $\boldsymbol{\mathcal{E}}(\mathbf{r}_\mathrm{z},t) = \mathbf{0}$, we would be unsuccessful. It cannot be guaranteed that within the span of three spatial dimensions the three components of $\boldsymbol{\mathcal{E}}$ are brought to zero simultaneously for all values of t, $\boldsymbol{\mathcal{E}} = \mathbf{0}$ simply needing too many mathematical conditions to be satisfied than can be provided by only three spatial degrees of freedom x, y, z[‡]. The only way to realise a true electric field dark spot is to control the superposing waves, perhaps by deliberately polarising them so that perfect destructive interference occurs at a chosen position $\mathbf{r}_\mathrm{z}$. A quarter of the original work of this thesis describes a method

[†]If the light is polarised orthogonal to the slits, then of the resulting cylindrical waves the electric field vector lies tangent to the wavefront curvature, and at the screen has a component pointing in the normal direction that relates to the line of sight to the slit. More detail is in chapter 4.

[‡]Even in far fields, where the electric field lies almost exactly tangent to spherical wavefronts ($\boldsymbol{\mathcal{E}} \approx \boldsymbol{\mathcal{E}}_\mathrm{t} = \mathcal{E}_\theta\hat{\boldsymbol{\theta}} + \mathcal{E}_\phi\hat{\boldsymbol{\phi}}$) and in these tangential components, $\boldsymbol{\mathcal{E}}_\mathrm{t} = \mathbf{0}$ is required in at least one location by the hairy ball theorem, the presence of small longitudinal field components (normal to wavefronts, parallel to propagation) means the full, three component vector $\boldsymbol{\mathcal{E}}$ is never zero exactly.

to create dark spots at any desired location in plane wave interference and in near fields.

For the very same reason that light's vector character makes it impossible for full suppression of the electric field to happen naturally in wave interference (meaning without outside control of interfering fields), an artificially synthesised dark spot can be deeply complicated in structure. The word 'structure' means more than simply the size and shape of the literal dark *spot* that contrasts with brighter space. Not only does single-frequency light have a certain polarisation determined by the orientation and oscillation of the vector $\boldsymbol{\mathcal{E}}$, a property that is undefined when $\boldsymbol{\mathcal{E}} = \mathbf{0}$ for all time, but it carries linear and possibly angular momentum, and transports energy in fluxes that are disrupted by the dark spot's presence. Subtleties in the way that polarisation and other physical quantities in light react to dark spots are a major point of study in this thesis, most notably in three-dimensional *non-paraxial* light because it is in this regime that the most striking features can be found. These features are especially surprising if, as is often the case, we are too accustomed to the (relatively speaking) less interesting physics of far field light, and certainly individual plane waves. For a plane wave is the simplest manifestation of propagating electric and magnetic fields, travelling in a single well-defined direction $\mathbf{k}$ (this being the wavevector), wavefronts perfectly planar, with the electric $\boldsymbol{\mathcal{E}}$ and magnetic $\boldsymbol{\mathcal{H}}$ vectors lying in-plane (that means $\boldsymbol{\mathcal{E}} \cdot \mathbf{k} = \boldsymbol{\mathcal{H}} \cdot \mathbf{k} = 0$). Although the polarisation of the wave (conventionally the 1D or 2D shape that the periodic $\boldsymbol{\mathcal{E}}$ vector traces in one oscillation) can vary, the $\boldsymbol{\mathcal{E}}$ and $\boldsymbol{\mathcal{H}}$ fields are tightly coupled (they are polarised identically up to a rotation about $\mathbf{k}$) and the plane wave's energy and momentum structure is ultimately very basic. Take linear polarisation, for instance: oscillating, the amplitude of the plane wave's electric and magnetic fields crosses zero periodically, such that separated by half a wavelength in the direction of $\mathbf{k}$ are entire planes of momentarily zero field,

dark phasefronts within the wave that propagate at the speed of light. But because the plane wave's $\boldsymbol{\mathcal{E}}$ and $\boldsymbol{\mathcal{H}}$ fields only equal zero at periodic *instants* in time, the time-averaged energy density of the wave and, therefore, the time-averaged number of photons per unit volume is uniformly non-zero across all of three-dimensional space (note that this means that plane waves carry infinite energy). As far as any matter that can interact with the light is concerned, instantaneous darkness is largely unimportant.

Single isolated plane waves cannot physically exist, their infinite size and delivery of energy being characteristics that can only be generated by a source infinite in more than one aspect. In truth sources of light are finite and given enough distance, wavefronts of radiation adopt a spherical curvature that lead to longitudinal field components, tiny but non-zero, via Gauss' law in free space $\nabla \cdot \boldsymbol{\mathcal{E}} = 0$ that means electric field lines must form closed loops. Towards another extreme, closer and closer to source (entering its near field within one wavelength λ distance), light behaves at its strangest: no longer is it so simple to define a direction of propagation, energy is often shared unequally between the electric and magnetic fields, and the $\boldsymbol{\mathcal{E}}$ and $\boldsymbol{\mathcal{H}}$ vectors can be oriented any way in three dimensions, free from confinement to a transverse plane and independently from each other insofar as Maxwell's equations allow. The ubiquity of longitudinal field components might seem disconnected from, even contradictory to the mental picture of light we might have developed when we first encountered Maxwell's equations. Yet, three-dimensional polarisation, energy and momentum inhomogeneity are utterly compliant with Maxwell's equations and, in reality, it is the perfect plane wave that is non-physical. Perhaps because any electromagnetic field can be expressed by an angular spectrum, an infinite sum of plane waves with different amplitudes and wavevectors, we might expect that light always holds on to its constituents' core properties. It is naive to assume, however, that

because plane waves are individually simple their vector sum must also be simple in terms of polarisation, energy and linear and angular momentum. This is far from the truth!

Only relatively recently had many subtle but striking phenomena emerging from the simple act of adding plane waves together begun to be discovered [2]; phenomena brought about by the way that vectors behave in wave interference and that although Maxwell's equations are themselves linear (meaning that the electric and magnetic fields resulting from many wave interference is the vector sum of each $\boldsymbol{\mathcal{E}}$ and each $\boldsymbol{\mathcal{H}}$ of the fields involved), other physical quantities in light are *not* linear with respect to $\boldsymbol{\mathcal{E}}$ and $\boldsymbol{\mathcal{H}}$. One such realisation (though older, relatively speaking) was that wave dislocations or 'scalar vortex lines' (scalar field interference minima) are a general feature of scalar wave interference [3]. Light's electric and magnetic fields are vector fields that, if comprised of one frequency and at their most complicated, have three components that are functions of space related by $\nabla \cdot \boldsymbol{\mathcal{E}} = 0$, i.e., $\boldsymbol{\mathcal{E}} = [\mathcal{E}_x(\mathbf{r}, t), \mathcal{E}_y(\mathbf{r}, t), \mathcal{E}_z(\mathbf{r}, t)]^T$, but which all oscillate sinusoidally with respect to time t. While it is unusual for all three components to equal zero for all time, each component is a scalar wave and, in say $\mathcal{E}_x$, there *generically* exist one-dimensional threads where that $\mathcal{E}_x$ component is permanently zero, independent of t—dark lines in individual field components [4–6]. To stress the word 'generically' in this context, we mean that no matter how structurally complicated an electromagnetic field, no matter how many other fields of the same frequency might interfere with it nor how those fields are individually polarised nor the direction in which they propagate, should we measure any one component of the resulting field, there are (outside of the simplest degenerate cases) *always* co-ordinates in space where there is *complete* destructive interference of that component (the reason for this we shall return to later). That electromagnetic waves interfere destructively is, by their definition as waves, far from

surprising; we said that interference minima in light have been observed for centuries since Young's double slit experiment. But there is something particularly special about scalar vortex lines, in the way that the surrounding light (where the scalar component is non-zero) has to smoothly adapt to the presence of a *one-dimensional* strand of darkness. Darkness is able to stir intrinsic orbital angular momentum into an electromagnetic field, hence the word 'vortex'.

Why dark spots?

The discovery that darkness in light causes orbital angular momentum to be carried by the surrounding, non-zero field [7] has led over the last thirty years to an explosion of interest in so-called vortex beams. Vortex beams, depending on the choice of basis, can be imagined to contain at their centre one or two superimposed scalar vortex lines that define a dark axis, enclosed by a bright, doughnut-shaped ring. Besides sending particles into orbit around the beam axis, the vortex beam's non-trivial spatial structure can store information [8, 9] and in its intimate relationship with polarisation, gives rise to many surprising phenomena [10]. But the physical richness and applicability of dark spots go far beyond the vortex beam, and in the next short sections we list some of the key motivations for a more general study of dark spots and highlight the direct relevance of the work which we present in this thesis.

Topological control

Depending on the spatial complexity of an electromagnetic field and the number of field components that are zero at the same time, zeros need not only take a one-dimensional form. It is, in fact, possible to non-stably produce planar or even

point-like, pin-prick pockets of darkness, the latter likely being a vector dark spot where more than one component is zero in the midst of an elliptically polarised field. Whatever its shape, be it a plane, a line or a point, a dark spot is inherently strange because as we mentioned, just as one of or both of the electric and magnetic fields vanish many of light's vector physical properties become singular automatically, resulting in non-trivial currents of energy, momentum and other quantities. Perhaps by synthesising dark spots or by specially organising other topological objects related to phase or polarisation, an electromagnetic field's topology can be deliberately manipulated, leading to richly complicated structures that sometimes are too exceptional to form naturally [11–15]. This way light can in some sense pose as a sandbox for exploring or inspiring the search for other topological phenomena that emerge elsewhere in physics, certainly in other wave theories such as those of gravity, acoustics and water waves [16–19]. That is why there is a strong theoretical interest in understanding the imprint(s) of dark spots in surrounding light fields, and to this end two chapters of this thesis (chapters 4 and 5) are dedicated to studying vector dark spots (when multiple components of a field are zero simultaneously) in two-dimensional (paraxial, far-field) and three-dimensional (non-paraxial, near-field) radiation, reporting novel findings based on two publications [20, 21]. Seeking in part to unify these two chapters under the umbrella of topological control, chapter 6 describes a simple approach to creating and controlling the position of dark spots by modulating the polarisation degrees of freedom of two plane waves. A detailed topological study of dark spots might at first seem arcane and impractical yet, particularly in light-matter interactions, dark spots can be remarkably effective experimental tools, most of all in the trapping and manipulation of atoms and in super-resolution microscopy.

Dark traps

Matter can be pushed by different aspects of an electromagnetic field, for instance by photon impacts, by the flow of active and reactive power, or by non-uniformity in energy density. The latter results in *gradient force* that normally pushes particles towards regions where light is brightest (for example the focus of a beam) and is the traditional mechanism driving optical trapping. But the sensitivity of a particle to this gradient force is frequency-dependent, and it turns out that in light sufficiently 'blue' with respect to a resonance of the particle, the gradient force reverses direction and pushes the particle into darkness. Then, a dark spot surrounded by blue-detuned, higher intensity can behave as a blue-detuned trap [22] with some advantages over conventional traps, namely that the lack of intensity increases the coherence time of captured atoms [23] and could reduce heating effects in trapped particles, and that a dark spot can be arbitrarily wide or narrow while the size of an intensity maximum is constrained by wavelength (meaning a dark spot can be more size-selective towards trapped particles). Blue-detuned traps can be realised in many different configurations [24–27] but with our proposal in chapter 6, three-dimensional blue-detuned traps in the form of point-like, non-paraxial dark spots (confined in all directions) could be synthesised in any desired location in a non-paraxial field, and moved, using far field illumination. We supplement this potential application of controllable point-like dark spots when in chapter 5 we characterise associated polarisation structures, flows of energy, and momentum streamlines that can couple to forces in the dark spot's immediate neighbourhood.

Super-resolution microscopy

Among the many techniques at the disposal of humans for seeing microscopic detail, optical microscopy techniques tend to be used in the study of tiny biological structures because of the transparency of cells in the visible spectrum [28]. Components of cells like proteins can be imaged via labelling with molecules that fluoresce when illuminated with optical-frequency light, but this sort of method is fundamentally limited in resolution by the fact that visible wavelengths measure a large fraction of a micron, too large for clear images of objects under a few hundred micrometres in size. Fluorescent molecules separated by less than half a wavelength cannot be distinguished—this is the diffraction limit, and while to resolve finer details one could in principle illuminate the target with shorter-wavelength light it is not always practical, especially when the target is biological. But cheating the diffraction limit *is* possible, it turns out, by relying on the theoretically unlimited sharpness of a dark spot; techniques that use dark spots such as stimulated-emission-depletion microscopy (STED) proposed in the 1990s have since been developed significantly and at the cutting edge allow nanometre-scale single-molecule imaging using visible light.

The principle basis for many of these techniques, including STED [29], is to selectively switch fluorophores (that are in too-close proximity to be individually resolved) between detectable 'on' and undetectable 'off' states. An initial excitation (e.g., a Gaussian spot of light, whose size is constrained by the diffraction limit) brings a collection of impinging fluorescent particles in to fluorescence (the 'on' state), that they may be observed from the far field but without being individually determined. Then a second, *doughnut*-shaped beam containing a central dark spot is shone on the target fluorophores. The frequency of this second beam is different to the first (red-

detuned) so as to drive all illuminated particles back down into the 'off' state—except, of course, for fluorophores lying in the beam's dark centre, which remain in the 'on' state and can still be detected. Since the central dark spot can be arbitrarily narrow it can isolate single molecules and so, using the two beams in sequence, fluorescent molecules can be excited one by one and upon knowing the molecules' locations a sub-diffraction-limit image may be reconstructed. Determining the location of a single molecule is not trivial and in any one approach requires that the dark-spot-containing beam is position-controlled. More powerful still is MINFLUX [30], which only implements a single beam with a dark spot (generically a doughnut) at an exciting frequency. Careful control of the doughnut beam's position while counting emitted photons (as fluorophores are excited by the bright ring but not by the dark centre), provides a markedly more efficient (in terms of emission) means of locating, tracking and imaging molecules with single-nanometre precision after post-processing.

Yet, the conventional doughnut beam's dark spot is axial, only confined in two dimensions, and therefore insufficient to resolve depth and construct three-dimensional images by selective excitation of fluorophores aligned parallel to the beam axis. One solution could be to use a point-like dark spot with full, three-dimensional confinement. If the position of the dark spot can be controlled then it could be possible, using a similar methodology to MINFLUX, to locate and track fluorescent particles in three dimensions. Once more chapter 6's proposed technique for point-like dark spot position control is strongly relevant.

Thesis outline

The thesis is divided into six further chapters, numbered 2-7. Dark spots in light can be difficult to fully appreciate if one is not comfortable with the more extraordinary physics of (non-paraxial) three-dimensional fields. They are, moreover, vector singularities of polarisation, linear momentum, and active and reactive power flow, all of which (and other quantities) must be defined before our findings are given. Thus the purpose of the next two chapters of this thesis. Chapter 2's primary objective is to define fundamental quantities, quadratic with respect to $\boldsymbol{\mathcal{E}}$ and $\boldsymbol{\mathcal{H}}$, that describe the field's flux of energy density, its linear momentum and spin angular momentum, to name a few. Meanwhile the second chapter outlines mainly the polarisation properties of monochromatic light, beginning with the polarisation ellipse that is met with discussion of polarisation singularities, then detailing the structural distinctions between paraxial and non-paraxial light (chapter 3 provides a more thesis-specific background compared to chapter 2). We begin presenting our original findings [21] in chapter 4, a treatment of paraxial, transverse field dark spots that give rise to non-diffracting polarisation structures that persist infinitely into the far field. Next in chapter 5 we transition to the non-paraxial regime which can support point-like dark spots and some of the most remarkable coupled topological structures [20]. In both chapters 4 and 5 we probe in analytical simulations dark spots that have been synthesised using a simple polarisation-modulation technique, with which dark spots can be created and fully position-controlled, that we explain in chapter 6. Finally chapter 7 of the thesis reports the results of [31] and is somewhat of an outlier, for it attempts to clarify the physical significance and possible geometric properties of an alternative expression of light's spin angular momentum density. Though it is not primarily concerned with dark spots we predict, after establishing the links be-

tween this expression of spin density and chiral optical forces on dipolar particles, a surprising longitudinal chiral force present at the centre of an optical vortex, a quite appropriate last example of the sort of exceptional consequences of dark spots' singular nature that continue to be discovered today.

Chapter 2

Fundamentals

There are four equations,

$$\begin{aligned} \nabla \cdot \boldsymbol{\mathcal{E}} &= \frac{\rho}{\epsilon_0}, \\ \nabla \cdot \boldsymbol{\mathcal{H}} &= 0, \\ \nabla \times \boldsymbol{\mathcal{E}} &= -\mu_0 \frac{\partial \boldsymbol{\mathcal{H}}}{\partial t}, \\ \nabla \times \boldsymbol{\mathcal{H}} &= \boldsymbol{\mathcal{J}} + \epsilon_0 \frac{\partial \boldsymbol{\mathcal{E}}}{\partial t}. \end{aligned} \tag{2.1}$$

that have since their introduction in the 19^{th} century provided a unified understanding of electricity and magnetism. The Maxwell equations, that above are given in their microscopic form and which combine Gauss' laws, Faraday's law and the Maxwell-Ampere law, are a set of spatial and temporal rules that lock together the electric $\boldsymbol{\mathcal{E}}(\mathbf{r}, t)$ and magnetic $\boldsymbol{\mathcal{H}}(\mathbf{r}, t)$ fields, emerging initially from static charge density $\rho(\mathbf{r}, t)$ and moving charge (current) density $\boldsymbol{\mathcal{J}}(\mathbf{r}, t)$, and constrain their degrees of freedom. Should these vector fields conform to all four of Maxwell's equations at the same time they are physically realisable, be they static (meaning $\partial/\partial t \to 0$, for example an electric field in a fully charged capacitor; $\rho \neq 0$, or the magnetic field set

up around a wire carrying DC current; $\boldsymbol{\mathcal{J}} \neq \mathbf{0}$) or oscillating, wherein time derivatives are non-zero and it is possible for non-zero electric and magnetic fields to exist beyond the bounds of charge or current density. For if the electric and magnetic fields $\boldsymbol{\mathcal{E}}$ and $\boldsymbol{\mathcal{H}}$ both obey the wave equation and, as vectors, are oriented in the correct way then energy can travel in completely free space, absent of charges, by mutual propagation of the electric and magnetic fields at the speed of light. According to Maxwell's equations one field cannot propagate through space without the other—oscillation of, say, the electric field (change over time, $\partial\boldsymbol{\mathcal{E}}/\partial t \neq \mathbf{0}$) must be accompanied by spatial variation in the magnetic field ($\nabla \times \boldsymbol{\mathcal{H}} \neq \mathbf{0}$) and vice versa—and geometric requirements of the $\boldsymbol{\mathcal{E}}$ and $\boldsymbol{\mathcal{H}}$ vectors, imposed by curls $\nabla\times$, mean that (purely propagating) electromagnetic waves are transverse waves and carry two polarisation degrees of freedom. When $\boldsymbol{\mathcal{J}} = \mathbf{0}$ and $\rho = 0$ Maxwell's equations simplify and mathematically treat the $\boldsymbol{\mathcal{E}}$ and $\boldsymbol{\mathcal{H}}$ fields equally, in a dual-symmetric regime through which we arrive at virtually all of the findings of this thesis (on the occasion that matter does come into play we will not generally be interested in internal fields, only the influence and interference of scattered fields in surrounding vaccuum outside of current and charge densities).

Although Maxwell's equations detail the non-negotiable relationship between the electric and magnetic fields many other quantities, some observables, are not directly specified by the four expressions Eq. (2.1). For instance the direction of an electromagnetic wave's flow of energy, and its linear and angular momenta are not explicit, which is not to say that this physical information is not implicit in Maxwell's equations, rather that to obtain expressions in free space we need to take extra steps combining the $\boldsymbol{\mathcal{E}}$ and $\boldsymbol{\mathcal{H}}$ fields via some vector operation. Proper definitions of light's momenta and energy fluxes are important not only for understanding how light can interact with matter, but for our own comprehension of the topology of

an electromagnetic field, however spatially complicated, and the singular nature of any dark spots it may contain. Like the electric and magnetic fields these quantities oscillate over time yet, given how quickly light in the visible regime oscillates, any interacting matter is largely concerned with time-averaged quantities. When only one frequency component is present in light, its time dependence is trivial and time-averaged quantities are straightforward to define using *phasors*, representations of the electric and magnetic field's spatial and polarisation structure using complex vectors $\mathbf{E}(\mathbf{r})$ and $\mathbf{H}(\mathbf{r})$ that are not time-dependent. We only consider monochromatic light in this thesis and phasors are used throughout and though they are quite simple to follow, to prevent confusion we shall explain exactly what they mean next.

2.1 Phasors (and notation)

That Maxwell's equations are linear with respect to $\boldsymbol{\mathcal{E}}$ and $\boldsymbol{\mathcal{H}}$ means that no matter how many superposing fields of the same colour, however polarised and propagating in whichever direction, the oscillations in time of the entire superposition's total electric field $\boldsymbol{\mathcal{E}}(\mathbf{r}, t)$ are predictably sinusoidal, that is $\boldsymbol{\mathcal{E}}(\mathbf{r}, t) = \mathbf{p}(\mathbf{r}) \sin \omega t + \mathbf{q}(\mathbf{r}) \cos \omega t$ (and likewise for the magnetic field). Note that the two real vectors $\mathbf{p}(\mathbf{r})$ and $\mathbf{q}(\mathbf{r})$ that are solely functions of $\mathbf{r} = x\hat{\mathbf{x}} + y\hat{\mathbf{y}} + z\hat{\mathbf{z}}$ completely describe the spatial structure of the monochromatic superposition. Practically all of the interesting characteristics that monochromatic light can possibly acquire come from the $\mathbf{r}$-variation of $\mathbf{p}(\mathbf{r})$ and $\mathbf{q}(\mathbf{r})$ and for this reason, single-frequency light's predictable time-dependence is often omitted, favouring time-independent but complex electric and magnetic field phasors $\mathbf{E}$ and $\mathbf{H}$. These relate to the instantaneous fields $\boldsymbol{\mathcal{E}}$ and $\boldsymbol{\mathcal{H}}$ through Euler's

identity, for instance,

$$\boldsymbol{\mathcal{E}}(\mathbf{r},t) = \mathbf{p}(\mathbf{r})\sin\omega t + \mathbf{q}(\mathbf{r})\cos\omega t = \Re\{\mathbf{E}(\mathbf{r})\exp(-i\omega t)\}, \tag{2.2}$$

where $\mathbf{E}(\mathbf{r}) = \mathbf{p}(\mathbf{r}) + i\mathbf{q}(\mathbf{r})$ (we may represent the instantaneous magnetic field $\boldsymbol{\mathcal{H}}$ similarly using $\mathbf{H} = \mathbf{a}(\mathbf{r}) + i\mathbf{b}(\mathbf{r})$ where $\mathbf{a}$ and $\mathbf{b}$ are different to $\mathbf{p}$ and $\mathbf{q}$). The imaginary part $\Im\{\mathbf{E}(\mathbf{r})\exp(-i\omega t)\}$ is merely an artefact of Euler's identity and is discarded; it has no real significance beyond being an image of what $\boldsymbol{\mathcal{E}}(\mathbf{r},t)$ looks like a quarter period later in time.

It is critical to now highlight the deliberate distinction in notation between $\boldsymbol{\mathcal{E}}$ and $\mathbf{E}$. The scripted character $\boldsymbol{\mathcal{E}}(\mathbf{r},t)$ is a real vector, oscillating over time, corresponding exactly to the electric field that would be measured at any instant t by a probe placed at a position $\mathbf{r}$ (assuming the response of the probe was arbitrarily fast). The non-scripted character $\mathbf{E}(\mathbf{r}) = \mathbf{p}(\mathbf{r}) + i\mathbf{q}(\mathbf{r})$ is a *phasor*, a complex vector that is a function of space only and whose real and imaginary parts $\mathbf{p}(\mathbf{r})$ and $\mathbf{q}(\mathbf{r})$ contain all polarisation and spatial information of a monochromatic field—again, all the information of real interest. A phasor like $\mathbf{E}$ is a mathematical convenience but not a physical vector that can be measured directly (i.e., without measuring $\boldsymbol{\mathcal{E}}$ and inferring $\mathbf{E}$ from the measurement), convenient because one can construct a phasor version of Eq. (2.1) wherein time-derivatives are simplified by $\partial/\partial t \to -i\omega$ so that the electric and magnetic phasors are proportional to each other's curls. In free space

(no charges or currents) these equations are:

$$\begin{aligned} \nabla \cdot \mathbf{E} &= 0, \\ \nabla \cdot \mathbf{H} &= 0, \\ \nabla \times \mathbf{E} &= i\omega\mu_0 \mathbf{H}, \\ \nabla \times \mathbf{H} &= -i\omega\epsilon_0 \mathbf{E}. \end{aligned} \tag{2.3}$$

The full instantaneous representation for monochromatic light can be recovered by multiplying each expression in Eq. (2.3) by $\exp(-i\omega t)$ and taking their real parts $\Re\{*\}$. We adopt this convention of scripted letters denoting functions of space and time and non-scripted letters for functions of space only (being either phasors or time-averaged quantities) throughout this thesis.

2.2 Time-averaged quantities

For light, many quantities like the flow of electromagnetic energy are expressed by (in broad terms) squaring the components of the time-varying electric $\boldsymbol{\mathcal{E}}(\mathbf{r}, t)$ and magnetic fields $\boldsymbol{\mathcal{H}}(\mathbf{r}, t)$, or by inter-field multiplication. Then, the kind of quantity that results is a function of time. For example, consider the expression

$$\boldsymbol{\mathcal{X}}(\mathbf{r}, t) \diamond \boldsymbol{\mathcal{Y}}(\mathbf{r}, t), \tag{2.4}$$

where the $\diamond$ represents any vector product preserving linear addition such as '$\cdot$' or '$\times$' (so Eq. (2.4) could evaluate to a scalar or a vector). We could conceivably replace $\boldsymbol{\mathcal{X}}$ and $\boldsymbol{\mathcal{Y}}$ by either $\boldsymbol{\mathcal{E}}$ and $\boldsymbol{\mathcal{H}}$ in any combination. Whatever the product, $\boldsymbol{\mathcal{X}} \diamond \boldsymbol{\mathcal{Y}}$ inherits some aspects of the behaviour in time of $\boldsymbol{\mathcal{X}}$ and $\boldsymbol{\mathcal{Y}}$: if $\boldsymbol{\mathcal{X}}$ and $\boldsymbol{\mathcal{Y}}$ are composed of

many frequencies then at a given point in space, $\boldsymbol{\mathcal{X}} \diamond \boldsymbol{\mathcal{Y}}$ probably oscillates erratically. However for monochromatic vectors, $\boldsymbol{\mathcal{X}} \diamond \boldsymbol{\mathcal{Y}}$ too oscillates predictably with, due to the fact that it squares the time-dependence of $\boldsymbol{\mathcal{X}}$ and $\boldsymbol{\mathcal{Y}}$, an easily defined 'DC' component representing the product's time-averaged magnitude (and orientation if it has one), and a purely oscillating component with zero mean. Explicitly, if $\boldsymbol{\mathcal{X}}$ and $\boldsymbol{\mathcal{Y}}$ relate to complex phasors via

$$\begin{aligned} \boldsymbol{\mathcal{X}}(\mathbf{r}, t) &= \Re\{\mathbf{X}(\mathbf{r})\mathrm{e}^{-i\omega t}\} \\ \boldsymbol{\mathcal{Y}}(\mathbf{r}, t) &= \Re\{\mathbf{Y}(\mathbf{r})\mathrm{e}^{-i\omega t}\}, \end{aligned} \tag{2.5}$$

we can expand with trigonometry Eq. (2.4) using the real and imaginary parts of $\mathbf{X}$ and $\mathbf{Y}$, obtaining

$$[\boldsymbol{\mathcal{X}} \diamond \boldsymbol{\mathcal{Y}}](\mathbf{r}, t) = \frac{1}{2}\Re\{\mathbf{X}^* \diamond \mathbf{Y}\} + \frac{1}{2}\Re\{\mathbf{X} \diamond \mathbf{Y}\}\cos 2\omega t + \frac{1}{2}\Im\{\mathbf{X} \diamond \mathbf{Y}\}\sin 2\omega t. \tag{2.6}$$

Out of this expansion comes a non-time-varying, DC term $(1/2)\Re\{\mathbf{X}^* \diamond \mathbf{Y}\}$ that includes the complex conjugate $\mathbf{X}^*$ (recall that $\mathbf{X}$ and $\mathbf{Y}$ are only functions of $\mathbf{r}$). Since the oscillating terms average to zero over time it is only this DC component, the time-average of $\boldsymbol{\mathcal{X}} \diamond \boldsymbol{\mathcal{Y}}$, that could have any measurable effect. It is highly convenient to work with time-averaged quantities defined using phasors and denoted by non-scripted letters that quantify the net effect of light's dynamic behaviour.

2.2.1 Electromagnetic energy

We have not arbitrarily invoked a quadratic quantity $\boldsymbol{\mathcal{X}} \diamond \boldsymbol{\mathcal{Y}}$ here for the purpose of explanation. It turns out according to Poynting's theorem that a vector $\boldsymbol{\mathcal{P}} = \boldsymbol{\mathcal{E}} \times \boldsymbol{\mathcal{H}}$ fits all the criteria of the flow of energy in light according to the continuity equation

[32]

$$\nabla \cdot \boldsymbol{\mathcal{P}} = \nabla \cdot (\boldsymbol{\mathcal{E}} \times \boldsymbol{\mathcal{H}}) = -\frac{\partial \mathcal{W}}{\partial t}, \tag{2.7}$$

where $\mathcal{W}$ represents time-varying energy density and $\boldsymbol{\mathcal{P}}$ is called the Poynting vector. The supreme significance of time-averaged quantities in monochromatic light is such that the DC component $\mathbf{P}$ of $\boldsymbol{\mathcal{P}}$,

$$\mathbf{P} = \frac{1}{2}\Re\{\mathbf{E}^* \times \mathbf{H}\}, \tag{2.8}$$

is mainly called the Poynting vector too. We adopt this nomenclature in this thesis; rarely shall we encounter the complete time-dependent vector $\boldsymbol{\mathcal{P}}$ and, from now on, any time we mention 'the Poynting vector' we refer to the time-averaged vector $\mathbf{P}$ Eq. (2.8). Instantaneous energy density in free space $\mathcal{W}$ takes the form [32]

$$\mathcal{W} = \frac{1}{2}\left(\epsilon_0 \boldsymbol{\mathcal{E}} \cdot \boldsymbol{\mathcal{E}} + \mu_0 \boldsymbol{\mathcal{H}} \cdot \boldsymbol{\mathcal{H}}\right), \tag{2.9}$$

which according to Eq. (2.6) has a time-averaged component given by

$$W = \frac{1}{4}\left(\epsilon_0 \mathbf{E}^* \cdot \mathbf{E} + \mu_0 \mathbf{H}^* \cdot \mathbf{H}\right), \tag{2.10}$$

and the oscillating terms

$$\frac{1}{4}\Re\{\epsilon_0 \mathbf{E} \cdot \mathbf{E} + \mu_0 \mathbf{H} \cdot \mathbf{H}\} \cos 2\omega t + \frac{1}{4}\Im\{\epsilon_0 \mathbf{E} \cdot \mathbf{E} + \mu_0 \mathbf{H} \cdot \mathbf{H}\} \sin 2\omega t. \tag{2.11}$$

These expressions incorporate contributions from both the electric and magnetic phasors (the leading 1/4 factor comes partly from time averaging and partly from averaging electric and magnetic energy densities). It is worth keeping in mind that if,

say, $\mathbf{E} \cdot \mathbf{E} = 0$ then the electric energy density does not oscillate—the square length of the instantaneous electric field vector does not change over one period—which we shall see is characterstic of circular polarisation. Except when energy is lost due to absorption, the time derivative of W is zero meaning $\nabla \cdot \mathbf{P} = 0$.

The importance of placing $\mathbf{E}$ and $\mathbf{H}$ on an equal footing in the definition of W Eq. (2.10) is most apparent in non-paraxial light. Though an in-depth description of the difference between paraxial and non-paraxial light is not provided until the next chapter, suffice to say that only *paraxial* light (including plane waves and far fields) is dual-symmetric and has its energy density divided equally between the electric and magnetic fields such that $W = (1/2)\epsilon_0 \mathbf{E}^* \cdot \mathbf{E} = (1/2)\mu_0 \mathbf{H}^* \cdot \mathbf{H}$. Non-paraxial light (including near fields) commonly has its energy density split unevenly between $\mathbf{E}$ and $\mathbf{H}$ in a breaking of duality symmetry with respect to the fields* [33–36]. Defined by a vector cross product between $\mathbf{E}^*$ and $\mathbf{H}$ the Poynting vector Eq. (2.8) cannot access all of the energy density present in an electromagnetic field if there is an asymmetric energy share between $\mathbf{E}$ and $\mathbf{H}$, or equally, if the instantaneous $\boldsymbol{\mathcal{E}}$ and $\boldsymbol{\mathcal{H}}$ vectors are not always perpendicular during oscillation. Thus when electric-magnetic asymmetry is present in non-paraxial light a portion of energy density is stored, unavailable to be transferred by $\mathbf{P}$.

One measure of asymmetry between $\mathbf{E}$ and $\mathbf{H}$ is the reactive energy density W_{Re}, the difference between electric and magnetic energy densities:

$$W_{\mathrm{Re}} = \frac{1}{4}\left(\epsilon_0 \mathbf{E}^* \cdot \mathbf{E} - \mu_0 \mathbf{H}^* \cdot \mathbf{H}\right). \tag{2.12}$$

*Although Maxwell's equations are known in free space to remain unchanged after a continuous duality transform, it is not necessarily true that the electric and magnetic fields themselves keep the same relative amplitude or polarisation throughout the transformation.

Its flux [37] is known as the imaginary Poynting vector (IPV) [38–41],

$$\mathbf{P}_{\mathrm{i}} = \frac{1}{2}\Im\{\mathbf{E}^* \times \mathbf{H}\}, \tag{2.13}$$

a frequently ignored quantity because it is zero in far fields—but in the non-paraxial regime the IPV can be responsible for a variety of rich interactions. For the IPV couples to a term in the total optical force exerted on Rayleigh particles [42, 43], only recently observed [41], and whose dual-asymmetric quality (the fact that swapping $\mathbf{E} \to \mathbf{H}$ and $\mathbf{H} \to -\mathbf{E}$ changes the sign of the IPV) has interesting consequences for asymmetric particles [38, 39].

2.2.2 Linear momentum and wavevectors

A photon has a free-space momentum vector equal simply to $\hbar\mathbf{k}$, where $\mathbf{k}$ is the wavevector and $\sqrt{\mathbf{k}\cdot\mathbf{k}} = k = 2\pi/\lambda$ is the free-space wavenumber. Yet producing a consistent definition of the linear momentum carried by light has historically been a complicated task, there being the question of whether upon entering a macroscopic medium a photon's free-space momentum increases or decreases by a factor of n, the medium's refractive index [44]. There are two quantities in conflict: the Abraham momentum and the Minkowski momentum, which Barnett equated with kinetic and canonical momenta respectively [44, 45], both equally meaningful. It has been suggested that as the photon propagates through the medium, it displaces and locally alters the density of atoms to create a 'mass-density wave' that moves in tandem with the photon [46, 47]. Consideration of the photon's movement alone results in the Abraham kinetic momentum, while the coupled movement of the photon and medium atoms recovers the Minkowski canonical momentum. Even with this and other convincing interpretations [48, 49], not all debate of the dilemma is completely

resolved [50, 51].

Much of the dilemma's original debate and the many efforts to find a resolution experimentally (with no unanimous conclusions) came before researchers began to take strong interest in non-paraxial light where, even in free space, it is not so straightforward to define a photon's wavevector $\mathbf{k}$. Non-paraxial light's mechanical properties vary significantly even over sub-wavelength scales so it is useful in this regime to deal with locally defined kinetic $\mathbf{\Pi}$ and canonical $\mathbf{p}$ momentum densities [51], both of which relate in some way to the Poynting vector $\mathbf{P}$. The kinetic momentum density is obtained by dividing the Poynting vector by c^2,

$$\mathbf{\Pi} = \frac{1}{2c^2}\Re\{\mathbf{E}^* \times \mathbf{H}\}, \tag{2.14}$$

while canonical momentum density has the form [51–54],

$$\mathbf{p} = \frac{1}{4\omega}\Im\{\epsilon_0\mathbf{E}^* \cdot (\nabla)\mathbf{E} + \mu_0\mathbf{H}^* \cdot (\nabla)\mathbf{H}\}. \tag{2.15}$$

where $\mathbf{A}\cdot(\nabla)\mathbf{B} = A_x\nabla B_x + A_y\nabla B_y + A_z\nabla B_z$ and, like the energy density Eq. (2.10), $\mathbf{p}$ combines separate electric and magnetic momentum contributions. The two densities Eq. (2.14) and Eq. (2.15) coincide for a plane wave, $\mathbf{\Pi} = \mathbf{p} = (W/\omega)\mathbf{k}$ where W is time-averaged energy density Eq. (2.10), whose wavevector $\mathbf{k}$ is easily identified, and is constant throughout space. But when in the non-paraxial regime (including surprisingly simple plane wave interference [2]) light's structure grows more complex, it is not always obvious to say in which direction the field propagates, tending to vary

from place to place[†]. The kinetic momentum density $\mathbf{\Pi}$, it turns out, cannot reconcile some of the strangest non-paraxial phenomena such as the transfer of momentum greater in magnitude than $\hbar k$ [55], which can occur in evanescent waves [52]. For this reason, and because it couples to the readily measurable radiation pressure force [42, 53], canonical momentum density is often argued to be the more meaningful quantity in non-paraxial fields.

When normalised, canonical momentum density also serves as a 'local' wavevector $\mathbf{k}_{\text{loc}}$, quantifying the average phase gradient of what in the non-paraxial regime are three-dimensional and less-restricted, complex electric and magnetic phasors. An appropriate local phase gradient defined for these phasors is not immediately clear—each component of a phasor is a complex scalar field with its own unique phase angle and phase gradient—but one can calculate the weighted average of the gradient of each component. Take, for instance, the $\hat{\mathbf{x}}$ component of the electric field phasor, a complex scalar field,

$$E_x(\mathbf{r}) = A(\mathbf{r})\mathrm{e}^{i\phi_x(\mathbf{r})}, \tag{2.16}$$

$A = |E_x|$ being a real scalar and ϕ_x the phase angle, both of which are position-dependent. Its gradient multiplied by E_x^* gives the expression,

$$\begin{aligned} E_x^*\nabla E_x &= A\mathrm{e}^{-i\phi_x}[(\nabla A)\mathrm{e}^{i\phi_x} + i(\nabla\phi_x)A\mathrm{e}^{i\phi_x}] \\ &= A\nabla A + iA^2\nabla\phi_x, \end{aligned} \tag{2.17}$$

whose second equality's real part is half the gradient of the $\hat{\mathbf{x}}$ component intensity, and whose imaginary part $A^2\nabla\phi_x$ carries the phase gradient of E_x. Then, by calcu-

[†]in fact this is also true in a macroscopic view of far fields: a spherical wave, for instance, propagates radially in 3D according to the phase factor $\exp(ikr)$. While, zooming in on a far-field wavefront, the wave's spherical curvature appears to flatten relative to wavelength distances and propagate along a single well-defined radial wavevector, this apparent wavevector does point in the same direction globally across the entire spherical wavefront.

lating $\Im\{E_x^*\nabla E_x + E_y^*\nabla E_y + E_z^*\nabla E_z\} = \Im\{\mathbf{E}^* \cdot (\nabla)\mathbf{E}\}$ we have a sum of the phase gradients from all three field components, weighted by their respective intensities, and by dividing by the total electric intensity $\mathbf{E}^* \cdot \mathbf{E} = |\mathbf{E}|^2$ we recover the phase gradient's radians-per-metre units and thus a definition of a local electric wavevector [33, 56, 57]. In complex form, and after multiplication by $-i$, its real part is related to the electric contribution to the canonical momentum,

$$\mathbf{k}_{\mathrm{loc}}^{\mathrm{e}} = -i\frac{1}{|\mathbf{E}|^2}\mathbf{E}^* \cdot (\nabla)\mathbf{E}. \tag{2.18}$$

This local wavevector is an important concept for understanding how, due to $\nabla\phi_{x,y,z}$ diverging, per-photon momentum can be amplified and integral curves contorted by dark spots, particularly relevant in chapter 5 of this thesis. Often because of the asymmetric response of matter to electric and magnetic fields, it is reasonable to consider only electric quantities like Eq. (2.18) though, like the canonical momentum density, only the full definition is dual-symmetric and fundamental [57],

$$\mathbf{k}_{\mathrm{loc}} = \frac{1}{\epsilon_0|\mathbf{E}|^2 + \mu_0|\mathbf{H}|^2}\left(\epsilon_0|\mathbf{E}|^2\mathbf{k}_{\mathrm{loc}}^{\mathrm{e}} + \mu_0|\mathbf{H}|^2\mathbf{k}_{\mathrm{loc}}^{\mathrm{m}}\right), \tag{2.19}$$

wherein $\mathbf{k}_{\mathrm{loc}}^{\mathrm{m}}$ assumes an identical form to Eq. (2.18) with $\mathbf{E} \to \mathbf{H}$.

We have not yet mentioned that kinetic and canonical momentum densities are connected by a third momentum density, the spin momentum $\mathbf{p}^{\mathrm{s}}$, in that

$$\mathbf{\Pi} = \mathbf{p} + \mathbf{p}^{\mathrm{s}}, \tag{2.20}$$

$\mathbf{p}^{\mathrm{s}}$ defined according to [33, 52],

$$\mathbf{p}^{\mathrm{s}} = \frac{1}{2}\nabla \times \frac{1}{4\omega}\Im\{\epsilon_0\mathbf{E}^* \times \mathbf{E} + \mu_0\mathbf{H}^* \times \mathbf{H}\}. \tag{2.21}$$

Spin momentum is generated by an inhomogeneity in polarisation and on the occasions that it is isolated from canonical momentum, is responsible for surprising optical recoil forces such as in evanescent waves [58].

2.2.3 Angular momentum

Naturally, from the expressions of linear momentum densities in light it is also possible to define angular momentum densities with respect to a chosen origin [59, 60]. Light, having a vector structure, has two angular momentum degrees of freedom, one that originates from its spatial structure (*orbital*, from propagation) and a second from local rotation of the electric and magnetic field vectors over time [61] (*spin*, from polarisation). Rather than a single angular momentum density related to the Poynting vector [62], these degrees of freedom can be described by separate angular momentum densities: $\mathbf{L}$, the orbital angular momentum (OAM) density, and $\mathbf{S}$, the spin angular momentum (SAM) density, both of which ordinarily point in the longitudinal direction of a beam and sum to give the total angular momentum density of a light field $\mathbf{J}$ [51, 54],

$$\mathbf{J} = \mathbf{L} + \mathbf{S}. \tag{2.22}$$

First of the two terms, the OAM density $\mathbf{L}$ is given by [63, 64]

$$\mathbf{L} = \mathbf{r} \times \mathbf{p}, \tag{2.23}$$

where the position vector $\mathbf{r}$ is measured from a chosen co-ordinate origin and $\mathbf{p}$ is the canonical momentum Eq. (2.15). We said that $\mathbf{p}$ is proportional to an inhomogeneous field's local wavevector, the local direction that photons are travelling—so Eq. (2.23) can be interpreted as the moment of light's primary pushing force with respect to

some origin from which $\mathbf{r}$ is measured. That by choosing different locations of the co-ordinate origin the length of $\mathbf{r} \to \mathbf{r} + \mathbf{r}_0$, and apparently the value of $\mathbf{L} = (\mathbf{r} + \mathbf{r}_0) \times \mathbf{p}$ and its volume integral, change, is why light's OAM is normally called extrinsic. One can usually choose a certain co-ordinate origin so that when $\mathbf{L}$ is integrated over a volume containing an electromagnetic field (such as a Gaussian beam), the total OAM is zero—except when the field is specially structured (for instance by an optical vortex) in such a way as to leave a residual angular momentum that cannot be eliminated by moving the origin [62, 65] (we will attend to optical vortices in the next chapter). This sort of seemingly origin-independent OAM appearing in vortex beams is very often called *intrinsic* though it is important to note that (unlike the truly intrinsic spin angular momentum discussed next) the density itself Eq. (2.23) is still dependent on the choice of origin, and that in a quantum formalism it is only the *average* longitudinal OAM introduced by the azimuthal linear momentum density that is actually independent of $\mathbf{r}_0$ (whereas variance is not intrinsic). For these reasons, longitudinal OAM that arises from helical wavefronts could justifiably be called *quasi-intrinsic* [66].

Second, the time-averaged spin angular momentum (SAM) density vector is [33, 36]

$$\mathbf{S} = \frac{1}{4\omega} \Im\{\epsilon_0 \mathbf{E}^* \times \mathbf{E} + \mu_0 \mathbf{H}^* \times \mathbf{H}\}, \tag{2.24}$$

another quantity including separate contributions from the electric and magnetic fields which, as we will learn in the next chapter, are proportional to the normal vectors of the electric and magnetic polarisation ellipses. The traditional intuition that light's plane of polarisation should be transverse to the wavevector might suggest that $\mathbf{S}$ always points parallel to light's direction of propagation. But it is now very well-known that in evanescent waves [52] and non-paraxial light in general [2, 67–70]

the **E** and **H** fields can gain significant longitudinal polarisation components and thus spin in the transverse direction. There is no position vector **r** in Eq. (2.24) and as such SAM density does not change by choice of origin. For this reason SAM is intrinsic: provided a field is not linearly polarised (and electric and magnetic contributions do not cancel out [71]) then **S** is non-zero and the field carries non-zero spin angular momentum density[‡].

As long as dual-symmetry is preserved (Maxwell's equations Eq. (2.3) treat **E** and **H** equally as in free space) then, in addition to energy density, there is another conserved electromagnetic quantity for which **S** is the flux (in fact, there are infinitely many conserved quantities associated with symmetry between derivative fields of **E** and **H**, but they coincide up to a constant in monochromatic light [35, 72, 73]). This quantity is the helicity density h [36, 74–76][§],

$$h = -\frac{1}{2\omega c}\Im\{\mathbf{E}^* \cdot \mathbf{H}\}, \tag{2.25}$$

which has been identified as proportional to the difference in energy density carried by left and right handed photons in general [37, 43, 57, 79, 80] and so is one measure of how chiral the electric and magnetic fields are. In a plane wave and when normalised (in appropriate units) by energy density Eq. (2.10), h is maximal for circular polarisation, positive or negative depending on handedness, and zero for linear polarisation.

[‡]This is not necessarily true for the integrated spin angular momentum of a field, which may be zero overall despite having non-zero density.

[§]Although it is of the form of a time-averaged quantity the helicity density h in monochromatic light is not time-dependent. Other representations of helicity density with instantaneous vectors, e.g., $h = (\boldsymbol{\mathcal{A}} \cdot \boldsymbol{\mathcal{H}} - \boldsymbol{\mathcal{C}} \cdot \boldsymbol{\mathcal{E}})/(2c)$ where $\boldsymbol{\mathcal{A}}$ and $\boldsymbol{\mathcal{C}}$ are magnetic and electric vector potentials ($\nabla \times \boldsymbol{\mathcal{A}} = \mu_0 \boldsymbol{\mathcal{H}}$, $\nabla \times \boldsymbol{\mathcal{C}} = -\epsilon_0 \boldsymbol{\mathcal{E}}$) [35, 77], and of chirality density [73, 78], to which h is proportional in monochromatic fields, simplify by substitution of phasors to being proportional to $\Im\{\mathbf{E}^* \cdot \mathbf{H}\}$.

2.3 Chapter summary

We have provided time-averaged expressions for energy, linear and angular momentum in electromagnetic fields which will serve the original findings of chapters 4 to 7. In the following, second background chapter we are concerned more specifically with the spatial and polarisation structure of light between paraxial and non-paraxial regimes, drawing upon some of the quantities given here.

Chapter 3

The phase and polarisation structure of monochromatic light

The instantaneous electric $\boldsymbol{\mathcal{E}}(\mathbf{r}, t)$ and magnetic $\boldsymbol{\mathcal{H}}(\mathbf{r}, t)$ fields are vector functions of three-dimensional space, and time. As with any vector field, each of $\boldsymbol{\mathcal{E}}$ and $\boldsymbol{\mathcal{H}}$ can be visualised by imagining, at every real-space co-ordinate, abstract arrows which in the most generic case have three components and oscillate along arbitrary paths as time evolves. It is the trajectory that the $\boldsymbol{\mathcal{E}}$ ($\boldsymbol{\mathcal{H}}$) field arrow follows over time which we call the electric (magnetic) polarisation. While in general the electric and magnetic fields are polarised differently, an electromagnetic wave (or a superposition of electromagnetic waves, however complicated) must uphold a degree of symmetry between electric and magnetic polarisation because the $\boldsymbol{\mathcal{E}}$ and $\boldsymbol{\mathcal{H}}$ fields always obey Maxwell's equations and are, therefore, not completely independent of one another. Magnetic polarisation is sometimes ignored, however, both because of the shared properties between electric and magnetic fields (general conclusions which one might draw about light's spatial electric polarisation structure often also apply to magnetic

polarisation), and because matter usually has a stronger response to the electric field, and subsequently to associated electric quantities (like electric canonical momentum and SAM densities) that tend to be the quantities measured experimentally in light-matter interactions.

The kind of polarisation shape that a field vector traces over time depends on whether the light field is comprised of more than one wavelength. Light from the sun, which contains the entire optical spectrum and more, is said to be unpolarised because so many frequency components are present that the electric field vector does not oscillate through a well-defined trajectory over time (there is an important distinction between 2D- and completely 3D-unpolarised light since far-field unpolarised light, while unpredictable, still must obey the rules of the paraxial regime and lie in a well-defined plane, transverse to propagation. This has interesting implications if paraxial unpolarised light is subsequently focussed to establish a longitudinal field component [70]). If we consider light of a single frequency (one colour), on the other hand, then at a single point in space both electric and magnetic field vectors sweep out an ellipse (the 'polarisation ellipse', whose trajectory can always be contained by a local 2D plane, even if the orientation of the ellipse varies arbitrarily from place to place in the field) over one wave period. This sort of light is said to be 'monochromatic'. Somewhere in-between unpolarised and monochromatic light are polychromatic fields, which contain a discrete number of frequency components greater than one. Polychromatic light has a well-defined polarisation—both $\boldsymbol{\mathcal{E}}$ and $\boldsymbol{\mathcal{H}}$ trace predictable shapes as the field oscillates—though it is markedly more complicated than that of the monochromatic case and depends strongly on the ratios between frequency components. Non-linear light-matter interactions can produce polychromatic fields, and bichromatic light composed of two colours has received much recent attention particularly because a bichromatic field of frequencies ω and

2ω is produced after second harmonic generation. In a paraxial field containing light with the two frequency components ω and 2ω, a variety of closed Lissajous curves are possible to be swept out by the electric field vector [81] (should the ratio between the two frequencies be irrational, the Lissajous curve never closes). Meanwhile, three-dimensional interference between waves with specially chosen frequency can give rise to polarisation shapes which are not confined to a 2D plane, and are chiral [82–84], perhaps even knotted [85]. This means that the electric field individually cannot be superimposed with its own mirror image at a given point in space, which is advantageous for chiral separation of small molecules that interact weakly with the magnetic field.

This thesis will focus only on the phase and polarisation structure of monochromatic light. Monochromatic fields are well-studied and widely implemented, yet despite being reasonably simple locally (i.e., drawing polarisation ellipses generically), often have a deeply complex polarisation spatial structure, especially in structured light and near fields where polarisation ellipses can be oriented in 3D and vary both in ellipticity and phase on subwavelength scales, and hold non-trivial properties which continue to be discovered today. Sometimes the spatial inhomogeneity of monochromatic light's polarisation is called its 'polarisation texture', something which while tightly coupled to the momentum of photons, can have skyrmionic properties [12, 15], and is interwoven with a tangle of topological defects called 'polarisation singularities'. The following sections in this chapter provide an in-depth background to the polarisation ellipse and the special cases of circular and linear polarisation which organise the polarisation singularities of general monochromatic fields. Light's polarisation topology changes radically between the paraxial and non-paraxial regimes, such as when transitioning from a source's near field to its far field, or when a focussed beam diffracts as it propagates. Two sections are dedicated to explain the

differences between the regimes and the role of the Poincaré sphere in paraxial light. Later sections outline vector topological defects more broadly, beyond polarisation singularities, when a three-component vector (that in light, could conceivably be any of the time-averaged vectors discussed last chapter) is zero.

3.1 The polarisation ellipse

So far in this chapter we have described polarisation as the trajectory followed by the time dependent electric field vector $\boldsymbol{\mathcal{E}}(\mathbf{r}, t)$ (or equivalently for the magnetic field). For monochromatic light where the trajectory over time of $\boldsymbol{\mathcal{E}}(\mathbf{r}, t)$ is rather simple, we can work with complex phasors which, between a real and imaginary vector, have encoded all the information about a field's spatial dependence of polarisation. We remind the reader that phasors, for which we use the non-scripted bold letters $\mathbf{E}(\mathbf{r})$ and $\mathbf{H}(\mathbf{r})$, are complex three-component vectors with no time dependence, for instance,

$$\mathbf{E}(\mathbf{r}) = \mathbf{p}(\mathbf{r}) + i\mathbf{q}(\mathbf{r}), \tag{3.1}$$

where $\mathbf{p}(\mathbf{r})$ and $\mathbf{q}(\mathbf{r})$ are real vector functions of space which relate to the time-dependent electric field vector via,

$$\boldsymbol{\mathcal{E}}(\mathbf{r}, t) = \Re\{\mathbf{E}(\mathbf{r})\mathrm{e}^{-i\omega t}\} = \mathbf{p}(\mathbf{r})\cos\omega t + \mathbf{q}(\mathbf{r})\sin\omega t. \tag{3.2}$$

Elliptical polarisation, its spatial variation and embedded singularities has on many occasions been explained using complex phasors [86–88], the original treatment of polarisation singularities given by Nye [89, 90]. In this section we adopt a similar notation to Dennis and Berry in their descriptions of the polarisation ellipse [16, 56, 91]. From Eq. (3.2) it is straightforward to see that for arbitrary vectors $\mathbf{p}$ and $\mathbf{q}$

which point in different directions and have different lengths, an ellipse is periodically drawn by $\boldsymbol{\mathcal{E}}(\mathbf{r}, t)$ in the plane normal to $\mathbf{p} \times \mathbf{q}$. Examples of this ellipse, which generically has any 3D orientation specified by $\mathbf{p}$ and $\mathbf{q}$, are shown in Fig. (3.1) in paraxial (where the 2D co-ordinate axes are aligned tangent to the plane of the ellipse) and non-paraxial regimes which we shall soon explain in more detail. The vectors $\mathbf{p}$ and $\mathbf{q}$ are related to the semi-axes of the ellipse, in that $\mathbf{E}$ can be multiplied by a certain complex number $\mathrm{e}^{i\chi_0(\mathbf{r})}$ to rectify $\mathbf{p}$ and $\mathbf{q}$, making them orthogonal, aligned to the ellipse's semi-major and semi-minor axes. Usually the phase angle $\chi_0(\mathbf{r})$ is called the rectifying phase, a position-dependent quantity because the complex number required to rectify $\mathbf{p}$ and $\mathbf{q}$ is different at each point in space, and is in fact given by,

$$\chi_0 = \frac{1}{2} \arctan \frac{2\mathbf{p} \cdot \mathbf{q}}{\mathbf{p} \cdot \mathbf{p} - \mathbf{q} \cdot \mathbf{q}} = \frac{1}{2} \arg \mathbf{E} \cdot \mathbf{E}. \tag{3.3}$$

The rectifying phase is calculated modulo π since the ellipse and its semi-axes (onto which $\mathbf{p}$ and $\mathbf{q}$ are rectified) are indistinguishable from themselves after rotation by π radians. When in three dimensions polarisation ellipses can take any orientation without restriction to a single plane, the rectifying phase χ_0 and the ellipse normal vector,

$$\mathbf{n} = \mathbf{p} \times \mathbf{q} = \frac{1}{2} \Im\{\mathbf{E}^* \times \mathbf{E}\}, \tag{3.4}$$

are two (usually) well-defined quantities that characterise the polarisation ellipse geometry, that is, χ_0 and $\mathbf{n}$ can both be calculated everywhere in arbitrary monochromatic fields (paraxial or non-paraxial) except where exact circular and linear polarisation occur. The normal vector $\mathbf{n}$ is proportional to the electric contribution of SAM density Eq. (2.24).

A circularly polarised electric field at some position $\mathbf{r}_\mathrm{c}$ produces one of the two extremities of the generic polarisation ellipse as, instead of an ellipse with an obvious

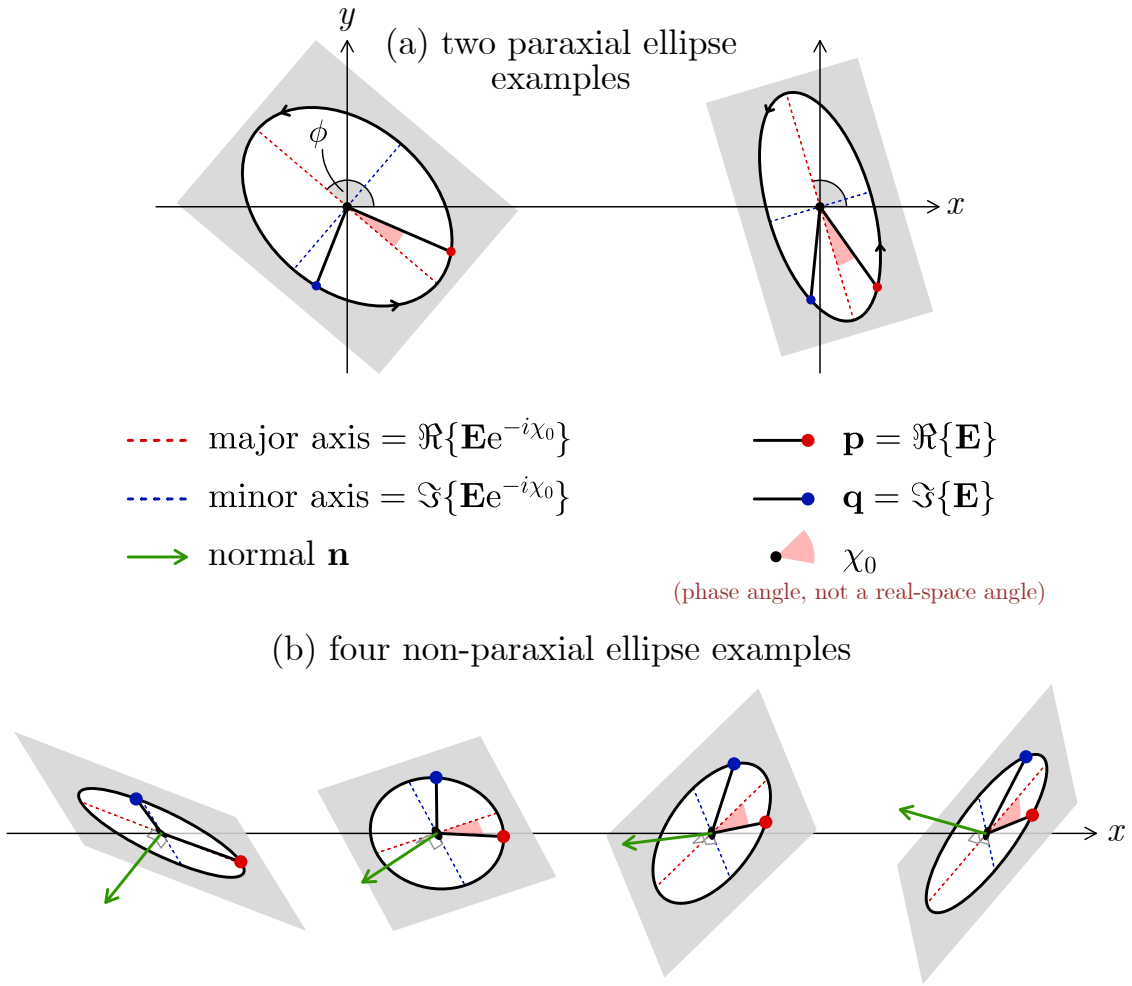

Figure 3.1: The polarisation ellipse traced in monochromatic light. Though they may rotate or vary in ellipticity polarisation ellipses in a paraxial field (a) lie in the same plane, here the xy plane, meaning one can consistently measure the major axis orientation angle ϕ and the ellipse handedness (arrows on the ellipse perimeter). Vectors $\mathbf{p} = \Re\{\mathbf{E}\}$ and $\mathbf{q} = \Im\{\mathbf{E}\}$ where $\mathbf{E}$ is the electric field phasor can be made right-angled and aligned to the ellipse semi-axes after rectifying $\mathbf{E}$ by a phase angle χ_0; $\mathbf{E} \to \mathbf{E}\exp(-i\chi_0)$. In non-paraxial light (b) ellipses may be oriented any way in 3D meaning a sense of rotation and the single angle ϕ are less simple to define consistently [92]. There are different ways to characterise 3D polarisation though two parameters which can be consistently calculated throughout (except at polarisation singularities) are the ellipse normal $\mathbf{n} = \mathbf{p} \times \mathbf{q}$ and rectifying phase $\chi_0 = (1/2)\arg \mathbf{E} \cdot \mathbf{E}$.

major and minor axis, a perfect circle is traced out by $\boldsymbol{\mathcal{E}}(\mathbf{r}_\mathrm{c}, t)$. This requires of the field phasor $\mathbf{E}(\mathbf{r}_\mathrm{c})$ that both $\mathbf{p}(\mathbf{r}_\mathrm{c})$ and $\mathbf{q}(\mathbf{r}_\mathrm{c})$ are equal in length and orthogonal. Consequently the rectifying phase is ill-defined—if $\mathbf{p}(\mathbf{r}_\mathrm{c})$ and $\mathbf{q}(\mathbf{r}_\mathrm{c})$ are equal and orthogonal, then they are rectified for any possible value of χ_0—which must mean that $\mathbf{E}(\mathbf{r}_\mathrm{c}) \cdot \mathbf{E}(\mathbf{r}_\mathrm{c}) = 0$ according to Eq. (3.3). We showed in Eq. (2.11) that the real and imaginary parts of $\mathbf{E} \cdot \mathbf{E}$ relate to the oscillating components of time-dependent electric energy density $(1/2)\epsilon_0 \boldsymbol{\mathcal{E}} \cdot \boldsymbol{\mathcal{E}}$ which are zero when, as in circular polarisation, the electric field vector keeps the same length over each period. Linear polarisation, meanwhile, occurs at positions $\mathbf{r}_\mathrm{l}$ where $\boldsymbol{\mathcal{E}}(\mathbf{r}_\mathrm{l}, t)$ oscillates along a straight line without any rotation to sweep out an elliptical trajectory. Because the instantaneous field vector no longer oscillates in a 2D plane, rather along a 1D line, the direction of the 'ellipse' normal $\mathbf{n}$ is undefined (a vector singularity). Mathematically $\mathbf{p}(\mathbf{r}_\mathrm{l})$ and $\mathbf{q}(\mathbf{r}_\mathrm{l})$ must be parallel for linear polarisation, such that $\mathbf{p}(\mathbf{r}_\mathrm{l}) \times \mathbf{q}(\mathbf{r}_\mathrm{l}) = \mathbf{0}$.

It may be tempting to think of states of circular and linear polarisation as typical in light, given that these states can be easily achieved experimentally in beams and because any arbitrary field can be realised by adding together circularly or linearly polarised plane waves with different wavevectors. From a purely topological perspective, however, circular and linear polarisation are special cases of the generic polarisation ellipse which the field vector traces out over one period. This generic behaviour of the electric field can be accessed in random plane wave interference, where there is very little spatial symmetry unlike in a beam or a single dipolar source. Polarisation circles and lines pose as defects in these general fields, each defect inscribing the field with a non-trivial arrangement of nearby polarisation ellipses. We will return in greater detail to the properties of these polarisation singularities in a later section of this chapter.

3.2 Paraxial polarisation and the Poincaré sphere

Diffraction, the spreading out of electromagnetic energy as light propagates, changes light's properties depending on the distance from its source or focus, transitioning from what is called the non-paraxial regime (e.g., near fields or a beam's focus) through to the paraxial regime (far fields). Between the two regimes light's polarisation and phase structure varies drastically, to the point where certain phenomena (spin-momentum locking effects [93], helicity-independent transverse spin [2, 52, 67], optical Möbius bands [94, 95], and many OAM-dependent chrioptical effects [96, 97] to name a handful) that are of enormous recent research interest are simply impossible or undetectable in a purely paraxial field. We will first focus on the polarisation properties of fields in the paraxial limit in this section.

Light is, broadly speaking, two-dimensional in the paraxial regime in that all polarisation ellipses lie in the same plane, the 'transverse plane', being transverse to the overall direction of propagation of the light field. In reality the paraxial regime is only *approached* in the far field region of a source or a diffracted beam; in physical paraxial fields the polarisation ellipse has a slight out-of-plane tilt due to longitudinal components belonging to both $\mathbf{E}$ and $\mathbf{H}$. That said, longitudinal field components causing this tilt are so small compared to the transverse field components as to be neglected (the only exceptional situation is when the transverse field components in a paraxial field are zero and dominated by longitudinal components. The whole of chapter 4 is dedicated to such a situation).

A major convenience afforded by the confinement of all polarisation ellipses to a 2D plane is the fact that polarisation can be consistently parameterised by four quadratic quantities, known as the Stokes parameters. This is because the polarisation ellipses at all points in space agree on a fixed reference frame from which to

define a handedness of rotation of the instantaneous field vector, the ellipse's ellipticity and the ellipse's orientation angle [see Fig. 3.1(a)]. The four Stokes parameters are denoted S_{0-3} and are defined in a fixed $\hat{\mathbf{x}}, \hat{\mathbf{y}}$ basis as,

$$\begin{aligned} S_0 &= |E_x|^2 + |E_y|^2, \\ S_1 &= |E_x|^2 - |E_y|^2, \\ S_2 &= 2\Re\{E_x^* E_y\}, \\ S_3 &= 2\Im\{E_x^* E_y\}, \end{aligned} \tag{3.5}$$

where for ease of interpretation we have defined S_{0-3} using the complex x and y components of the 2D electric field phasor, $\mathbf{E}_{2\mathrm{D}} = (E_x, E_y)$, meaning Eq. (3.5) is valid for a paraxial field propagating in the $\hat{\mathbf{z}}$ direction as is often the convention. The 0^{th} parameter relates to the field intensity in the transverse plane, the relative size of the ellipse, whereas the remaining three parameters relate to the intensity discrepancy between x and y components in the Cartesian basis (S_1), diagonal components in a diagonal basis (S_2), and left- and right-handed components in a circular basis (S_3). Together S_{1-3} inform the ellipticity, handedness, and orientation of all polarisation ellipses in the transverse xy plane, while holding the critical relation $S_0^2 = S_1^2 + S_2^2 + S_3^2$ that defines the 2-sphere. Any 2D polarisation with a particular ellipticity, handedness, and orientation can therefore be 'mapped' to an abstract space, defined by the orthogonal axes S_1, S_2 and S_3, as a single point on the surface of a sphere of radius S_0. Mapping to a 2D sphere surface upon which any position can be identified by two angles is indicative of 2D polarisation, with normalised amplitude, having two degrees of freedom. This abstract sphere is called the Poincaré sphere and is given in Fig. 3.2.

The Poincaré sphere's upper hemisphere belongs to right handed ellipses mean-

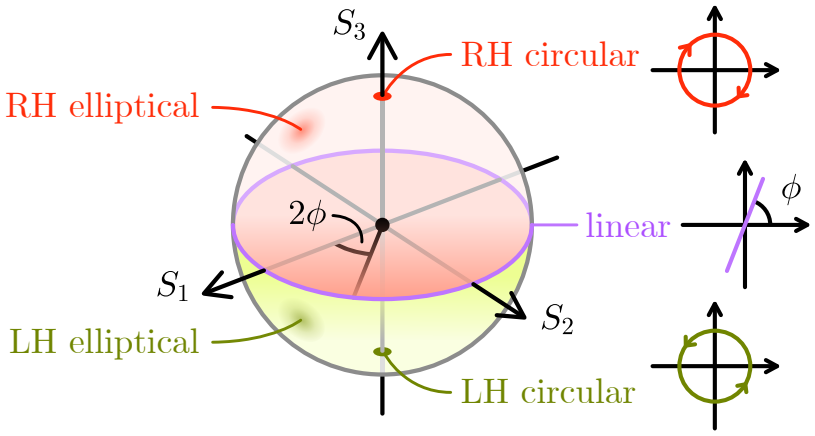

Figure 3.2: The Poincaré sphere, an intuitive way to characterise 2D polarisation. In paraxial light the polarisation ellipse at any single point in real-space maps to a single point on the Poincaré sphere, with the location on the sphere depending on ellipticity, handedness and orientation. Right-/left-handed polarisation ellipses map to the upper/lower hemispheres, regions separated by linear polarisation at the equator. Every fixed latitude corresponds to a fixed ellipticity. Completing a circuit around a latitude corresponds to a polarisation ellipse in real space rotating by π radians; the azimuth angle about the sphere's polar axis (S_3) is twice the real-space ellipse orientation angle ϕ. Right/left circular polarisation maps to the north/south pole.

ing the instantaneous field vector $\boldsymbol{\mathcal{E}}$ sweeps out the ellipse in an anticlockwise sense (when viewing the transverse plane such that the propagation direction points out-of-plane). Meanwhile the lower hemisphere contains left-handed, clockwise-rotating polarisation ellipses. The boundary separating the upper and lower hemispheres, the equator, corresponds to linear polarisation; as one travels around the equator, the line of polarisation rotates by π radians. In fact on any contour of constant latitude parallel to the equator a polarisation ellipse of fixed ellipticity undergoes this π radians rotation. Depending on its handedness, circular polarisation maps to the north or south pole of the Poincaré sphere.

To understand the relationship between how polarisation is organised in 2D paraxial fields and correspondingly on the Poincaré sphere we note that when mapped into another space via some function, a subspace's dimension generically stays the

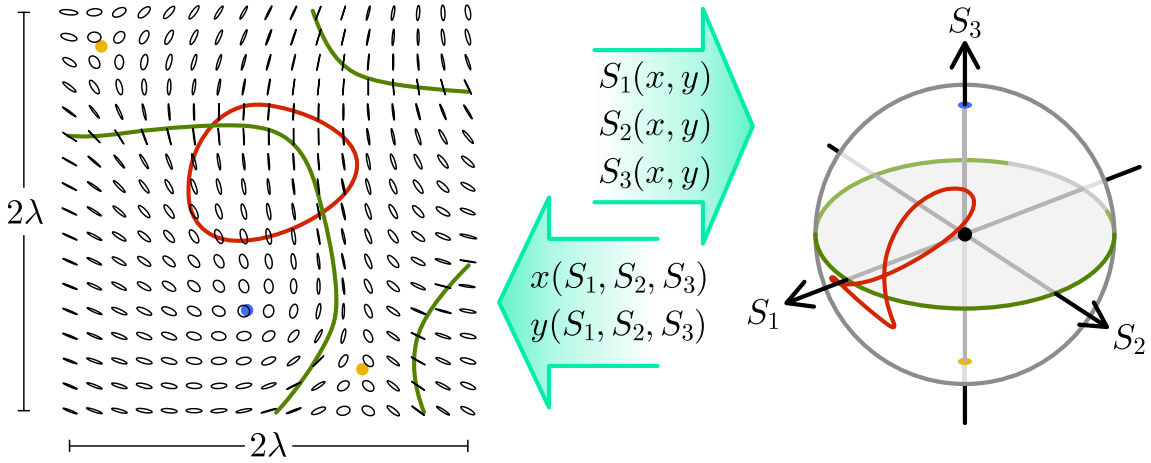

Figure 3.3: Mapping of 2D polarisation both ways between real space and the Poincaré sphere (Stokes space). The normalised Stokes parameters can be calculated from the complex E_x and E_y components, which are both functions of x and y, of a paraxial field propagating along z. An arbitrary line or closed loop drawn in the real-space paraxial field (red curve in the left plot) can be mapped to a line or closed loop on the Poincaré sphere. Conversely, points or lines on the Poincaré sphere map, by calculating the x and y co-ordinates as a function of S_i, to objects of the same dimension in real space. Special points or regions of the sphere, such as the poles (right-/left-circular polarisation) and a portion of the equator (linear polarisation), map to polarisation singularities in the paraxial field (blue/yellow circles are oppositely handed C points, green lines are L lines).

same. A subspace could simply be a straight line in a parameter space, say the a axis, which could be mapped to the xy plane by two functions $x = f_x(a)$ and $y = f_y(a)$ producing a curve A of connected (x, y) co-ordinates. The a axis is a 1D line, and after mapping to 2D real space via f_x and f_y, the curve A is also 1D having acquired the extra freedom to traverse the 2D plane spanned by x and y. The same concept applies to the Poincaré sphere as illustrated in Fig. 3.3. One could hand-draw a 1D path in the transverse plane of an arbitrary paraxial field, obtain the complex components E_x and E_y along that path, and from them calculate the Stokes parameters $S_{1-3}(E_x, E_y)$ to draw a corresponding 1D curve on the surface of the Poincaré sphere. In its entirety a paraxial field covers some portion of the Poincaré sphere surface. Inside the patch of polarisations on the Poincaré sphere that

exist in the paraxial field, an equivalent statement can be made that a point, curve or area of the Poincaré sphere surface maps back into objects of the same dimension in real space. With these arguments we can infer that of the two polarisation ellipse extremities circular polarisation, which maps to the Poincaré sphere poles (points), can only exist at points in the transverse plane (C points) while linear polarisation, spread across the entire equator (a line), is organised in lines in 2D real space (L lines).

Paraxial C points and L lines are topologically protected structures emerging in generic monochromatic interference (such as the polarisation field on the left of Fig. 3.3), which is to say that upon perturbation (addition of another interfering field), C points and L lines are merely displaced rather than destroyed. Quite remarkably paraxial polarisation singularities are 'stable' even when changing the line of sight of the field [98] (for instance if instead of viewing the field of Fig. 3.3 along the $\hat{\mathbf{z}}$ direction one's line of sight is tilted, C points appear to be displaced in the plane normal to the new line of sight).

3.3 Non-paraxial polarisation

The non-paraxial regime lifts the geometrical constraints placed on 2D paraxial polarisation as the electric and magnetic fields develop strong out-of-plane components. While in the last section we described polarisation ellipses that all lie (for purposes of explanation) on the xy plane, in a non-paraxial field, polarisation ellipses gain z components and complicate matters tremendously, being independently oriented any which way in 3D space [Fig. 3.1(b)]. The number of degrees of freedom of the ellipse double to four and for this reason it is notoriously challenging to draw a consistent mental image of non-paraxial polarisation in the same way as can be done using the

Poincaré sphere in paraxial light.

To construct a framework to parameterise 3D polarisation is an active area of research (though an in-depth discussion escapes the scope of this thesis). Three-dimensional polarisation can no longer be expressed by the four 2D Stokes parameters Eq. (3.5), but can be by nine generalised parameters [99]—though it is difficult to construe these parameters geometrically like Eq. (3.5). One could, alternatively, approach 3D-oriented polarisation by defining the plane of the ellipse using two angles and within this plane, return to 2D stokes parameters (or equivalently, two more angles) to characterise the ellipse's ellipticity and in-plane orientation [37, 100]. Other proposals, namely the Majorana sphere [101] and Poincarana sphere [102], retain a more palatable unit sphere (this time in real space) but account for additional degrees of freedom by assigning two points on the sphere per 3D polarisation ellipse (as opposed to one point per 2D ellipse on the Poincaré sphere). For a more detailed summary, see [92] (which also describes a statistical unit sphere approach to classify 3D polarisation).

Two quantities, the ellipse normal Eq. (3.4) $\mathbf{n}$ and rectifying phase χ_0 Eq. (3.3), can often provide a sufficient picture of how 3D polarisation ellipses are arranged because even in non-paraxial light, $\mathbf{n}$ is ill-defined wherever polarisation is linear, and similarly for χ_0 wherever polarisation is circular. These stable singularities reveal a polarisation skeleton in non-paraxial fields, built of strands of pure linear polarisation (L lines) and strands of pure circular polarisation (C lines) [56, 89, 90]. The reason for the dimension of these polarisation singularities is the number of mathematical criteria (two each) that they satisfy versus the number of spatial dimensions that they exist in: specifically, L lines must obey $p_x/q_x = p_y/q_y = p_z/q_z$ while C lines satisfy $\Re\{\mathbf{E}\cdot\mathbf{E}\} = \Im\{\mathbf{E}\cdot\mathbf{E}\} = 0$, both sets of two scalar conditions [90] which subtracted from three spatial dimensions $3 - 2 = 1$ results in a one-dimensional structure. In

paraxial light where all polarisation sits in the same plane, the number of important spatial dimensions is reduced to two such that circular polarisation occurs at points and that linear polarisation, which now only meets one condition $p_x/q_x = p_y/q_y$, is still found in continuous lines. The number of real scalar conditions that must be imposed on the electric field phasor at the location of a singularity can informally be interpreted as the singularity's codimension—so in non-paraxial light, C lines and L lines are both codimension 2 objects.

3.4 Imprints of polarisation singularities

Every polarisation singularity disturbs nearby polarisation ellipses in a special way depending on which aspect of the polarisation ellipse is ill-defined by the singularity. Polarisation circles do not have major and minor axes and so in the plane of circular polarisation (in paraxial fields this is simply the transverse plane while in non-paraxial fields, the plane of polarisation, normal to $\mathbf{n}$, is defined locally to each point on the line as polarisation circles have inconstant orientation), nearby polarisation ellipses conform to ensure a smooth surrounding circulation of major and minor axes by rotating, in an (anti)clockwise sense, a multiple of π radians as shown in Fig. 3.4 in both paraxial and non-paraxial cases (an ellipse needs only to rotate by π radians to align with its non-rotated self). In a closed loop around a C line or C point, the sense and number of π radians rotations of ellipses undergone relative to the direction of travel along the loop is its topological index I_c, a parameter to differentiate between these two possible states and for which Berry provided a straightforward formula [103],

$$I_\mathrm{c} = \frac{1}{2}\mathrm{sign}(|\mathbf{E}^* \cdot \nabla(\mathbf{E} \cdot \mathbf{E})|^2 - |\mathbf{E} \cdot \nabla(\mathbf{E} \cdot \mathbf{E})|^2). \tag{3.6}$$

In Fig. 3.4(a) there are three paraxial C points shown by the filled red, blue and green circles, around which rectangular circuits are drawn. Traversing the red circuit in the clockwise direction, the ellipses appear to rotate anticlockwise by one half turn (π radians) giving the red C point an index of $-1/2$. The same is true of the green C point while the blue C point has an opposite $+1/2$ index. If a circuit is drawn around multiple C points, the sum of the indices of the individual enclosed C points is the index of the circuit (see the gold circuit of Fig. 3.4(a) which contains oppositely signed C points and has an overall index of 0). Plotting integral curves of the major axes of polarisation ellipses in the plane of circular polarisation one sees that either one or three curves terminate at the singularity depending on the sign of the index—integral curves are organised in one of three possible structures, named lemon (index $+1/2$, 1 terminating line), star (index $-1/2$, 3 terminating lines), and monstar (index $+1/2$, 3 terminating lines) [91, 104]. A unique characteristic of non-paraxial C lines arises from significant out-of-polarisation-plane field components which causes, in an enclosing circuit, polarisation ellipses to undergo a half turn in 3D and construct a Möbius band [94, 95].

The singular property of linear polarisation is the direction of the normal vector $\mathbf{n}$ to the non-present ellipse (the normal to a line is not defined), a vector proportional to the electric SAM density $\mathbf{S}_\mathrm{e}$ which circulates in some manner around L lines. Either side of an L line in paraxial light the normal vector, defined via the right hand rule, points in the opposite directions into or out of the transverse plane so that L lines act as boundaries between left and right handed (with respect to the uniform overall propagation direction) polarisation ellipses. Due to the coupling of far field electric and magnetic polarisation structures L lines in paraxial fields also coincide with the phase singularities of the complex scalar field $\mathbf{E}^*\cdot\mathbf{H} = \Re\{\mathbf{E}^*\cdot\mathbf{H}\}+i\Im\{\mathbf{E}^*\cdot\mathbf{H}\}$. At any point along its length a non-paraxial L line creates a smooth rotation of $\mathbf{n}$ of nearby

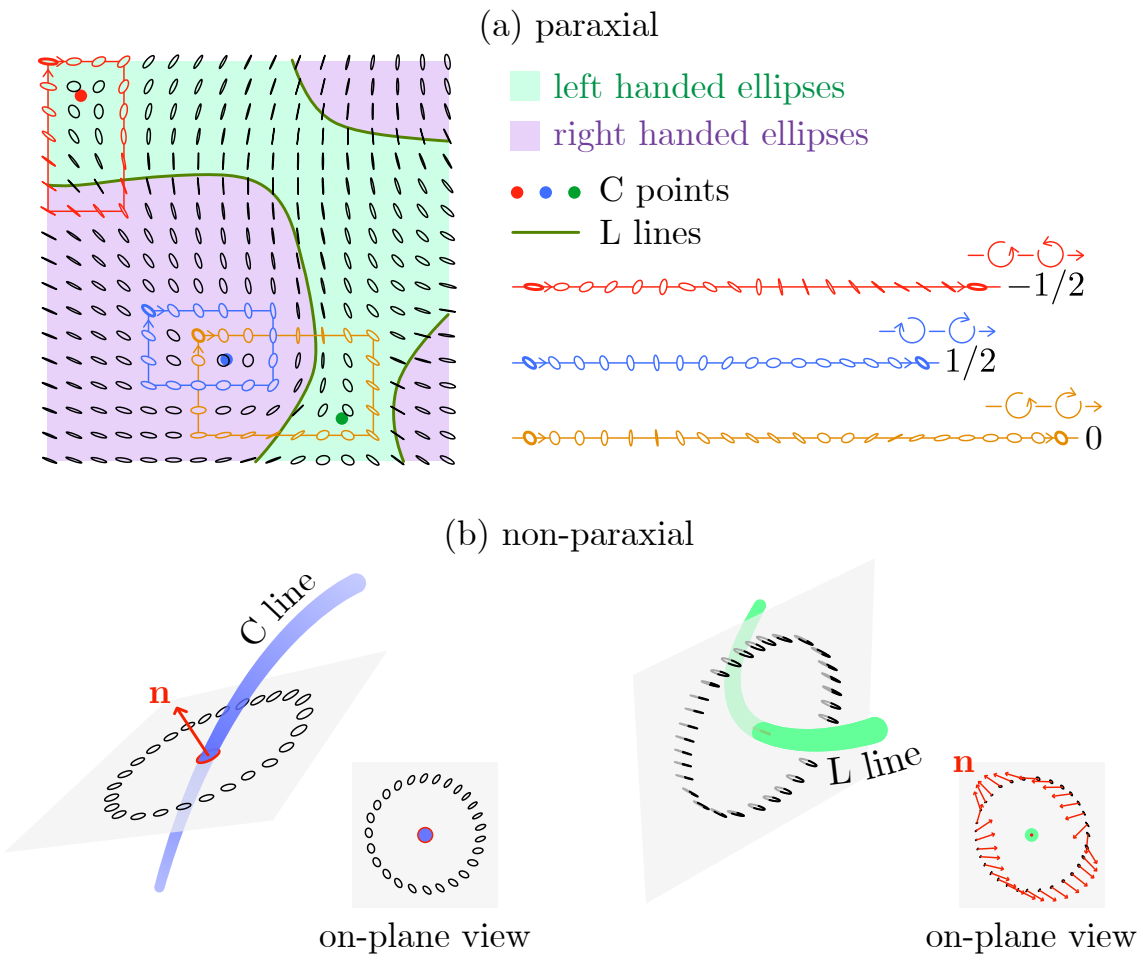

Figure 3.4: The polarisation imprint in general paraxial (a) and non-paraxial (b) fields of circular and linear polarisation singularities. Paraxial light (a) contains C points and L lines (see Fig. 3.3). C points disturb nearby polarisation ellipses by, along any closed circuit containing one C point, causing them to turn by an integer multiple of π radians. Three C points (red, blue and green circles) are shown in the paraxial field on the left of (a) as well as three closed circuits (red, blue and gold lines) that sample the paraxial polarisation and which are unravelled in the key to the right of (a). The red C point causes ellipses to rotate by π radians anticlockwise, gaining a $-1/2$ index as shown by the red circuit, arranging ellipse major axes in a 'star' pattern (this is true of the green C point too). The blue C point has a $+1/2$ index as ellipses on the blue circuit rotate π radians clockwise (a 'lemon' pattern is produced). Both the blue and green C points are enclosed by the gold circuit whose ellipses do not undergo a net rotation because the indices of the two enclosed C points cancel out. For non-paraxial light (b), C lines cause a rotation of polarisation ellipses in the plane of polarisation local to each point along the line (Möbius bands are swept out by the major axes due to out-of-plane field components). L lines cause the normal vector of nearby ellipses to rotate in the plane normal to the electric field vector, local to points on the L line.

(very slight) ellipses in the plane normal to the oscillation direction, the polarisation line, with either clockwise or anticlockwise sense with respect to the direction of travel along an L-line-enclosing loop (Fig. 3.4 also visualises these features).

3.5 Optical vortices

Scalar phase singularities exist in complex scalar fields, such as $\phi = a+ib$, when both its real and imaginary parts vanish and leave the field's phase angle $\arg\phi = \chi$ undefined. A phase singularity is ordinarily a thread-like 1D structure in 3D real space (codimension 2) because $\Re\{\phi\} = \Im\{\phi\} = 0$ totals *two* constraints which with *three* space parameters (x, y, z), can be maintained with one freely varying spatial degree of freedom left over that sweeps out the length of the thread. Having an undefined phase angle the singularity twists the surrounding field into a vortex, in particular χ is forced to wind around the singularity an integer multiple l, its topological charge, of 2π times. Because the phase vortex persists along the length of the singularity strand, unchanging in strength and handedness, the phase singularity's index l can be found formally by drawing a closed loop C around any part of the singularity and integrating $\nabla\chi$ in a certain direction along the loop [16],

$$l = \frac{1}{2\pi}\oint_C \nabla\chi \cdot d\mathbf{r} \tag{3.7}$$

where Eq. (3.7) returns an integer. Monochromatic light's field phasor components are individually complex scalar fields which generically contain phase singularities. What is significant about optical phase singularities is that the phase gradient of an electric field component contributes towards the canonical momentum of light and radiation pressure force, a pushing force from photons felt indiscriminately by

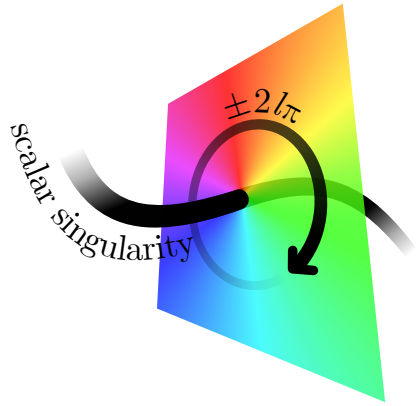

Figure 3.5: A scalar wave dislocation or scalar vortex line, an optical vortex in a complex scalar field ϕ. The vortex line pierces a plane on which the phase angle of the field, $\arg\phi$, is plotted, showing a smooth azimuthal change in phase. Integrating the phase gradient clockwise over a loop enclosing the singularity line returns an integer l (the topological charge) multiple of 2π. Adapted from [20].

all kinds of matter. If a phase singularity causes the scalar field's phase in the surrounding space to increase azimuthally, then it is possible for canonical momentum to acquire an azimuthal component and for a light field to develop orbital angular momentum, centred on a phase singularity—an optical vortex.

Of course $\mathbf{E}$ as a whole is a vector field and a phase singularity in a single field component, say $E_x = 0$, does not in general amount to a vortex of momentum which is proportional to a weighted average of the gradient of all three components [via $\mathbf{E}^* \cdot (\nabla)\mathbf{E} = E_x^* \nabla E_x + E_y^* \nabla E_y + E_z^* \nabla E_z$ in the electric canonical momentum, Eq. (2.15)]. However, it is possible to design cylindrically symmetric light, propagating in a well-defined overall direction, in which phase singularities of more than one field component are aligned to create a beam carrying orbital angular momentum. These beams are the vortex beams we mentioned previously and have become very well-established in optics since they were popularised during the 1990s. We said that vortex beams can carry information in their spatial phase [8, 9] and polarisation

structure and twist particles onto orbiting trajectories, but even from a purely theoretical perspective, focussed vortices have a deep and rich physics particularly in 3D polarisation and the complicated interplay of helices in light [76, 83, 105]: those (orbit-related) of sculpted phase fronts and those (spin-related) which are drawn out by the electric field vector.

3.6 Vector singularities in general

Polarisation singularities are special examples of a wider class of the vector singularity that emerges in a real vector field $\mathbf{V}$ when $\mathbf{V} = \mathbf{0}$ and the direction of the $\mathbf{V}$ arrow is unspecified. A general, real, and 3D vector field whose components do not depend on each other actually vanishes at 0D points because $V_x = V_y = V_z = 0$ comprise three real scalar conditions, but geometric constraints mean both circular and linear polarisation singularities turn out to be 1D line structures, not points, in 3D real space. Point-like vector singularities do, however, occur in many other electromagnetic quantities in light such as the instantaneous electric field $\boldsymbol{\mathcal{E}}$, the Poynting vector $1/2\ \Re\{\mathbf{E}^* \times \mathbf{H}\}$ or the *total* SAM density $\mathbf{S} = \mathbf{S}_\mathrm{e} + \mathbf{S}_\mathrm{m}$ [71], to name a few. These point-like singularities stir up the surrounding vector field, creating a distinct imprint which we will quantify in this section, and share many of the same properties of optical skyrmions [106] (the name 'optical skyrmion' encompasses skyrmions in different vector fields including the instantaneous electric field and electric spin, and even in polarisation ellipses [12, 107, 108]. Most famously 'skyrmion' refers to the topologically protected quasiparticle formed in chiral magnets [109–111]).

To understand how a point-like vector singularity $\mathbf{V} = \mathbf{0}$ disturbs the rest of $\mathbf{V}$ it is useful to draw upon the lower-dimensional analogy of the optical vortex. A phase vortex forces the scalar field's phase angle $\arg \phi$, wrapping around the singularity, to

advance through every possible value between 0 and 2π at least once. Likewise in 3D space a point-like vector singularity $\mathbf{V} = \mathbf{0}$ forces, on a surface A enclosing the point-singularity where the real vector $\mathbf{V}$ is non-zero, that the arrow representing $\mathbf{V}$ realises every 3D orientation an integer number of times (this is the magnitude of the singularity's index). One could point their finger any way in 3D and somewhere on A, the vector $\mathbf{V}$ is pointing in that exact direction. Though it is much more difficult to picture mentally, $\mathbf{V}$ also 'winds' in orientation over this singularity-enclosing surface with a certain sense, once again corresponding to the sign of the singularity index as in the scalar case. In much the same way a two-dimensional optical skyrmion can be interpreted as a vector realised in every orientation on a closed surface in parameter space (for instance the Stokes vector calculated in a 2D polarisation skyrmion which wraps, pointing radially, over the Poincaré sphere).

For the above reasons, we cannot use a similar expression to Eq. (3.7) to calculate a vector point-singularity's topological index—a 1D closed loop will not properly enclose a point-like singularity and capture its effect on the surrounding vector field $\mathbf{V}$, rather, we must integrate over the 2D closed surface A in a higher-dimensional definition. The vector singularity's topological index is equivalent to the skyrme number [106, 109], and, if we take A to be a sphere surface, is defined as,

$$n = \frac{1}{4\pi} \int_A \mathbf{V} \cdot \left(\frac{\partial \mathbf{V}}{\partial \theta} \times \frac{\partial \mathbf{V}}{\partial \phi} \right) dA, \tag{3.8}$$

which returns an integer whose magnitude is the order of the singularity. The order of a singularity in $\mathbf{V}$ has implications for the derivatives of $\mathbf{V}$ at the singularity location, because for order m, the $(m-1)^{th}$ order derivatives must be zero (so for a first-order singularity $|n| = 1$, only the components of $\mathbf{V}$ are zero while $\nabla \mathbf{V} \neq \mathbf{0}$). Both a vector point-singularity and skyrmion have other characteristics, relating to

the net flow of streamlines through the singularity, which escape Eq. (3.8) and are calculated separately. But first-order singularities can, conveniently, be completely characterised by the vector's Jacobian matrix as we will next explain. A first-order singularity is arguably of most interest since it is the most stable, due to $\mathbf{V}$ vanishing without imposing any further mathematical conditions on the field derivatives at the singularity location.

3.6.1 First-order vector singularities

While Eq. (3.8) is valid for arbitrary order, it is perhaps simpler for first-order singularites where $n = \pm 1$ to instead consider the field's Jacobian matrix which contains all necessary information on the singularity. Jacobian matrices are used repeatedly throughout this thesis and are N-dimensional analogues to the scalar derivative (for instance in one dimension, $df = (df/dr)dr$ whereas in N dimensions, $d\mathbf{f} = (d\mathbf{f}/d\mathbf{r})\cdot d\mathbf{r}$, $d\mathbf{f}/d\mathbf{r}$ being the Jacobian matrix). In three-dimensions a Jacobian matrix is 3×3 in size, defined for a vector $\mathbf{V} = (V_x, V_y, V_z)^T$ as,

$$\mathbf{J} = (\nabla \mathbf{V})^T = \begin{pmatrix} \frac{\partial V_x}{\partial x} & \frac{\partial V_x}{\partial y} & \frac{\partial V_x}{\partial z} \\ \frac{\partial V_y}{\partial x} & \frac{\partial V_y}{\partial y} & \frac{\partial V_y}{\partial z} \\ \frac{\partial V_z}{\partial x} & \frac{\partial V_z}{\partial y} & \frac{\partial V_z}{\partial z} \end{pmatrix}. \tag{3.9}$$

The Jacobian matrix is what determines how the vector field $\mathbf{V}$ behaves over small distances $\Delta\mathbf{r}$ where first-order derivatives dominate in the Taylor expansion of $\mathbf{V}$, which is to say $\mathbf{V}(\mathbf{r} + \Delta\mathbf{r}) \approx \mathbf{V}(\mathbf{r}) + \mathbf{J}\Delta\mathbf{r}$. It is particularly important evaluated at the location of a singularity $\mathbf{r} = \mathbf{r}_z$ where $\mathbf{V}(\mathbf{r}_z) = \mathbf{0}$, and hence $\mathbf{V}(\mathbf{r}_z + \Delta\mathbf{r}) \approx \mathbf{J}\Delta\mathbf{r}$, because its three eigenvalues correspond to the singularity index and the flow of $\mathbf{V}$ streamlines, while its eigenvectors inform the 'principle axes' of the structure

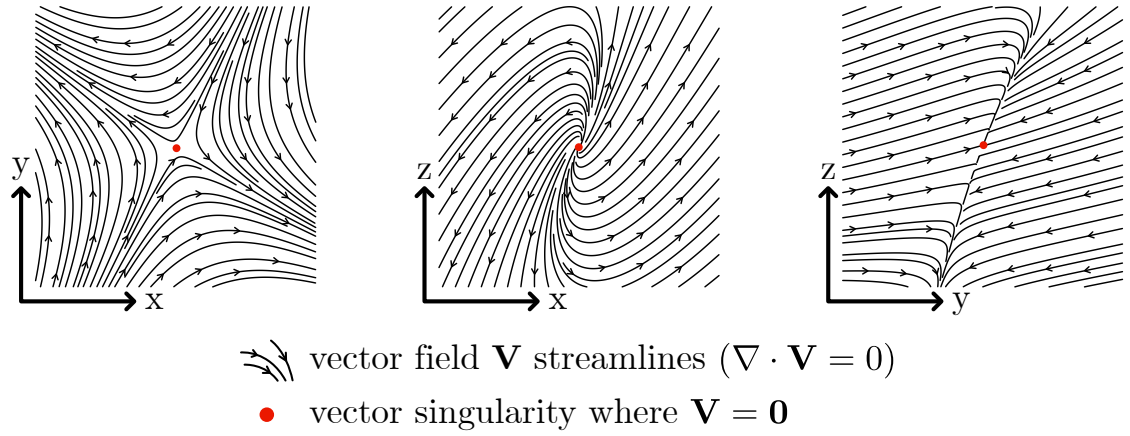

Figure 3.6: Three cut planes of a vector field $\mathbf{V}$ containing a first-order direction singularity (red circle) where $\mathbf{V} = \mathbf{0}$. In this case the vector field has zero divergence meaning the singularity must be a vector saddle point, characterised by Jacobian eigenvalue signs of $(+,+,-)$ or $(+,-,-)$. In the xy plane integral curves of the field appear to be deflected from the singularity (which seems reasonable given $\nabla \cdot \mathbf{V} = 0$), while on the central xz plane $\mathbf{V}$ streamlines appear to emanate from the singularity, apparently in contradiction to $\nabla \cdot \mathbf{V} = 0$. In fact the true flow of $\mathbf{V}$ through the singularity can only be comprehended in 3D—apparent net outward flow like in the xz plane is compensated by inward flow in other directions.

of the nearby flux of $\mathbf{V}$, which may resemble that of Fig. 3.6. Multiplying the eigenvalues of $\mathbf{J}$ gives its determinant, whose sign ($+$ or $-$) is equivalent to the first-order singularity's index ($+1$ or -1),

$$n = \pm 1 \equiv \text{sign}(\det \mathbf{J}). \tag{3.10}$$

A Jacobian matrix in three dimensions has three eigenvalues meaning a $+1$ index can be realised by signed eigenvalues of $\text{sign}(e_i) = (+,+,+)$ or $(+,-,-)$ in any order—two situations which are topologically distinct despite sharing the same overall index. That a singularity's Jacobian matrix with $\text{sign}(e_i) = (+,+,+)$ is a vector source with non-zero divergence of $\mathbf{V}$, while $\text{sign}(e_i) = (+,-,-)$ corresponds to a vector saddle point which could satisfy $\nabla \cdot \mathbf{V} = 0$ is why calculating the singularity index n alone is often insufficient, especially when dealing with electromagnetic vectors some of which

in free space are divergence-free, but not others. Likewise a negative singularity index is assigned to both vector sinks $(-,-,-)$ and saddle points $(+,+,-)$ (which is a *different* saddle point to one with $(+,-,-)$ eigenvalue signs due to the odd number of spatial dimensions).

These concepts are used extensively in chapter 5 of this thesis where three-component electric field phasor zeros $\mathbf{E} = \mathbf{0}$ are studied in depth. Full electric field singularities are special by being 3D confined in near fields and by being automatically coupled to point-like singularities in other electromagnetic vectors such as the (real and imaginary) Poynting vector, and canonical and spin momentum, each of which can be classified by calculating the eigenvalues of their Jacobian matrices.

3.7 Chapter summary

In this chapter we have reviewed how electromagnetic vectors behave locally and globally in monochromatic light, most notably locally that 'polarisation ellipses' with an associated rectifying phase and ellipse normal vector are drawn at each point by the electric and magnetic fields in space, and globally that over space, polarisation ellipses are organised into strands of constant ellipticity [12, 107] whose extremes are C lines and L lines. The phase gradient of an electromagnetic field is proportional to the direction of canonical momentum and when field components are suppressed, establishing dark spots, the phase gradient diverges and can acquire an azimuthal component in nearby space indicative of helical, vortex wavefronts. Depending on how constrained its polarisation and phase structure is light falls into one of two regimes, namely the paraxial regime when all polarisation ellipses lie flat in a single plane transverse to propagation (which is largely in one direction), and the non-paraxial regime when polarisation is inhomogeneous, freely oriented in 3D, and the

field's phase gradient is defined locally. In non-paraxial light vortex strands and polarisation singularities are continuous, stable singularities that either extend infinitely in space or form (un)knotted closed loops [6, 112–114]. What is so compelling about the study of the singularities and spatial structure of monochromatic light is that many of its findings are applicable to wave fields *in general*. For it was initially realised that waves ordinarily contain topological defects in phase fifty years ago in a study of ultrasound waves [3] and since then and the explosion of research that followed the discovery of orbital angular momentum in light, analogies to many of the phenomena in this chapter have been predicted or shown to exist in acoustic [18], water [18, 19], and even gravitational waves [17]. The next chapter is the first of four presenting original findings, its focus dark spots in paraxial fields.

Chapter 4

Paraxial dark spots

We mentioned in chapter 3 that the paraxial regime is one of restricted physics where light can be considered to be two-dimensional, and to be propagating in a single well-defined direction. Polarisation ellipses of both electric and magnetic fields are constrained to lie tangent to the two-dimensional plane transverse to this overall propagation direction (the 'transverse plane'). Longitudinal field components, while only ever truly zero in plane waves (which cannot be physically realised), are so small compared to the transverse field components as to be ignored. The paraxial regime is reached in the far field of *absolutely any* localised source.

That the source is localised is key. In practice we cannot build sources of light that are infinite in extent and driven with infinite power; any source which we can feasibly create, be it a light bulb, a dipole antenna, or a laser, radiates electromagnetic energy which *must* spread out eventually. Some solutions to Maxwell's equations, such as plane waves and Bessel beams, carry infinite energy—this energy, while non-physical, does not strictly speaking spread out in space, but the propagating fields that carry it can only be generated exactly by an infinite source. With

more precise terminology the inevitable spreading of energy over space is known as diffraction and occurs because, given enough distance, any physical source of light appears to be point-like and radiating with spherical wavefronts that grow in size as they propagate. The far field region where wavefronts become spherical is approached only after several wavelengths' distance from the source. Zooming in on an almost-planar patch of one of these far field spherical wavefronts, one sees that the light's polarisation structure is paraxial.

Focussing on phenomena in the paraxial regime this chapter is the first of four that report the findings of our recent publications and the first of three which treat vectorial electric field dark spots (where two or more components of the $\mathbf{E}$ phasor vanish) in light. Dark spots have a remarkable ability to imbue light with surprising, even counter-intuitive properties and a far field dark spot, in spite of the rules of paraxiality, is no exception. We consider a paraxial dark spot at some location $\mathbf{r}_\mathrm{z}$ to be a null in both the transverse field components, $\mathbf{E}_\mathrm{t}(\mathbf{r}_\mathrm{z}) = \mathbf{0}$, that normally carry the majority of a far field's energy density but must become comparable to the radial field near to $\mathbf{r}_\mathrm{z}$ as they approach zero. The result is a small and very dim non-paraxial region around $\mathbf{r}_\mathrm{z}$ where polarisation is 3D and, as we shall see, non-diverging polarisation singularities and other structures emerge. Our findings in *Non-diffracting polarisation features around far-field zeros of electromagnetic radiation* [21] are presented here, a significant generalisation of a result which was reported for a vortex beam by Afanasev et al. [115] and had also been observed on the axis of a linearly polarised dipole [116]. The existence of these phenomena is contingent on the different dependence of the amplitude of the transverse and radial field components on the radial distance from the source, which we shall explain next.

4.1 Radiation diagrams and dark spots

Spherical wavefronts set out an important simplification in defining a far field electromagnetic field analytically in a spherical co-ordinate system with the parameters (r, θ, ϕ) representing radial distance, and elevation and azimuth angles. All advancing of phase is accounted for by a single $\exp(ikr)$ factor, and since in the paraxial limit longitudinal (radial) field components are small, it is often sufficient to express only the transverse field phasor $\mathbf{E}_\mathrm{t}$ via a radiation diagram*,

$$\mathbf{E}_\mathrm{t} = \begin{pmatrix} E_\theta(r,\theta,\phi) \\ E_\phi(r,\theta,\phi) \end{pmatrix} = \begin{pmatrix} f_\theta(\theta,\phi) \\ f_\phi(\theta,\phi) \end{pmatrix} \frac{\mathrm{e}^{ikr}}{r}. \tag{4.1}$$

Since both transverse field component amplitudes E_θ and E_ϕ obey a simple $1/r$ radial dependence, it is possible to completely segregate the radial dependence of $\mathbf{E}_\mathrm{t}$ by defining as above two functions, f_θ and f_ϕ, which depend only on the elevation and azimuth angles and can fully describe the far field radiation of any source. A linearly polarised dipole, for instance, is expressed in the far field by $E_\theta = f_\theta \exp(ikr)/r = E_0 \sin\theta \exp(ikr)/r$ and $E_\phi = 0$ as illustrated in Fig. 4.1.

As with any typical function, the transverse field components contain zeros in general where both real and imaginary parts vanish, comprising two conditions for a zero in one of f_θ or f_ϕ. In a 3D parameter space (r, θ, ϕ) a zero in complex scalar field organises a line (since three parameters minus two real conditions that set the field's real and imaginary parts to zero equals one, the dimension of the structure) which intersects a fixed-radius sphere at a point—hence the zeros in $f_\theta(\theta, \phi)$ and $f_\phi(\theta, \phi)$ are points (these concepts are well-known and a substantial body of work exists on

*The radiation diagram is a θ, ϕ space representation of the far field of a source (here simply referring to the functions f_θ, f_ϕ) and is used frequently in engineering.

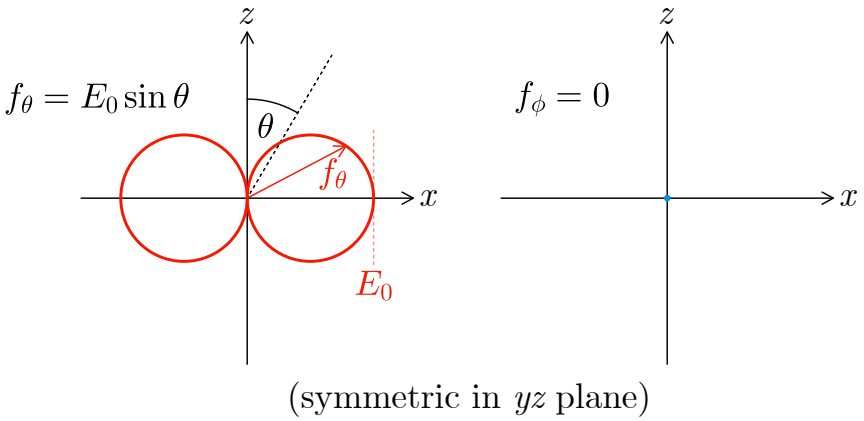

Figure 4.1: Radiation diagrams of the $\hat{\boldsymbol{\theta}}$ (left) and $\hat{\boldsymbol{\phi}}$ (right) dipole component amplitudes (excluding radial dependence $\exp(ikr)/r$). Only the $\hat{\boldsymbol{\theta}}$ component is non-zero, varying according to $f_\theta = E_0 \sin\theta$ which is plotted in red in the left plot; the radial distance of the red curve from the centre of the plot corresponds to f_θ and vanishes at $\theta = (0, \pi)$, the location of the dipole's axial dark spot. The angle θ is measured with respect to the $+z$ axis; cartesian x and z axes are superimposed for visual reference. Since the dipole's field is independent of ϕ the plots are rotationally symmetric about z.

scalar vortex lines in light). Should $f_\theta = 0$ and $f_\phi = 0$ coincide at the same (θ, ϕ) coordinates, then a time-fixed dark spot emerges (the longitudinal radial component is very small and does not contribute a significant intensity). A paraxial dark spot will not, however, appear organically unless the field has a high degree of symmetry, and otherwise requires that $f_\theta = 0$ and $f_\phi = 0$ are forced at the same position artificially (see chapter 6). The linearly polarised dipole is an example of a highly symmetric far field containing a transverse field zero at $\theta = 0$.

Thus far we have neglected the radial electric field component E_r. While it is perfectly reasonable to only consider a source's radiation diagram if we are interested in the field's energy density, Eq. (4.1) does not provide a comprehensive description of far field polarisation if there is a paraxial dark spot. This is because polarisation depends on the *relative* amplitude and phase of each field component and by definition in the neighbourhood of a paraxial zero, the transverse field, ordinarily

dominant, becomes comparable to the radial field which is required by Gauss' law to be non-zero as long as $\mathbf{E}_\mathrm{t}$ is not trivially zero everywhere in space. In some perhaps confusing sense, polarisation near to a paraxial zero is inherently non-paraxial. Gauss' law $\nabla \cdot \mathbf{E} = 0$ (where $\mathbf{E} = \mathbf{E}_\mathrm{t} + E_r\hat{\mathbf{r}}$) offers a way to obtain E_r from a differential equation using the far field terms of $\mathbf{E}_\mathrm{t}$. The solution of $\nabla \cdot \mathbf{E} = 0$ using Eq. (4.1) takes the form,

$$E_r(r,\theta,\phi) = \frac{const}{r^2} + \frac{i}{kr}\left(\frac{1}{\tan\theta}E_\theta + \frac{1}{\sin\theta}\frac{\partial E_\phi}{\partial\phi} + \frac{\partial E_\theta}{\partial\theta}\right). \tag{4.2}$$

For our purposes we may ignore the first (constant) term because it accounts for non-radiating static charge. Substituting expressions for E_θ and E_ϕ from Eq. (4.1) we may find the r-independent function f_r,

$$f_r(\theta,\phi) = \frac{i}{k}\left(\frac{1}{\tan\theta}f_\theta + \frac{1}{\sin\theta}\frac{\partial f_\phi}{\partial\phi} + \frac{\partial f_\theta}{\partial\theta}\right). \tag{4.3}$$

with which the radial dependence of E_r can be written explicitly:

$$E_r(r,\theta,\phi) = f_r(\theta,\phi)\frac{\mathrm{e}^{ikr}}{r^2}. \tag{4.4}$$

By calculating E_r we arrive at a surprising relationship between the transverse and radial components of far field radiation: while in the radial direction the transverse components reduce by $1/r$ [Eq. (4.1)], the radial component falls in amplitude by $1/r^2$. We shall explain in the following section the striking implication of this result, that is the capacity to identify 3D polarisation structures near to a paraxial dark spot which keep the same real-space separation independently of the growing size of the spherical wavefronts, and hence, may be described as non-diffracting.

4.2 Non-diffracting polarisation objects

Many physical quantities in light are quadratic with respect to the electric and magnetic fields. This is immediately noticeable in chapter 2 after the time-averaged Poynting vector, SAM density, canonical momentum, energy and helicity densities were each defined by, under some vector operation, multiplying $\mathbf{E}$ and $\mathbf{H}$ once with themselves or their conjugates or each other. Of the scalar quadratic quantities, electric energy density is proportional to intensity $\mathbf{E}^* \cdot \mathbf{E}$ and always greater than zero, increasing in all transverse directions from the minima of a paraxial zero, and may be separated into transverse and radial contributions $\mathbf{E}^* \cdot \mathbf{E} = \mathbf{E}_\mathrm{t}^* \cdot \mathbf{E}_\mathrm{t} + E_r^* E_r$. We learned last section that $\mathbf{E}_\mathrm{t}$ and E_r behave differently in the far field while wavefronts inflate and so in making this transverse-radial intensity separation near to a paraxial zero, it is possible to identify a non-diffracting object. To do so, let us first imagine an arbitrary source with a radiation diagram described by unspecified functions $E_\theta(r, \theta, \phi)$ and $E_\phi(r, \theta, \phi)$ and make a single assumption that both E_θ and E_ϕ are zero at an angular position (θ_0, ϕ_0). We will address the suitability of this assumption (manifesting as a question of how stable the zero is) in a later section of this chapter.

4.2.1 Transverse and radial intensity

Due to their characteristic r-dependencies, the ratio of the transverse and radial intensities itself acquires a radial dependence, which we see using Eq. (4.1) and Eq. (4.4),

$$\frac{\mathbf{E}_\mathrm{t}^* \cdot \mathbf{E}_\mathrm{t}}{E_r^* E_r} = r^2 \frac{f_\theta^* f_\theta + f_\phi^* f_\phi}{f_r^* f_r} = r^2 F(\theta, \phi). \tag{4.5}$$

Normally the ratio $F(\theta, \phi)$ is very large while in the paraxial limit the transverse field overwhelms the radial field. But under small displacements from a paraxial dark spot's location (θ_0, ϕ_0) these components are of similar magnitude and, by equating the always-positive Eq. (4.5) to a relatively small constant δ (e.g., $\delta = 1$) we define a tube-like *surface* S,

$$S : \; r^2 F(\theta, \phi) = \delta, \tag{4.6}$$

which has a real-space cross section C containing (θ_0, ϕ_0). Notice under the definition Eq. (4.6) that if the solid angle Ω enclosed by $C_{\theta\phi}$, the surface's (θ, ϕ)-space cross section at some radial distance, scales linearly with the value of δ, then $C_{\theta\phi}$ must shrink in (θ, ϕ) space around the paraxial dark spot's position with increasing r, at *exactly the same rate* as the real-space area of a spherical wavefront grows (the coverage of (θ, ϕ) space of the sphere is constant at 4π steradians). Swept through real space, the physical cross section C defines a non-diffracting tube enclosing the dark spot whose cross section is constant, completely independent of radial distance. The criterion that "the solid angle enclosed by $C_{\theta\phi}$ scales linearly with the value of δ" is not insignificant, but is easily met if the curve $C_{\theta\phi}$ is an ellipse, as turns out to be the case in a paraxial zero's immediate vicinity where field components behave like linear functions of space.

In this neighbourhood we can perform a lowest-order expansion of the electric field for a simple picture of how it behaves. Only the transverse field components are actually zero and so, defining the 2D transverse Jacobian matrix and the constant

(zeroth-order) complex radial term E_{r0}, we have,

$$\mathbf{E} = \mathbf{E}_{\mathrm{t}} + E_r\hat{\mathbf{r}} \approx \mathbf{J}\mathbf{v} + E_{r0}\hat{\mathbf{r}} = \begin{pmatrix} \frac{\partial E_\theta}{\partial \theta} & \frac{\partial E_\theta}{\partial \phi} \\ \frac{\partial E_\phi}{\partial \theta} & \frac{\partial E_\phi}{\partial \phi} \end{pmatrix} \begin{pmatrix} \theta' \\ \phi' \end{pmatrix} + E_{r0}\hat{\mathbf{r}}, \tag{4.7}$$

where $\mathbf{v} = \theta'\hat{\boldsymbol{\theta}} + \phi'\hat{\boldsymbol{\phi}}$ and $\theta' = \theta - \theta_0$ and $\phi' = \phi - \phi_0$ are angular displacements from the dark spot centre. Importantly under the first order approximation, the electric field intensity becomes a quadratic function of θ' and ϕ' as well as $\mathbf{E}$. Likewise $F(\theta, \phi)$ from Eq. (4.5) behaves quadratically in (θ, ϕ) space such that the closed curve $r^2F(\theta, \phi) = \delta$ cuts an ellipse shape through the (θ, ϕ) plane. Our linear approximation Eq. (4.7) of the electric field is accurate in the far field limit where, due to there being a well-defined longitudinal propagation direction, the field components vary slowly across the transverse plane. With sufficient distance (e.g., for $r > 3\lambda$) the influence of higher-order derivatives on the small non-paraxial region surrounding the dark spot is negligible and the shape and size of the non-diffracting tube (and as we shall see, C lines) are very well-described by a first-order Taylor expansion of the field. We will proceed with Eq. (4.7) in the following sections. Nearer to the source, on the border of the far field region (around $r = 2\lambda$, a minimum distance for which it is reasonable to discuss *paraxial* dark spots), higher-order transverse derivatives of the field components are more significant and (combined with the assumption of spherical wavefronts) deform our tube's expected elliptical cross section.

Summarising this section, we demonstrated that in the far field of an arbitrary source containing a dark spot, the setting of the ratio of the transverse and radial component intensities to a constant δ yields an equation of the form $r^2F(\theta, \phi) = \delta$, which in the region of the paraxial dark spot is quadratic with respect to (θ, ϕ) and thus defines a tube with elliptical cross section. The r^2 dependence of the left hand

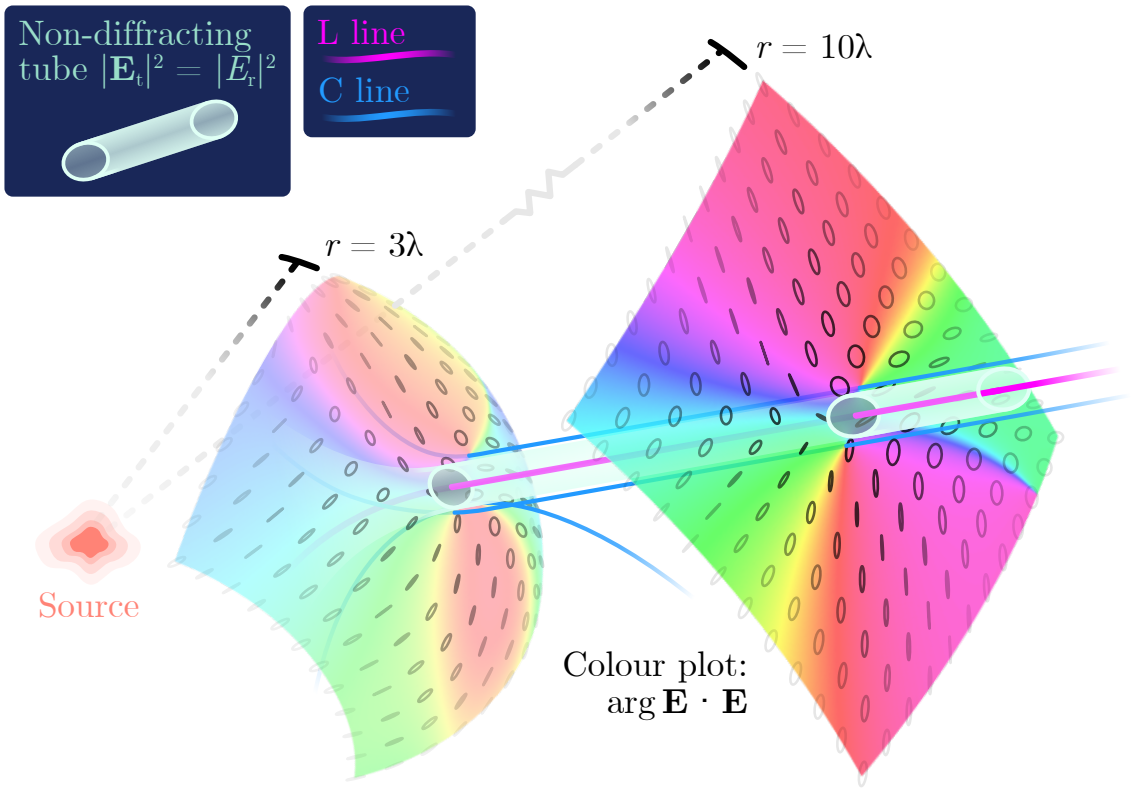

Figure 4.2: A paraxial dark spot where $\mathbf{E}_t = \mathbf{0}$, equivalent to a radially polarised L line (magenta line) extending infinitely from a source, along with a tube defined where $|\mathbf{E}_t|^2 = |E_r|^2$ that does not change in cross section. The dark spot and tube pass through two sphere patches on which the phase angle $\arg \mathbf{E} \cdot \mathbf{E}$ and nearby polarisation ellipses (normalised amplitude) are plotted, the spheres defined at radii $r = 3\lambda$ and $r = 10\lambda$ and centred on the source. Two non-diverging true C lines (blue) accompany the dark spot into the far field.

side of this equation compensates for the $4\pi r^2$ surface area of each far field wavefront, getting larger with radial distance from the source, and means the intensity-ratio tube is immune to the diffractive effects that light's energy density is subject to—though because the tube exists in, by definition, a low-intensity region of space, the visibility and applicability of the tube is perhaps limited, as we shall return to discuss at the end of this chapter. Figure 4.2 depicts one such non-diffracting tube enclosing a paraxial dark spot (the magenta radially polarised L line). The tube pierces patches

of two spherical surfaces of radius $r = 3\lambda$ and $r = 10\lambda$ without spreading out in cross section. Other elements present in Fig. 4.2 are discussed later on.

4.2.2 Tube cross section

We can use the tube defined by Eq. (4.6) in a first-order approximation to better understand the geometry of its elliptical cross section. Calculating Eq. (4.5) with $\mathbf{E}_\mathrm{t} = \mathbf{J}\mathbf{v}$ and a radial component evaluated at the paraxial zero centre, $E_r(r, \theta_0, \phi_0) = E_{r0} = f_{r0}\exp(ikr)/r^2$, we may obtain the tube,

$$r^2 F(\theta, \phi) = r^2 \frac{1}{f_{r0}^* f_{r0}} \mathbf{v}^T \left[\mathbf{J}_f^{*T} \mathbf{J}_f\right] \mathbf{v} = \delta, \tag{4.8}$$

where,

$$\mathbf{J}_f = \begin{pmatrix} \frac{\partial f_\theta}{\partial \theta} & \frac{\partial f_\theta}{\partial \phi} \\ \frac{\partial f_\phi}{\partial \theta} & \frac{\partial f_\phi}{\partial \phi} \end{pmatrix}. \tag{4.9}$$

Writing $\mathbf{v}^T \left[\mathbf{J}_f^{*T} \mathbf{J}_f\right] \mathbf{v}$ compacts the tube cross section's quadratic form into a matrix expression, wherein the eigenvalues λ_1, λ_2 of the 2×2 matrix $\mathbf{J}_f^{*T} \mathbf{J}_f$ relate to the semi-axis lengths a' and b' of the tube's elliptical cross section in (θ, ϕ) space:

$$\begin{aligned} a' &= \frac{\sqrt{\delta}}{r} \sqrt{\frac{f_{r0}^* f_{r0}}{\lambda_1}}, \\ b' &= \frac{\sqrt{\delta}}{r} \sqrt{\frac{f_{r0}^* f_{r0}}{\lambda_2}}. \end{aligned} \tag{4.10}$$

Assuming a small elliptical cross section, the enclosed solid angle is $\Omega = \sin\theta \pi a' b'$ and is thus proportional to δ, giving a real-space enclosed area A of,

$$A = r^2 \Omega = \pi \delta \sin\theta \frac{f_{r0}^* f_{r0}}{\sqrt{\lambda_1 \lambda_2}} = \pi \delta \sin\theta \frac{f_{r0}^* f_{r0}}{|\det \mathbf{J}_f|}, \tag{4.11}$$

where we have used $\sqrt{\lambda_1\lambda_2} = \sqrt{\det \mathbf{J}_f^{*T}\mathbf{J}_f} = \sqrt{\det \mathbf{J}_f^{*T} \det \mathbf{J}_f} = |\det \mathbf{J}_f|$. Equation (4.11) provides a general expression for the cross-sectional area of the non-diffracting tube surrounding a far field dark spot in an otherwise arbitrary field radiated by an unknown source. It shows clearly in the final equality that the area A is independent of r and hence does not diffract with distance from the source. While the chosen constant δ comparing the radial and transverse field intensity scales the size of the tube cross section, the core elliptical geometry is determined by the field derivatives which construct the transverse Jacobian $\mathbf{J}$ (and subsequently $\mathbf{J}_f$). Two 'generic' paraxial zeros are unlikely to share the same Jacobian and can construct non-diffracting tubes with drastically different ellipticity and extent for the same value of δ, though ordinarily, the semi axes of the tube cross section are on the order of a reasonable fraction of a wavelength. As in the non-generic, axially symmetric cases of a vortex beam [115] and, as we next demonstrate, a linearly polarised dipole (both of which contain 2D zeros), a non-diffracting cylindrical tube exists with a diameter of $2\sqrt{\delta}\lambda/\pi$.

4.2.3 Example: a linearly polarised dipole

We shall now apply the equation of the cross-sectional area of the non-diffracting intensity ratio tube that exists around the dark axis of a linearly polarised dipole, which we know to have a radiation diagram given simply by $E_\theta = f_\theta \exp(ikr)/r = E_0 \sin\theta \exp(ikr)/r$ and $E_\phi = 0$ where E_0 is a complex amplitude (Fig. 4.1). Incidentally, these expressions prove to be problematic when substituted into Eq. (4.11) because the dipole's zeros lie at $\theta = 0, \pi$ where the azimuth angle ϕ is not defined and the field Jacobian is singular. In remedying this we may rotate the dipole by $\pi/2$ radians such that its axial zero passes through $(\theta, \phi) = (\pi/2, 0)$ and $(\theta, \phi) = (\pi/2, \pi)$,

giving the following transverse components,

$$E_\theta = E_0 \cos\theta \cos\phi \frac{\mathrm{e}^{ikr}}{r}, \qquad E_\phi = -E_0 \sin\theta \frac{\mathrm{e}^{ikr}}{r}. \tag{4.12}$$

Meanwhile, the r-independent Jacobian $\mathbf{J}_f$ [Eq. (4.9)] of the transverse field and the modulus of its determinant are,

$$\mathbf{J}_f = \begin{pmatrix} -E_0 \sin\theta\cos\phi & -E_0\cos\theta\sin\phi \\ 0 & -E_0\cos\phi \end{pmatrix}, \tag{4.13}$$

$$|\det \mathbf{J}_f| = \sqrt{E_0^* E_0^* E_0 E_0}\sin\theta\cos^2\phi = E_0^* E_0 \sin\theta\cos^2\phi. \tag{4.14}$$

To find the radial field component we calculate Eq. (4.2) (neglecting the constant term), giving,

$$E_r = E_0 \frac{i}{k}\left(-\sin\theta\cos\phi + \frac{\cos\theta\cos\phi}{\tan\theta} - \frac{\cos\phi}{\sin\theta}\right)\frac{\mathrm{e}^{ikr}}{r^2}, \tag{4.15}$$

which evaluates at the zero location $(\theta_0, \phi_0) = (\pi/2, 0)$ to $E_{r0}(r, \theta_0, \phi_0) = -2E_0 i/k \cdot \exp(ikr)/r^2$. Finally, substituting Eq. (4.14) and $f_{r0} = -2E_0 i/k$ into Eq. (4.11), we have at the zero location $(\theta_0, \phi_0) = (\pi/2, 0)$ a tube area of,

$$A = \pi\delta\sin\theta_0 \frac{4E_0^* E_0}{k^2 E_0^* E_0 \sin\theta_0 \cos^2\phi_0} = \frac{4\pi\delta}{k^2} = \delta\frac{\lambda^2}{\pi}, \tag{4.16}$$

which leads to a non-diffracting tube diameter of $2\sqrt{\delta}\lambda/\pi$.

The authors of [116] identified a constant-cross-section tube of circular polarisation enclosing the linearly polarised dipole's axis, in agreement with this subsection's

brief treatment (despite the fact that we have not yet considered polarisation). In fact with almost identical arguments to those we have so far used it is possible to show that an even number of parallel lines of true circular polarisation are produced automatically by paraxial zeros. The axial symmetry of the linearly polarised dipole makes a degenerate case in which a surface of circular polarisation coincides exactly with our non-diffracting intensity ratio tube.

4.2.4 True C lines

Having an overall propagation direction the phase structure of the paraxial field is such that on the sphere of radius r or a local transverse plane, the entire polarisation texture of the transverse field $\mathbf{E}_\mathrm{t}$ extends uniformly in the radial direction as special points of polarisation are drawn into lines and lines drawn into surfaces. But as we discussed, a 2D zero where $\mathbf{E}_\mathrm{t} = \mathbf{0}$ sets up a well of non-paraxial polarisation which, before transitioning to the typical polarisation texture of a paraxial field as one moves away from the dark spot, contains *true* circular and linear polarisation singularities in the 3D field vector $\mathbf{E} = \mathbf{E}_\mathrm{t} + E_r\hat{\mathbf{r}}$, not simply in the transverse field projection.

To find the lines of true circular polarisation in a paraxial dark spot's neighbourhood, we first calculate $\mathbf{E}\cdot\mathbf{E}$ under the first-order approximation Eq. (4.7),

$$\mathbf{E}\cdot\mathbf{E} \approx (\mathbf{J}\mathbf{v})\cdot(\mathbf{J}\mathbf{v}) + E_{r0}\cdot E_{r0} = \mathbf{v}^T\left[\mathbf{J}^T\mathbf{J}\right]\mathbf{v} + E_{r0}\cdot E_{r0}. \tag{4.17}$$

We know from chapter 3 that the electric field is circularly polarised when $\mathbf{E}\cdot\mathbf{E} = 0$ allowing us to arrive at the complex quadratic equation,

$$\mathbf{v}^T\left[\mathbf{J}^T\mathbf{J}\right]\mathbf{v} = \mathbf{E}_\mathrm{t}\cdot\mathbf{E}_\mathrm{t} = -E_{r0}\cdot E_{r0}, \tag{4.18}$$

whose solutions $\mathbf{v}_\mathrm{c}$ locate circular polarisation. Note that the condition Eq. (4.18) departs from Eq. (4.8) for $\delta = 1$ by having both the 2×2 matrix $\mathbf{J}^T\mathbf{J}$ and $E_{r0} \cdot E_{r0}$ being complex-valued. This means that the real and imaginary parts of $\mathbf{v}^T \left[\mathbf{J}^T\mathbf{J}\right] \mathbf{v} + E_{r0} \cdot E_{r0} = 0$ each define quadratic surfaces M and N, constant in the radial direction, whose cross sections are either elliptical or parabolic (since $\mathbf{v}^T\Re\{\mathbf{J}^T\mathbf{J}\}\mathbf{v}$ and $\mathbf{v}^T\Im\{\mathbf{J}^T\mathbf{J}\}\mathbf{v}$ need not be positive for all $\mathbf{v}$). Regardless of the cross section geometry of the real and imaginary parts of Eq. (4.18), be they ellipses or parabolas or a combination of the two, we may still define principle axes for each in (θ, ϕ) space similar to Eq. (4.10) and which in real space have r-independent arc lengths. Then, the positions of the intersections of $M : \mathbf{v}^T\Re\{\mathbf{J}^T\mathbf{J}\}\mathbf{v} = \Re\{-E_{r0} \cdot E_{r0}\}$ and $N : \mathbf{v}^T\Im\{\mathbf{J}^T\mathbf{J}\}\mathbf{v} = \Im\{-E_{r0} \cdot E_{r0}\}$ corresponding to true circular polarisation do not diverge from the paraxial dark spot, and like the intensity ratio tube defined in section 4.2.1, can be described as non-diffracting. Figure 4.3 illustrates how the surfaces M and N might emerge as either a hyperbola, a degenerate hyperbola, or an ellipse on the transverse plane, and intersect with one another in an even number of places near to a paraxial zero where true 3D circular polarisation is located.

As a paraxial dark spot propagates further and further into the far field, the region for which a first-order approximation of the field components is accurate grows and envelopes the dark spot's neighbourhood and its non-diffracting structures (which, of course, do not grow in size). Therefore in real space near to the zero $\mathbf{E}_\mathrm{t} \cdot \mathbf{E}_\mathrm{t}$ is almost a perfectly quadratic function of space which, due to its in-built symmetries, satisfies $\mathbf{E}_\mathrm{t} \cdot \mathbf{E}_\mathrm{t} = -E_{r0} \cdot E_{r0}$ in an even number of locations in the transverse plane. We have proven in this way that an even number (0 inclusive) of true C lines generically accompany a paraxial dark spot into the far field without diverging, maintaining constant separation (this feature is also shown in Fig. 4.2).

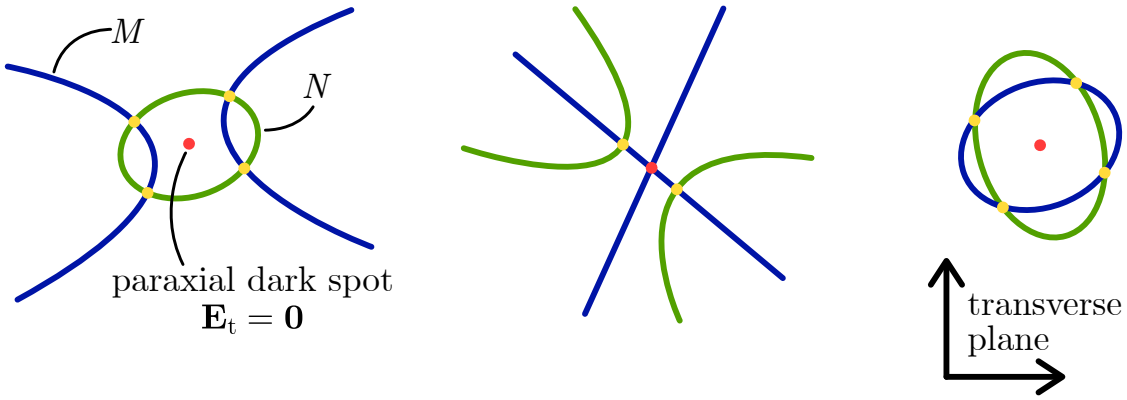

Figure 4.3: Non-exhaustive examples of paraxial zeros and the curves $M : \Re\{\mathbf{E}_\mathrm{t} \cdot \mathbf{E}_\mathrm{t}\} = \Re\{-E_{r0} \cdot E_{r0}\}$ (blue) and $N : \Im\{\mathbf{E}_\mathrm{t} \cdot \mathbf{E}_\mathrm{t}\} = \Im\{-E_{r0} \cdot E_{r0}\}$ (green) as viewed on the transverse plane near to a dark spot (red circle), their intersections highlighted by the yellow circles.

4.2.5 Example: Young's double slit experiment

We have learned that transverse field zeros, paraxial dark spots, always construct non-diffracting structures that can be defined by comparing the intensity of the transverse and radial field components[†] What better way to support our claims than by revisiting an over-200-years-old experiment?

When in 1801 Thomas Young shone sunlight through two thin slits separated by an opaque surface he observed the interference fringes indicative of light's wave-like nature, periodically spaced bright lines (maxima) of constructive interference and

[†]That the transverse and radial field components reduce by $1/r$ and $1/r^2$ is a general feature of a paraxial field, not in any way restricted to a region around a dark spot, so it is natural to ask whether non-diffracting structures can only be identified near zeros. The special feature of the dark spot is that transverse intensity increases in every outward direction, *while* the field components behave as linear functions of θ, ϕ nearby—so taking the intensity ratio of $\mathbf{E}_\mathrm{t}$ and E_r results in *closed* tubes. It is not generally possible to identify small closed tubes that do not diffract using the intensity ratio elsewhere in the field (although closed tubes could be defined around local maxima, they would likely not be diffraction-immune as maxima are non-zero stationary points of the field components, meaning $\nabla_\mathrm{t}\mathbf{E}_\mathrm{t} = \mathbf{0}$). But in principle, one *could* identify non-diffracting structures—which could be closed tubes, or parallel surfaces with constant separation—that are not associated with zeros in intensity $\mathbf{E}_\mathrm{t}^* \cdot \mathbf{E}_\mathrm{t}$, but with zeros in other quadratic scalar fields (e.g. $|\mathbf{E}_\mathrm{t} \cdot \mathbf{E}_\mathrm{t}|$ or $|\mathbf{E}_\mathrm{t}^* \cdot \mathbf{H}_\mathrm{t}|$) that are found in non-dark regions of the paraxial field.

the dark minima of destructive interference in-between, as well as dispersive effects [1]. The interference fringes were projected onto a screen well into the far field of the light appearing to radiate from the two slits. Sunlight is, of course, unpolarised though should we replace Young's source with a single-frequency radiator, we may obtain a monochromatic interference pattern whose well-defined polarisation can be probed near to the interference minima that are, as the reader might have guessed, paraxial dark spots. Suppose that we illuminate an opaque screen split by two thin slits parallel to the z axis, separated along the x axis by a distance d, with a plane wave propagating normal to the screen along y and linearly polarised in the $\hat{\mathbf{x}}$ direction, perpendicular to the length of the slits. The plane wave is diffracted by the two slits which approximately behave like sources of cylindrical waves, in phase and with the same amplitude A_p, that must carry both $\hat{\mathbf{x}}$ and $\hat{\mathbf{y}}$ field components to obey the transversality condition; slit 1 radiates the field $\mathbf{E}_1$ and slit 2 the field $\mathbf{E}_2$. The cylindrical fields are given by,

$$\mathbf{E}_1 = \begin{pmatrix} A_p \sin\alpha_1 \\ -A_p \cos\alpha_1 \\ 0 \end{pmatrix} \frac{\mathrm{e}^{ik\rho_1}}{\sqrt{\rho_1}}, \tag{4.19}$$

$$\mathbf{E}_2 = \begin{pmatrix} A_p \sin\alpha_2 \\ -A_p \cos\alpha_2 \\ 0 \end{pmatrix} \frac{\mathrm{e}^{ik\rho_2}}{\sqrt{\rho_2}}, \tag{4.20}$$

where $\rho_{1,2} = |\mathbf{r} - \mathbf{r}_{1,2}|$, $\mathbf{r}_{1,2} = \pm(d/2)\hat{\mathbf{x}}$ being the slits' position vectors. Two cylindrical waves and the relevant parameters in Eq. (4.19) and Eq. (4.20) are drawn in Fig. 4.4(a) for a slit separation of $d = 3\lambda$, while in Fig. 4.4(b) we plot the electric energy density $W_\mathrm{e} \propto \mathbf{E}^* \cdot \mathbf{E}$ in the resulting interference (the colour is saturated at 1

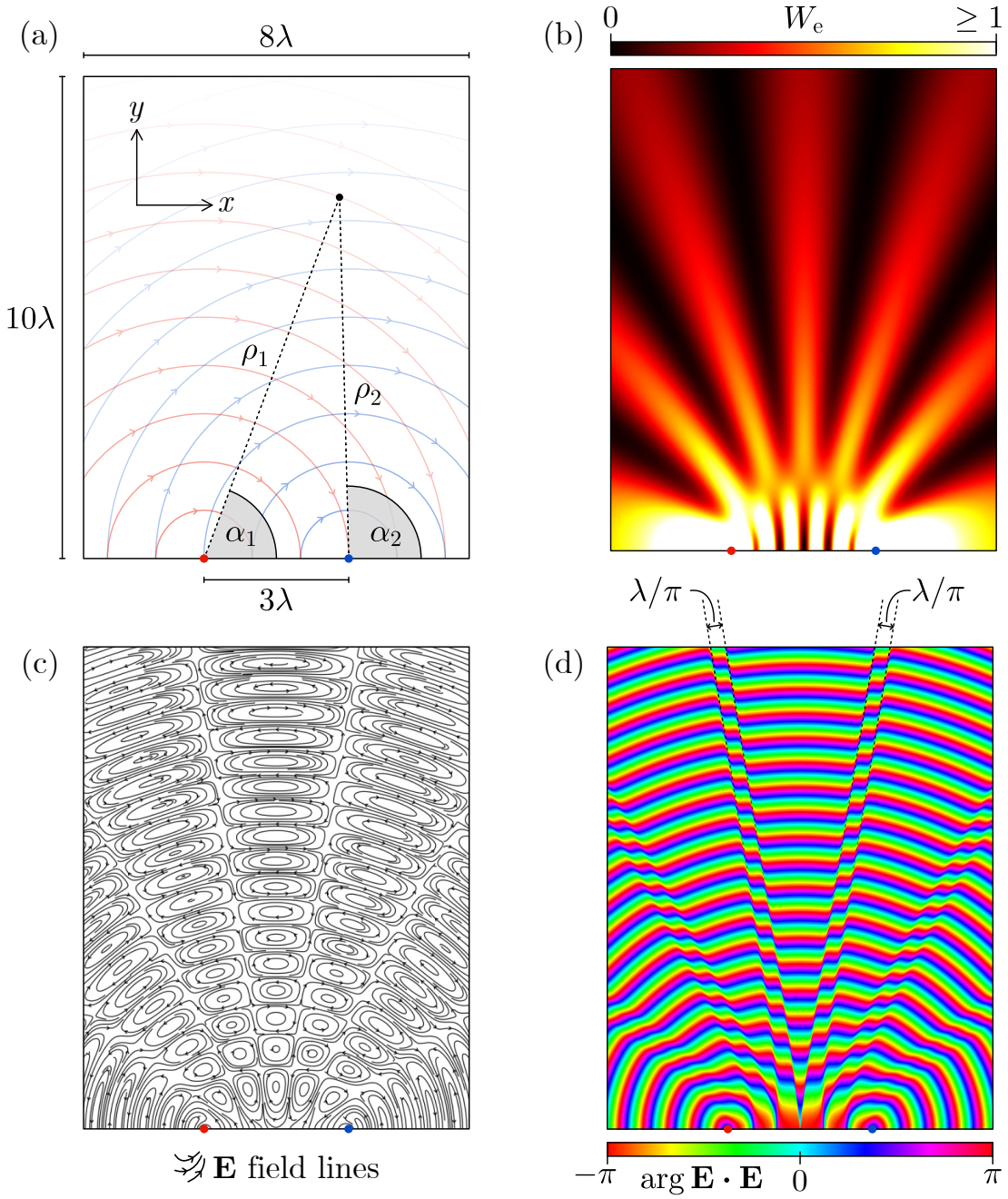

Figure 4.4: Non-diffracting structures in a monochromatic version of Young's double slit experiment where an $\hat{\mathbf{x}}$ polarised plane wave illuminates the slits. The slits are approximated by two cylindrical waves with $\hat{\mathbf{x}}$ and $\hat{\mathbf{y}}$ components separated as shown in (a) by 3λ. In (b) the electric energy density in the two waves' superposition $\mathbf{E}$ is plotted with a saturated colourmap while in (c) the field lines are plotted. In (d) the phase angle of $\mathbf{E} \cdot \mathbf{E}$, whose dislocation lines correspond to circular polarisation, revealing non-diverging lines of circular polarisation separated by λ/π.

a.u.—the maximum energy density a short distance from $y = 0$—since the cylindrical waves become singular at $\rho_{1,2} = 0$). While individually these fields with cylindrical wavefronts have no longitudinal components in the direction of $\rho_{1,2}$, their superposition $\mathbf{E} = \mathbf{E}_1 + \mathbf{E}_2$ falls onto a screen whose face is perpendicular to $\hat{\mathbf{y}}$ and, separated a few wavelengths from the slits along the y axis, in the centre of the screen the $\hat{\mathbf{x}}$ component of $\mathbf{E}$ is dominant and the $\hat{\mathbf{y}}$ component, longitudinal to the screen, is insignificant by comparison—except in the interference minima. One in fact sees the dominance of longitudinal field components in the field line plot of the interference pattern [Fig. 4.4(c)]—since, according to Gauss' law in free space $\nabla \cdot \mathbf{E} = 0$, field lines must be closed in each interference minima they run approximately parallel to $\hat{\boldsymbol{\rho}}$ and to $\hat{\mathbf{y}}$ near to $x = 0$ (it is, of course, the way that electric field lines must comply with $\nabla \cdot \mathbf{E} = 0$ in transverse field minima that results in Eq. (4.4) and all of our reported non-diffracting features). As long as the amplitudes of the two waves are similar (i.e., $\rho_1 \approx \rho_2$) then the electric field $\hat{\mathbf{x}}$ component is approximately zero in a minimum and non-diffracting structures arise in the relationship between the longitudinal and transverse fields (the ratio of the magnitude of the transverse and longitudinal components equals 1 when the field lines in Fig. 4.4(c) are about 45° relative to the axis of a dark fringe). Non-diverging C lines (C planes in 3D) with a constant λ/π separation are observed sandwiching the two most central interference minima as shown by the dislocation lines in the plot of $\arg \mathbf{E} \cdot \mathbf{E}$ in Fig. 4.4(d). These C lines which rely on there being both $\hat{\mathbf{x}}$ and $\hat{\mathbf{y}}$ field components present in the wave superposition would not be present were the slits vertically polarised (i.e., $A_p = 0$ and the $\hat{\mathbf{z}}$ components in Eq. (4.19) and Eq. (4.20) are non-zero); this would result in scalar interference but with non-diverging C lines present in the magnetic field.

4.3 Time-fixed and instantaneous zeros: the question of stability

Insofar as we have described far fields using the complex field phasors $\mathbf{E}$ and $\mathbf{H}$, *time-fixed* paraxial dark spots are unstable entities. A zero in the two-component transverse field phasor $\mathbf{E}_{\mathrm{t}} = \mathbf{0}$ actually imposes four scalar conditions, $\Re\{E_\theta\} = 0$ and $\Im\{E_\theta\} = 0$ and $\Re\{E_\phi\} = 0$ and $\Im\{E_\phi\} = 0$; one condition too many to coalesce naturally within the span of three spatial dimensions. We cannot expect a chance encounter with a fixed-position paraxial dark spot in arbitrary far field radiation but it is possible to create one synthetically, for example in a vector vortex beam or by designing a source's radiation diagram, a topic which we discuss in-depth in chapter 6 (dipolar and multipolar sources can also 'radiate' paraxial dark spots but these are no less unstable).

If perturbed by noise, a paraxial zero is destroyed which presents a challenge for practical application of the zero's non-diffracting polarisation properties. However, it is possible to reconstruct destroyed dark spots by allowing a parameter of the far field source to vary and pose as an artificial dimension, a technique proposed by the authors of [117] who demonstrated that a point-like zero could be recovered after perturbation by re-tuning the source wavelength. Paraxial zeros exist stably in a four-dimensional parameter space such as (x, y, z, λ). When destroyed in real space at a given wavelength by noise, the dark spot is displaced in (x, y, z, λ) space and may still be accessed at a new (x, y, z, λ) co-ordinate by re-tuning λ (of course, λ is not the only possible changeable parameter!).

Although far field zeros in the transverse field phasor ($\mathbf{E}_{\mathrm{t}} = \mathbf{0}$, zeros whose positions do not change over time) are not topologically protected singularities

like paraxial C points or L lines, *instantaneous* paraxial zeros *are*. An instantaneous paraxial zero occurs when the time-dependent, transverse electric field vector $\boldsymbol{\mathcal{E}}_{\mathrm{t}} = \Re\{\mathbf{E}_{\mathrm{t}} \exp(-i\omega t)\}$ crosses zero, something which is only possible at positions where the electric field is linearly polarised in the transverse plane. Existing only momentarily in one position, instantaneous zeros travel smoothly and periodically along continuous trajectories defined by paraxial L lines (lines of linear polarisation), racing rapidly around the source's far field radiation diagram. And at any given instant in time, the conditions $\boldsymbol{\mathcal{E}}_{\mathrm{t}} = \mathbf{0}$ are guaranteed to be met in at least one location somewhere in the far field region of any source. It is straightforward to explain why using fundamental topological arguments, namely the hairy ball theorem, which in this context states that $\boldsymbol{\mathcal{E}}_{\mathrm{t}}$, being a two-component real vector, cannot lie tangent to (or be 'combed' over) each far field spherical wavefront without incurring at least one singularity where its direction is undefined—a zero.

We must not forget the presence of the small but non-zero time-varying radial field component $\mathcal{E}_r$ which still obeys the $1/r^2$ dependence of Eq. (4.4). While there is not enough information contained in a momentary snapshot of the electric field vector to understand its polarisation structure, we can still compare the square lengths of the transverse and radial field components, $|\boldsymbol{\mathcal{E}}_{\mathrm{t}}|^2$ and $\mathcal{E}_r^2$, near to an instantaneous dark spot and obtain a non-diffracting ratio, simply by first introducing time dependence to our first-order approximation Eq. (4.7) and taking the real part at an instant $t = t_0$,

$$\boldsymbol{\mathcal{E}}(\mathbf{v}, t_0) \approx \boldsymbol{\mathcal{J}}(t_0)\mathbf{v} + \mathcal{E}_{r0}(t_0)\hat{\mathbf{r}}, \tag{4.21}$$

where,

$$\begin{aligned} \boldsymbol{\mathcal{J}}(t_0) &= \frac{1}{r}\boldsymbol{\mathcal{J}}_f(t_0) = \Re\left\{\mathbf{J}\mathrm{e}^{-i\omega t_0}\right\}, \\ \mathcal{E}_{r0}(t_0) &= \frac{1}{r^2} f_{r0}(t_0) = \Re\{E_{r0}\mathrm{e}^{-i\omega t_0}\}, \end{aligned} \tag{4.22}$$

and once again $\mathbf{v} = (\theta', \phi')$. Equating the approximated transverse and radial fields at the instant t_0 via a constant δ, we may define a time-varying square-length-ratio tube (the time-dependent version of Eq. (4.6) using the first-order approximation):

$$r^2 \frac{\mathbf{v}^T \boldsymbol{\mathcal{J}}_f^T(t_0) \boldsymbol{\mathcal{J}}_f(t_0) \mathbf{v}}{f_{r0}(t_0)} = \delta. \tag{4.23}$$

The fact that Eq. (4.23) is written using time-varying quantities does not change the fundamental relation between the transverse and radial field components—that they have $1/r$ and $1/r^2$ respective radial dependencies—and so the tube Eq. (4.23) is likewise non-diffracting, but no longer does it have a time-fixed position in angular space. As time evolves and the instantaneous dark spot travels along its L line path it is followed by the non-diffracting tube Eq. (4.23).

It is quite true that a changing position renders the time-dependent non-diffracting tube unlikely to be of much practical value. But what we may conclude from this discussion is that non-diffracting structures can be identified in some form in all far field radiation and are, in this sense, a fundamental electromagnetic phenomenon, a mandatory consequence of Maxwell's equations that emerge at any given instant even in unpolarised light.

4.4 Chapter summary

Paraxial electric dark spots are unstable points on the transverse plane of far field radiation where the transverse components of the electric field phasor are zero, $\mathbf{E}_{\mathrm{t}}(\mathbf{r}_{\mathrm{z}}) = \mathbf{0}$, and that defy the expected behaviour of the paraxial regime. As the transverse field approaches zero in the neighbourhood of $\mathbf{r}_{\mathrm{z}}$ its amplitude becomes comparable to the radial field components, ordinarily neglected but ever present in

far fields, establishing a region of non-paraxial, 3D polarisation (though intensity is very low). Because of their inherent instability time-fixed dark spots in the electric field phasor do not occur naturally and must be created synthetically or identified in particularly symmetric fields, such as from a radiating dipole. Here in the first of four chapters of original results we showed that by comparing transverse and radial field intensities that have different radial dependencies any paraxial dark spot develops non-diverging structures such as an even number of parallel C lines and a tube of constant ratio between $|\mathbf{E}_\mathrm{t}|^2$ and $|E_r|^2$.

Conceptually a non-diffracting property of a field, be it an intensity-ratio tube or non-diverging C lines, could be invaluable in metrology or any discipline which involves alignment of directive beams. But to measure in the far field what is unstable to noise and can only occur in regions of low intensity due to the dominance of longitudinal field components will inevitably be challenging, requiring high-sensitivity detectors. In the RF-microwave regime, by modulating the elements of a phased array antenna a paraxial dark spot could be created and accompanied by non-diffracting features of a substantial size ($\sim \lambda/\pi$), that could be measured in principle using high gain antennas (which can be rotated in 3D to measure field components). Nonetheless, from a purely theoretical perspective we have shown that non-diffracting features, be they time-varying or time-fixed, are remarkably general occurrences in paraxial light because of the fundamental difference in radial dependence of the amplitude of the transverse and longitudinal field components.

Chapter 5

Non-paraxial dark spots

Before settling into the spherical uniformity of the far field region a wavefront, emitted from a localised source, navigates the much more turbulent near field region where the electromagnetic field bends many of the rules and breaks many of the symmetries held under the paraxial limit. Complicated swirling electric and magnetic momentum currents and totally inhomogeneous, 3D polarisation occur in the *non-paraxial* near field region as energy density is divided unevenly between the electric and magnetic fields and their non-zero parallel and antiparallel components [37]. The fact that **E** and **H** polarisation ellipses may be different in shape and amplitude and not all constrained to the same plane means that non-paraxial electric dark spots $\mathbf{E} = \mathbf{0}$, where all three electric field components are zero, are usually point-like singularities which are synthesised in a non-zero magnetic field. A point-like character makes the non-paraxial dark spot an interesting prospect for use in dark spot microscopy [29, 30, 118, 119] and optical trapping and imbue the electromagnetic field with rich topological properties which we will study in depth in this chapter, reporting the findings of our publication *3D zeros in electromagnetic fields* [20].

There is also a pure theoretical interest in point-like field zeros, in that besides what we present here, there is no framework to classify the types of zero that can occur in the same way as topological indices exist for phase and polarisation singularities. So many electromagnetic quantities are defined using the electric field phasor that a three-component zero is not one but a whole intricate assortment of vector singularities. Most are point-like singularities as described in section 3.6 but $\mathbf{E} = \mathbf{0}$ also meets both the mathematical criteria of circular polarisation ($\mathbf{E} \cdot \mathbf{E} = 0$) and linear polarisation $\Im\{\mathbf{E}^* \times \mathbf{E}\} = \mathbf{0}$, thereby acting as a meeting point for polarisation singularities which, as we will learn, intersect in a discrete number of combinations. Together these vector singularities give rise to very many possible incarnations of a point-like dark spot, in contrast to simpler singularities (for example first-order phase singularities, which have a topological charge magnitude of 1, are differentiated by being either left or right handed; paraxial $|1/2|$-index C points create three possible polarisation ellipse patterns).

More specifically we treat first-order electric field dark spots in this chapter, as in the previous chapter of this thesis (though this time they are point-like, rather than line structures in the far field). This is a dark spot whose first-order spatial derivatives are non-zero meaning no more conditions are enforced beyond those, totalling six, suppressing the three complex electric field components. Though they are no more difficult to create theoretically a higher-order zero does require more degrees of freedom which may not be available in an experimental scenario, meanwhile the dark spot need only be first-order to act as a 3D optical trap or a microscopy tool. Unlike paraxial dark spots, $\mathbf{E}$ in a non-paraxial field can be zero independently ('independently' insofar as Maxwell's equations allow) from the magnetic field, which needs to be suppressed separately to achieve a perfectly dual electromagnetic zero ($\mathbf{E} = \mathbf{H} = \mathbf{0}$), which would total twelve real scalar conditions.

In the following section where we establish how polarisation singularities interact with an electric field dark spot, our conclusions apply identically to a magnetic field zero and magnetic polarisation. It is true that an electric field dark spot may be transformed into a magnetic dark spot via a duality operation, which preserves dual-symmetric vector singularities (such as the Poynting vector) and switches the sign of singularities which break dual symmetry (such as the imaginary Poynting vector). Once more our primary tool for probing first-order non-paraxial dark spots is the field Jacobian matrix, now in three dimensions, though because we will be calculating Jacobian matrices for multiple vector fields we shall make some distinctions in notation. The electric and magnetic field Jacobian matrices are denoted $\mathbf{J}_{\mathrm{E}}$ and $\mathbf{J}_{\mathrm{H}}$ respectively, while to avoid untidy subscripts the Jacobian matrices of all other electromagnetic vectors will be referred to as first-order dyadics using $D(*)$, e.g., for a vector $\mathbf{F}$,

$$D(\mathbf{F}) = \begin{pmatrix} \frac{\partial F_x}{\partial x} & \frac{\partial F_x}{\partial y} & \frac{\partial F_x}{\partial z} \\ \frac{\partial F_y}{\partial x} & \frac{\partial F_y}{\partial y} & \frac{\partial F_y}{\partial z} \\ \frac{\partial F_z}{\partial x} & \frac{\partial F_z}{\partial y} & \frac{\partial F_z}{\partial z} \end{pmatrix}. \tag{5.1}$$

Given that point-like dark spots are not in 3D real space topologically protected we cannot expect to encounter them by chance; instead we must produce electric field zeros artificially. At the same time our electric field zeros, while created on purpose, should be as generic and unexceptional as possible, something which we can achieve with by randomising other aspects of the field. All figures in this chapter that depict polarisation and point-like vector singularities were produced in analytic simulations of the interference of ten monochromatic plane waves, which while intentionally polarised to enforce $\mathbf{E}(\mathbf{r}_{\mathrm{z}}) = \mathbf{0}$ at a position $\mathbf{r}_{\mathrm{z}}$, have randomly-assigned, 3D wavevectors (a similar approach to that which is used in other work identifying phase and polarisation singularities in wave fields [18]). There is no particular reason for

using ten plane waves—fewer or more than ten may be used to create non-paraxial dark spots—but the spatial complexity of the resulting field is increased the greater the number of interfering plane waves.

5.1 A dark spot's polarisation singularities

Suppose that a point-like, non-paraxial electric field dark spot exists at a position $\mathbf{r}_z$ such that $\mathbf{E}(\mathbf{r}_z) = \mathbf{0}$, the electric field magnitude increasing in all directions away from $\mathbf{r}_z$. The polarisation of the electric field is undefined at $\mathbf{r}_z$ but is determined nearby in a 3D first-order approximation of $\mathbf{E}(\mathbf{r})$ about $\mathbf{r} = \mathbf{r}_z$,

$$\mathbf{E} \approx \mathbf{J}_E \mathbf{v}, \tag{5.2}$$

where $\mathbf{v} = \mathbf{r} - \mathbf{r}_z$ is a 3×1 column vector and $\mathbf{J}_E$ is a 3×3 matrix. By equating $\mathbf{E} \cdot \mathbf{E} = 0$ and $(1/2)\Im\{\mathbf{E}^* \times \mathbf{E}\} = \mathbf{p} \times \mathbf{q} = \mathbf{0}$ under the approximation Eq. (5.2) we can locate any strands of circular and linear polarisation permeating the neighbourhood of $\mathbf{r}_z$. Although Eq. (5.2) is accurate only very near to the dark spot where first-order field derivatives dominate the Taylor expansion of $\mathbf{E}$, it sufficiently describes core polarisation structure imprinted by the dark spot. Since polarisation singularities are stable, thread-like structures, they cannot abruptly terminate and any which we identify passing through the dark spot using Eq. (5.2) will generally be preserved even at larger displacements from $\mathbf{r}_z$ where higher-order field derivatives take hold.

5.1.1 C lines

Approximating $\mathbf{E}\cdot\mathbf{E}$, we obtain a 3D version of Eq. (4.17) that can be split into real and imaginary parts in a vector-matrix-vector representation,

$$\mathbf{E}\cdot\mathbf{E} \approx \mathbf{v}^T\mathbf{M}\mathbf{v} + i\mathbf{v}^T\mathbf{N}\mathbf{v}. \tag{5.3}$$

in which $\mathbf{M} = \Re\{\mathbf{J}_{\mathrm{E}}^T\mathbf{J}_{\mathrm{E}}\}$ and $\mathbf{N} = \Im\{\mathbf{J}_{\mathrm{E}}^T\mathbf{J}_{\mathrm{E}}\}$. Both real and imaginary parts of Eq. (5.3) define quadric surfaces in 3D. The solution space of $\mathbf{v}^T\mathbf{M}\mathbf{v} + \mathbf{v}^T\mathbf{N}\mathbf{v} = 0$ is 1D, the line(s) of intersection of the two quadrics which are each usually double cones, vertices centred on $\mathbf{r}_{\mathrm{z}}$ because both $\mathbf{v}^T\mathbf{M}\mathbf{v} = 0$ and $\mathbf{v}^T\mathbf{N}\mathbf{v} = 0$ in the electric dark spot. Figure 5.1 shows that two double cones, one pair representing $\Re\{\mathbf{E}\cdot\mathbf{E}\} = 0$, the other $\Im\{\mathbf{E}\cdot\mathbf{E}\} = 0$, emerging from the same point $\mathbf{r}_{\mathrm{z}}$ have zero, two or four intersection lines that can be visualised on the unit sphere as points of intersection of ellipses (a cone has an elliptical cross section—note that in a first-order approximation, the solid angle enclosed by a cone does not change with radial distance from $\mathbf{r}_{\mathrm{z}}$). Two closed curves can intersect stably in an even number of locations and in particular two ellipses can intersect zero, two or four times proving, in terms of polarisation, that a point-like electric field dark spot must be crossed by zero, two or four C lines. Degenerate cases in the first-order approximation, where on the unit sphere in Fig 5.1 the ellipses may touch at a single point (giving an odd number of C lines), are not preserved in the exact scalar field $\mathbf{E}\cdot\mathbf{E}$, collapsing into an even number of intersections as higher-order derivatives take hold.

In truth the two quadrics are double cones only if $\mathbf{M}$ and $\mathbf{N}$ are not definite matrices meaning, for instance, that there are volumes of space where $\mathbf{v}^T\mathbf{M}\mathbf{v}$ is positive and negative, separated by the $\mathbf{v}^T\mathbf{M}\mathbf{v} = 0$ quadric. Otherwise, the real and imaginary parts of Eq. (5.3) can either solely increase or solely decrease in all

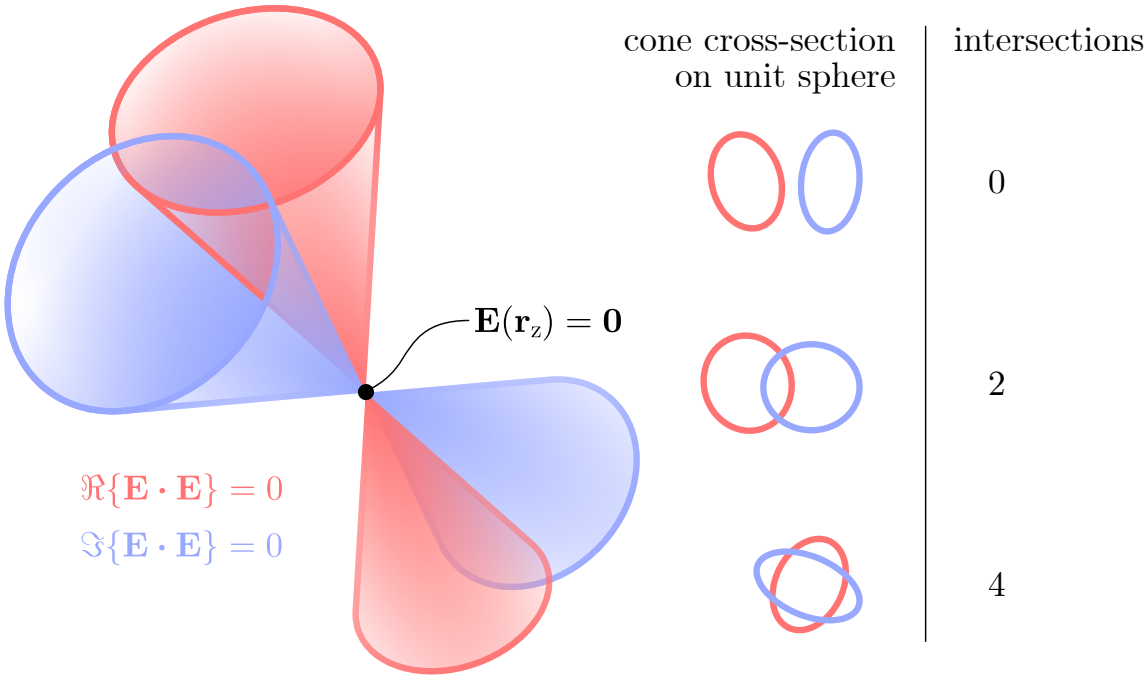

Figure 5.1: Quadric surfaces defined by the real (red) and imaginary (blue) parts of $\mathbf{E}\cdot\mathbf{E} = 0$ in a first-order approximation of $\mathbf{E}$ in the region of an electric field dark spot. The surfaces are generically double cones whose vertices touch at $\mathbf{r}_z$, the singularity's location, and either do not intersect, or intersect along two or four lines. On the unit sphere the cross section of each cone is elliptical. Two ellipses, if they intersect, cross at two or four points, which helps to visualise the crossing of the red and blue surfaces in 3D since their angular shape is invariant with radial distance from $\mathbf{r}_z$. Adapted from [20].

directions from zero at $\mathbf{r}_z$ and if, say, $\mathbf{M}$ is a positive-definite matrix, then $\mathbf{v}^T\mathbf{M}\mathbf{v} = \delta > 0$ draws ellipsoidal surfaces that enclose $\mathbf{r}_z$. When one of $\mathbf{M}$ or $\mathbf{N}$ is positive or negative definite, then, zero C lines pass through the dark spot ($\mathbf{E}\cdot\mathbf{E} = 0$ is only satisfied at $\mathbf{r}_z$ as a byproduct of $\mathbf{E}(\mathbf{r}_z) = \mathbf{0}$. This does not mean that $\mathbf{r}_z$ is strictly a C point because polarisation is completely undefined when the electric field is zero).

5.1.2 L lines

Linear electric polarisation is identified when the electric contribution to spin angular momentum density is zero or, identically, the normal vector to the polarisation ellipse $\mathbf{n} = \mathbf{p} \times \mathbf{q}$ is zero, where $\mathbf{p} = \Re\{\mathbf{E}\}$ and $\mathbf{q} = \Im\{\mathbf{E}\}$. Both $\mathbf{p}$ and $\mathbf{q}$ can be calculated in the first-order approximation as,

$$\begin{aligned} \mathbf{p} &\approx \Re\{\mathbf{J}_\mathrm{E}\}\mathbf{v}, \\ \mathbf{q} &\approx \Im\{\mathbf{J}_\mathrm{E}\}\mathbf{v}, \end{aligned} \tag{5.4}$$

and their cross product is zero when the two vectors are parallel, that is $\Re\{\mathbf{J}_\mathrm{E}\}\mathbf{v} = a\Im\{\mathbf{J}_\mathrm{E}\}\mathbf{v}$, where a is a scalar. This leads to the eigenproblem,

$$\Im\{\mathbf{J}_\mathrm{E}\}^{-1}\Re\{\mathbf{J}_\mathrm{E}\}\mathbf{v} = a\mathbf{v}, \tag{5.5}$$

whose solutions in $\mathbf{v}$ are parallel to the three eigenvectors of the 3×3 matrix $\Im\{\mathbf{J}_\mathrm{E}\}^{-1}\Re\{\mathbf{J}_\mathrm{E}\}$ which are either all three real, or a mixture of one real eigenvector and a conjugate pair of complex eigenvectors. Of course $\mathbf{v}$ cannot point in a complex direction, it being the position vector in our first-order approximation so we can conclude simply that either one or three L lines always cross in real-space through the dark spot at $\mathbf{r}_\mathrm{z}$ ($\mathbf{v} = \mathbf{0}$).

5.1.3 Combinations

As C lines and L lines are forced to combine by the constraints $\mathbf{E}(\mathbf{r}_\mathrm{z}) = \mathbf{0}$ any of six possible permutations of a point-like dark spot can emerge. Zero, two or four C lines can intersect either one or three L lines as shown in Fig. 5.2, where dark spots were deliberately synthesised in the non-paraxial interference of ten plane waves

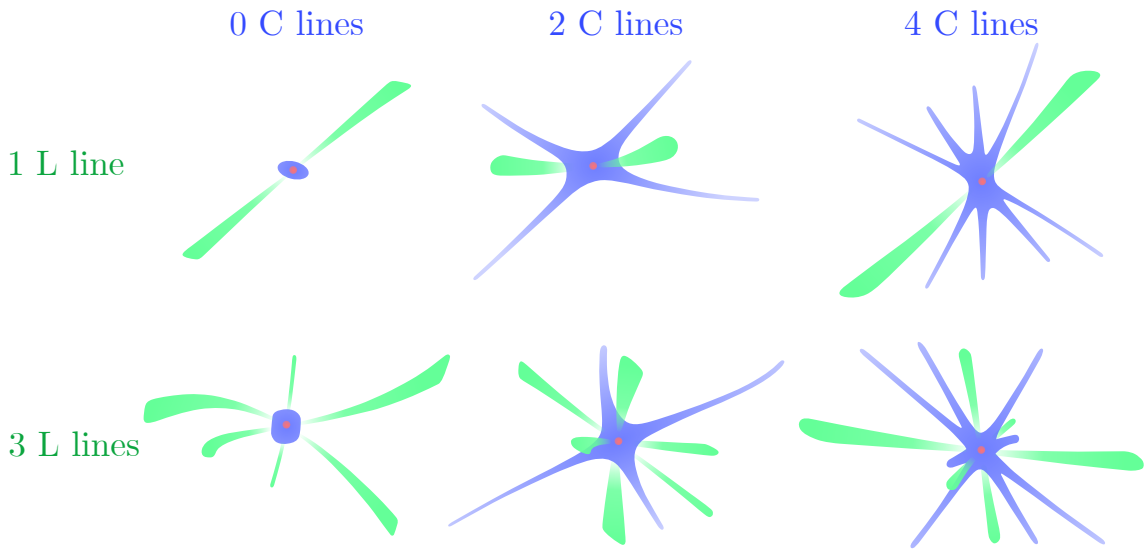

Figure 5.2: Each of the six possible first-order dark spots (red circle, position $\mathbf{r}_z$) that can be realised in terms of the combination of polarisation singularities (C lines, blue and L lines, green) that intersect. Either zero, two or four C lines and one or three L lines always cross at the point-like singularity's position. Each dark spot is created in the interference of ten plane waves with a unique set of random wavevectors, that are then polarised specifically to realise $\mathbf{E}(\mathbf{r}_z) = \mathbf{0}$. The polarisation singularities of the exact electric field function (including derivatives to all orders) are plotted in this figure. Adapted from [20].

with random wavevectors, a different set of ten for each dark spot. Though we used a first-order approximation of the electric field near the dark spot to argue this result, the number of crossing polarisation singularities persists in the exact electric field function. Polarisation singularities cannot terminate unexpectedly though it is possible that any two C line tips or any two L line tips of the examples of Fig. 5.2 join together when followed further away from $\mathbf{r}_z$.

5.2 A dark spot's point-like vector singularities

Flows of power and linear and angular momentum in monochromatic electromagnetic fields are, in their dual definitions, calculated using both the **E** and **H** phasors.

Therefore when $\mathbf{E}(\mathbf{r}_z) = \mathbf{0}$ in an electric field dark spot some of these quantities—certainly the electric field's contribution—also vanish to form point-like vector field singularities centred on the dark spot's location, $\mathbf{r}_z$. Each vector singularity is characterisable by the field in question's Jacobian matrix [dyadic $D(*)$]. The singularities, while individually stable, are brought to coalesce unstably at the same point $\mathbf{r}_z$ by the conditions $\mathbf{E}(\mathbf{r}_z) = \mathbf{0}$. In this section we will index the vector singularities induced in the Poynting vector, the imaginary Poynting vector, the electric orbital and spin currents and discuss the dark spot's SAM density, principally by calculating the relevant vector's dyadic matrix—we will only consider first-order derivatives of these vectors. This is not an unreasonable restriction because as along as the first-order derivatives of a vector $\mathbf{V}$ are non-zero at $\mathbf{r}_z$ (where $\mathbf{V}(\mathbf{r}_z) = \mathbf{0}$), then the resultant vector singularity at $\mathbf{r}_z$ cannot have a topological degree greater than 1 in magnitude. Like the azimuthal phase circulation caused by a scalar vortex, the topological imprint of this vector singularity on the exact function of the surrounding vector field $\mathbf{V}$ is always preserved on any closed surface of any size containing $\mathbf{r}_z$ and no other singularities of $\mathbf{V}$. Derivation of dyadics can be found in this chapter's appendix.

5.2.1 Poynting vector

We might recall from the first chapter that the Poynting vector, measuring the flux of active power in light, is given by,

$$\mathbf{P} = \frac{1}{2}\Re\{\mathbf{E}^* \times \mathbf{H}\}. \tag{5.6}$$

The Poynting vector definition contains inter-vector multiplication of $\mathbf{E}$ and $\mathbf{H}$ so that only one phasor need be zero for the Poynting vector to be zero too. That said, it is also possible for the Poynting vector to vanish in regions of non-zero intensity

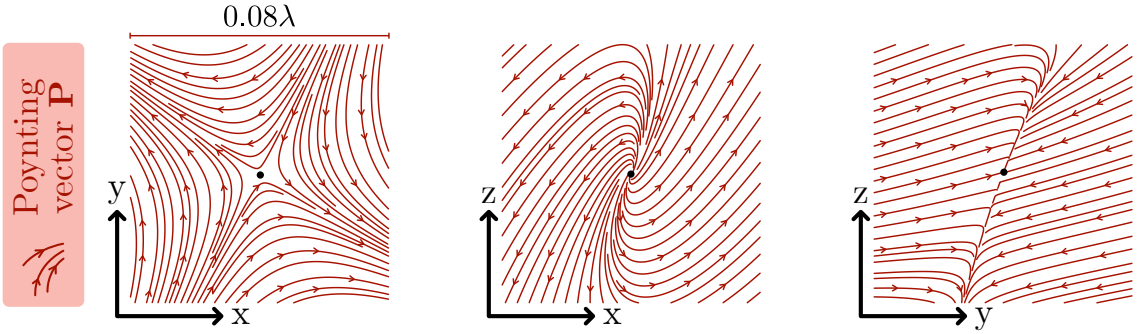

Figure 5.3: Example divergence-free saddle set up in the Poynting vector in 3D space by an electric field singularity at $\mathbf{r}_z$ (black circle). For visualisation the flux of the Poynting vector is shown on three cut planes; on some planes there may appear to be a net flux (e.g., on the xz and yz planes) but this is compensated for by out-of-plane flow of the vector. Adapted from [20].

(for example a standing wave where there is no transfer of active power, but still an oscillating electromagnetic field where the instantaneous $\boldsymbol{\mathcal{E}}$ and $\boldsymbol{\mathcal{H}}$ vectors are always parallel or antiparallel). General Poynting vector singularities were studied and indexed in [120] and the authors' findings of 'electric-field-induced' singularities apply to the case of a point-like electric field dark spot. In free space where there are no sources or sinks of electromagnetic energy the Poynting vector must have zero divergence according to Eq. (2.7), meaning its Jacobian matrix [first-order dyadic $D(\mathbf{P})$] [20],

$$D(\mathbf{P}) = \frac{c^2}{2\omega}\epsilon_0 \Im\{(\mathbf{J}_\mathrm{E}^T - \mathbf{J}_\mathrm{E})\mathbf{J}_\mathrm{E}^*\}, \tag{5.7}$$

must have a mixture of positive and negative (real or complex) eigenvalues*; real parts signed $(+,+,-)$ or $(+,-,-)$ in any order, such that two types of singularity (both saddle points) can form in the Poynting vector when the electric field is zero. Equation (5.7) is defined only using the electric field Jacobian $\mathbf{J}_\mathrm{E}$, possible because the $\mathbf{H}$ phasor in Eq. (5.6) can be replaced with the curl of $\mathbf{E}$ using Maxwell's equa-

*The divergence of a vector $\mathbf{F}$ is the trace of its dyadic, tr $D(\mathbf{F})$, equal to the sum of the dyadic's eigenvalues. It is only possible for the eigenvalues to sum to zero and ensure $\nabla \cdot \mathbf{F} = 0$ if they do not all have the same sign.

tions (a magnetic version defined using $\mathbf{J}_\mathrm{H}$ exists and is equally true). An example of a Poynting vector singularity formed in a dark spot is given in Fig. 5.3, where three orthogonal cut planes are taken with the on-plane projection of Poynting vector streamlines. The 3D flux of the Poynting vector is divergence-less and any apparent net flow of field lines on one cut plane is compensated on other cut planes by opposite flow (e.g., see the xz and yz planes of Fig. 5.3). Point-like Poynting vector singularities have been identified recently in non-paraxial near fields [121–123]. Two-dimensional transverse Poynting vector singularities, perhaps resembling one of the cut planes of Fig. 5.3, exist in beams and have been studied in depth [64, 124–126].

5.2.2 Imaginary Poynting vector

Testament to how often the imaginary Poynting vector (IPV) is ignored is the fact that the real part of the complex time-averaged Poynting vector $(1/2)\,\mathbf{E}^* \times \mathbf{H}$ is widely called the 'Poynting vector' (just as we did in the last subsection). For the IPV, defined as

$$\mathbf{P}_\mathrm{i} = \frac{1}{2}\Im\{\mathbf{E}^* \times \mathbf{H}\}, \tag{5.8}$$

does not describe active power flow, rather *reactive* power flow, the flux of reactive energy density $\propto \epsilon_0|\mathbf{E}|^2 - \mu_0|\mathbf{H}|^2$. Much recent interest in the IPV is motivated by the optical force term to which it couples [42, 43] that was only recently experimentally measured [41], providing an additional degree of freedom beyond radiation pressure and gradient forces that can be independently structured [40]. Unlike the familiar Poynting vector, the IPV is dual-asymmetric meaning the sign of the vector changes after swapping $\mathbf{E} \to \mathbf{H}$ and $\mathbf{H} \to -\mathbf{E}$. This asymmetry could be harnessed to control

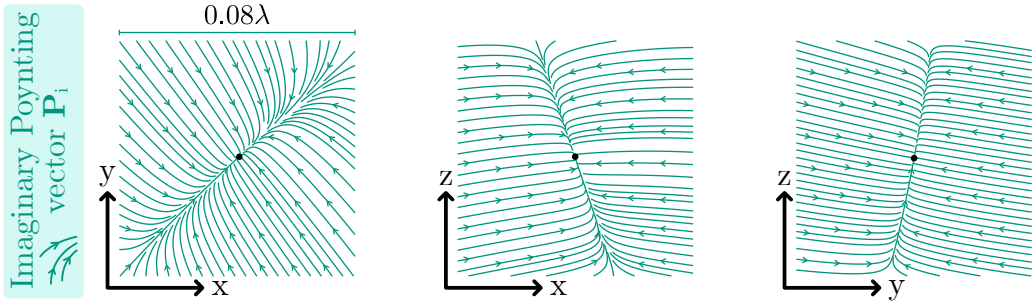

Figure 5.4: Example sink singularity set up in the imaginary Poynting vector in 3D space by an electric field dark spot at $\mathbf{r}_z$ (black circle). The flux of the imaginary Poynting vector is projected onto three cut planes. Adapted from [20].

directional scattering from Janus particles[†] [38, 39].

Discrepancy between the energy density contributions from $\mathbf{E}$ and from $\mathbf{H}$ sets up sources and sinks of the IPV because of the relation [37]

$$\nabla \cdot \mathbf{P}_i = \frac{\omega}{2}\left(\epsilon_0|\mathbf{E}|^2 - \mu_0|\mathbf{H}|^2\right), \tag{5.9}$$

from which it follows that if $\mathbf{E}(\mathbf{r}_z) = \mathbf{0}$ and $\mathbf{H}(\mathbf{r}_z) \neq \mathbf{0}$ then the divergence Eq. (5.9) is negative at $\mathbf{r}_z$. Electric field zeros are able to construct sinks of the IPV while zeros of the magnetic field phasor can construct sources of the IPV, a property intrinsic to the imaginary Poynting vector's dyadic,

$$D(\mathbf{P}_i) = -\frac{c^2}{4\omega}\epsilon_0 \Re\{(\mathbf{J}_E^T - \mathbf{J}_E)\mathbf{J}_E^*\} + \frac{c^2}{4\omega}\mu_0 \Re\{(\mathbf{J}_H^T - \mathbf{J}_H)\mathbf{J}_H^*\}, \tag{5.10}$$

written in dual representation. Note that in the case of $\mathbf{E}(\mathbf{r}_z) = \mathbf{0}$ Maxwell's equations force $\mathbf{J}_H$ to be a symmetric matrix[‡] so that the second term of Eq. (5.10)

[†]In a Janus particle, a plane wave excites a Janus dipole which is characterised by orthogonal electric and magnetic dipole moments that are out of phase (e.g., $\mathbf{p}_d = 1\hat{\mathbf{x}}$ and $\mathbf{m}_d = ic\hat{\mathbf{y}}$). This dipole generates a flow of reactive power, the IPV, in a preferred direction.

[‡]The off-diagonal elements of $\mathbf{J}_H^T - \mathbf{J}_H$ are the components of $\nabla \times \mathbf{H}$. From Maxwell's equations, if $\mathbf{E} = \mathbf{0}$ then $\nabla \times \mathbf{H} = \mathbf{0}$ and therefore $\mathbf{J}_H^T - \mathbf{J}_H = \mathbf{0}$. The same is true of $\mathbf{J}_E$ when $\mathbf{H} = \mathbf{0}$.

vanishes. This way the trace of $D(\mathbf{P}_\mathrm{i})$, the IPV's divergence, is negative and equal to the sum of the matrix's eigenvalues which cannot, therefore, be all three positive. The type of IPV singularity set up by the electric field dark spot can either be a sink, or a negative divergence saddle. An example sink singularity is given in Fig. 5.4.

5.2.3 Canonical momentum

The orbital component of the Poynting vector, known as orbital current, is proportional to light's canonical momentum by a factor of c^2, transferable to matter via radiation pressure. Canonical momentum can be thought of as a local wavevector to be defined in non-paraxial light where there is no homogeneous propagation direction; it is the canonical momentum that is twisted around the OAM-carrying optical vortex, informing the way in which matter is able to orbit the vortex centre. Recalling from chapter 2 canonical momentum is defined fundamentally as

$$\mathbf{p} = \mathbf{p}_\mathrm{e} + \mathbf{p}_\mathrm{m} = \frac{1}{4\omega}\Im\{\epsilon_0\mathbf{E}^* \cdot (\nabla)\mathbf{E} + \mu_0\mathbf{H}^* \cdot (\nabla)\mathbf{H}\}, \tag{5.11}$$

accounting for contributions from both the electric and magnetic fields. Though it is true that an electric field dark spot alone generally does not eliminate canonical momentum (since $\mathbf{p}_\mathrm{m}$ may be non-zero at a point where $\mathbf{E} = \mathbf{0}$) it is reasonable to consider electric and magnetic momenta separately because matter does not respond to $\mathbf{E}$ and $\mathbf{H}$ fields equally, particles usually having a larger electric polarisability.

Singularities of $\mathbf{p}$, $\mathbf{p}_\mathrm{e}$ and $\mathbf{p}_\mathrm{m}$ are all stable and point-like in ordinary monochromatic interference [57], and as $\mathbf{E}(\mathbf{r}_\mathrm{z}) = \mathbf{0}$ necessarily forces $\mathbf{p}_\mathrm{e} = \mathbf{0}$ an electric canonical momentum singularity is anchored to a dark spot at $\mathbf{r}_\mathrm{z}$. But compounded by the suppression of the electric field this dark-spot-coupled $\mathbf{p}_\mathrm{e}$ singularity acquires non-generic, remarkable properties. The dyadic of $\mathbf{p}_\mathrm{e}$ when evaluated at the dark

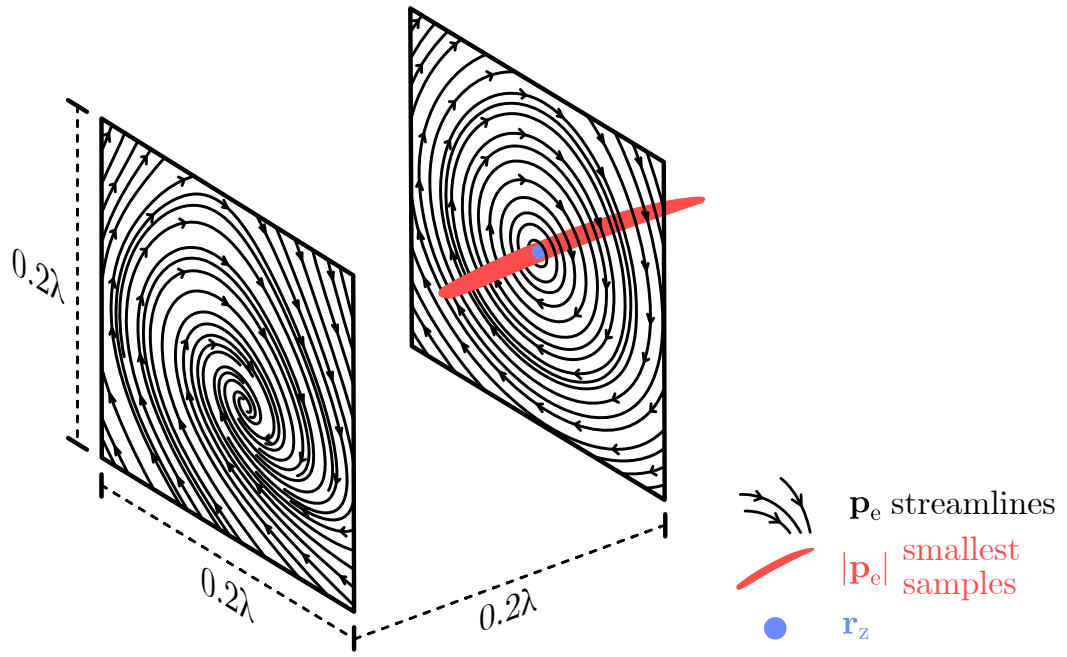

Figure 5.5: The localised vortex of electric canonical momentum established by a point-like electric field dark spot. Streamlines of $\mathbf{p}_e$ are plotted on two planes, one coinciding with the dark spot (blue circle), showing the vortex-like circulation of momentum which tends to dissolve with distance from the dark spot. This dissolution happens because the canonical momentum singularity is in fact point-like, but always rather elongated as shown by the red volume bounding the smallest 5000 samples of $|\mathbf{p}_e|$ in the analytic simulation of the dark spot. Adapted from [20].

spot location is

$$D(\mathbf{p}_e) = \frac{1}{4\omega}\epsilon_0 \Im\{\mathbf{J}_E^T \mathbf{J}_E^*\}, \tag{5.12}$$

which unlike dyadics given earlier in this chapter, is an anti-symmetric matrix, meaning $D(\mathbf{p}_e) = -D(\mathbf{p}_e)^T$. Anti-symmetry forces the eigenvalues of $D(\mathbf{p}_e)$ to be purely imaginary while the matrix's trace is zero because $\mathbf{p}_e$, like the Poynting vector, is divergence-less in free space. The consequence is that the singularity of $\mathbf{p}_e$ at an electric field dark spot is classed a circulation; a singularity that resembles a vortex line in the region near to $\mathbf{r}_z$ where first-order derivatives of $\mathbf{p}_e$ dominate. While it is still strictly point-like, the conditions $\mathbf{E}(\mathbf{r}_z) = \mathbf{0}$ elongates the $\mathbf{p}_e$ singularity and

around it, streamlines of $\mathbf{p}_e$ circulate in a vortex structure as shown in the example given in Fig. 5.5. In it, streamlines of $\mathbf{p}_e$ are projected onto two planes, one coinciding with an electric field zero (blue circle), highlighting the local momentum vortex structure about $\mathbf{r}_z$ (losing definition with distance from $\mathbf{r}_z$). A red volume indicates the elongated shape of the singularity, defined over the smallest 5000 samples of $|\mathbf{p}_e|$ in the analytic simulation (In Fig. 5.5 the exact function $\mathbf{p}_e$ is plotted and is only truly zero at a single point $\mathbf{r}_z$, the blue circle. If Taylor-expanded to first order meaning $\mathbf{p}_e \approx D(\mathbf{p}_e)(\mathbf{r} - \mathbf{r}_z)$, then the approximate function of $\mathbf{p}_e$, valid for small displacements $\mathbf{r} - \mathbf{r}_z$, is exactly zero along a line running parallel to the red volume in Fig. 5.5. In some sense, then, the $\mathbf{p}_e$ singularity is halfway between being a point-like and a line structure). The real part of the local electric wavevector,

$$\Re\{\mathbf{k}_e\} = \Re\{-i\mathbf{e}^* \cdot (\nabla)\mathbf{e}\} = \frac{4\omega}{\epsilon_0 \mathbf{E}^* \cdot \mathbf{E}} \mathbf{p}_e, \tag{5.13}$$

where $\mathbf{e} = \mathbf{E}/\sqrt{\mathbf{E}^* \cdot \mathbf{E}}$, points in the direction of electric canonical momentum, defining the local phase gradient of the electric field. While canonical momentum approaches zero near $\mathbf{r}_z$ the electric local wavevector diverges, becoming superoscillatory [57, 127]. The axis of the canonical momentum vortex can be found from the one real eigenvector of $D(\mathbf{p}_e)$.

5.2.4 Spin momentum

Spin momentum $\mathbf{p}^s$ is the spin counterpart to canonical momentum satisfying $c^2\mathbf{p} + c^2\mathbf{p}^s = \mathbf{P}$, $\mathbf{P}$ being the Poynting vector. Like canonical momentum, spin momentum contains electric and magnetic contributions—each is half the curl of the field's spin

angular momentum density,

$$\mathbf{p}^{\mathrm{s}} = \mathbf{p}^{\mathrm{s}}_{\mathrm{e}} + \mathbf{p}^{\mathrm{s}}_{\mathrm{m}} = \frac{1}{2}\nabla \times \frac{1}{4\omega}\Im\{\epsilon_0 \mathbf{E}^* \times \mathbf{E} + \mu_0 \mathbf{H}^* \times \mathbf{H}\}. \tag{5.14}$$

Despite the different vector operations executed in Eq. (5.11) and Eq. (5.14) electric spin momentum's dyadic, evaluated in an electric field zero, takes a similar form to Eq. (5.12),

$$D(\mathbf{p}^{\mathrm{s}}_{\mathrm{e}}) = -\frac{1}{4\omega}\epsilon_0 \Im\{\mathbf{J}_{\mathrm{E}}\mathbf{J}^*_{\mathrm{E}}\}, \tag{5.15}$$

though without sharing the dyadic of canonical momentum's anti-symmetric property. Much like the Poynting vector the point-like singularity of $\mathbf{p}^{\mathrm{s}}$ located at an electric field dark spot is a divergence-free saddle point with signed eigenvalues $(+,-,-)$ or $(+,+,-)$.

5.2.5 Spin angular momentum

In chapter 2 we provided an expression for spin angular momentum (SAM) density,

$$\mathbf{S} = \mathbf{S}_{\mathrm{e}} + \mathbf{S}_{\mathrm{m}} = \frac{1}{4\omega}\Im\{\epsilon_0 \mathbf{E}^* \times \mathbf{E} + \mu_0 \mathbf{H}^* \times \mathbf{H}\}, \tag{5.16}$$

whose curl is proportional to the spin momentum Eq. (5.14). Above is the dual-symmetric definition of SAM density summing vectors which are normal to the electric and magnetic polarisation ellipses formed over space. Since we are concerned with only the electric field being zero at a location $\mathbf{r}_{\mathrm{z}}$ a singularity in the *total* SAM vector does not develop, rather only the electric spin is zero. While the behaviour of electric spin in the neighbourhood of a dark spot we have largely already accounted for by showing that one or three L lines (lines of zero electric spin) intersect, the

specific texture of the $\mathbf{S}_\mathrm{e}$ vector is too complicated to be captured by the dyadic of Eq. (5.16) at $\mathbf{r}_\mathrm{z}$, which is zero because $\mathbf{J}_\mathrm{H}$ is forced to be symmetric by Maxwell's equations:

$$D(\mathbf{S}_\mathrm{e}) = \frac{1}{4\omega^2}\epsilon_0 \Re\{(\mathbf{J}_\mathrm{H}^T - \mathbf{J}_\mathrm{H})\mathbf{J}_\mathrm{E}^*\} = \mathbf{0}. \tag{5.17}$$

A higher-order Taylor expansion of $\mathbf{S}_\mathrm{e}$, including derivatives beyond the those (first-order) accounted for by its dyadic Eq. (5.17), would be needed to properly describe the flux of $\mathbf{S}_\mathrm{e}$ at a dark spot.

5.3 Remarks on duality

Our treatment of non-paraxial dark spots in this chapter has been biased towards the electric field and its contributions to light's dynamic quantities, neglecting to some extent the so-called 'electromagnetic democracy' [33, 128] that maintains that in free space the $\mathbf{E}$ and $\mathbf{H}$ fields belong with equal importance in the definitions of light's total energy, momentum and spin angular momentum densities (ensuring that these definitions are dual-symmetric). While in light-matter interactions it is quite reasonable to favour electric quantities (because particles normally have larger electric polarisability), many of the vector singularities coupled to $\mathbf{E} = \mathbf{0}$ change or disappear entirely after a duality transform.

A continuous duality transform replaces the $\mathbf{E}$ and $\mathbf{H}$ phasors with transformed versions $\mathbf{E}'$ and $\mathbf{H}'$ that mix together the original $\mathbf{E}$ and $\mathbf{H}$ vectors [34, 36],

$$\begin{aligned} \mathbf{E} \to \mathbf{E}' &= \mathbf{E}\cos\theta + \eta\mathbf{H}\sin\theta, \\ \mathbf{H} \to \mathbf{H}' &= \mathbf{H}\cos\theta - \frac{1}{\eta}\mathbf{E}\sin\theta, \end{aligned} \tag{5.18}$$

where $\eta = \sqrt{\mu_0/\epsilon_0}$ and θ is the transformation angle. The transform's significance is that Maxwell's equations are unchanged[§] by substituting $\mathbf{E} \to \mathbf{E}'$ and $\mathbf{H} \to \mathbf{H}'$. Equation (5.18) is a rotation through an angle θ in $\mathbb{C}^2$ space of an abstract vector-valued vector, the electromagnetic bispinor [33, 52, 53, 129] for which $\mathbf{E}$ and $\mathbf{H}$ are vector-valued components, not strictly a rotation in real space of the $\mathbf{E}$ and $\mathbf{H}$ vectors themselves. Supposing that there is dark spot in $\mathbf{E}$ every quarter turn of the bispinor swaps the dark spot between the transformed $\mathbf{E}'$ and $\mathbf{H}'$ fields as $\cos\theta$ and $\sin\theta$ periodically pass zero. Total energy density, being shared unevenly between $\mathbf{E}$ and $\mathbf{H}$ because only $\mathbf{E}$ is zero, stays constant throughout the transformation but the intrinsic asymmetry in its distribution between the fields is exchanged between reactive energy density (maximal when $\theta = 0$) and a quantity sometimes called magnetoelectric energy density [53], proportional to reactive helicity density[¶], $\propto \Re\{\mathbf{E}'^* \cdot \mathbf{H}'\}$ [130] in the transformed field:

$$\begin{aligned} \frac{1}{4}\left(\epsilon_0|\mathbf{E}'|^2 - \mu_0|\mathbf{H}'|^2\right) &= \frac{1}{4}\left(\epsilon_0|\mathbf{E}|^2 - \mu_0|\mathbf{H}|^2\right)\cos 2\theta + \frac{1}{2c}\Re\{\mathbf{E}^* \cdot \mathbf{H}\}\sin 2\theta, \\ \frac{1}{2c}\Re\{\mathbf{E}'^* \cdot \mathbf{H}'\} &= \frac{1}{2c}\Re\{\mathbf{E}^* \cdot \mathbf{H}\}\cos 2\theta - \frac{1}{4}\left(\epsilon_0|\mathbf{E}|^2 - \mu_0|\mathbf{H}|^2\right)\sin 2\theta. \end{aligned} \tag{5.19}$$

Meanwhile those of the vectors discussed in the last section that violate dual symmetry are, along with their singularities, altered by the $\mathbb{C}^2$-space rotation Eq. (5.18). These vectors include the imaginary Poynting vector, the flux of reactive energy

[§]This is the continuous symmetry that in vacuum results in helicity conservation. One way to retain this symmetry in the presence of electric charge density $\rho_\mathrm{e} \neq 0$ is if magnetic charge density ρ_m is introduced [32].

[¶]Non-zero reactive energy and reactive helicity densities are exclusive to non-paraxial fields. Reactive helicity density quantifies a type of chirality of the local geometry of the $\boldsymbol{\mathcal{E}}$ and $\boldsymbol{\mathcal{H}}$ vectors that is present if the angle between them is not ninety degrees, averaged over one oscillation. Even without considering any other vectors (e.g., $\mathbf{k}$), this sort of geometry cannot be superimposed with its mirror image (meaning after parity inversion $\mathbf{E} \to -\mathbf{E}, \mathbf{H} \to \mathbf{H}$).

density, transformed using Eq. (5.18) according to,

$$\mathbf{P}_{\mathrm{i}}' = \mathbf{P}_{\mathrm{i}} \cos 2\theta - \omega c(\mathbf{S}_{\mathrm{e}} - \mathbf{S}_{\mathrm{m}}) \sin 2\theta, \tag{5.20}$$

the electric canonical momentum, transformed according to,

$$\mathbf{p}_{\mathrm{e}}' = \mathbf{p}_{\mathrm{e}} \cos^2\theta + \mathbf{p}_{\mathrm{m}} \sin^2\theta - \frac{1}{4\omega c} \nabla \times \mathbf{P}_{\mathrm{i}} \sin 2\theta, \tag{5.21}$$

the electric spin momentum,

$$\mathbf{p}_{\mathrm{e}}^{\mathrm{s}\prime} = \mathbf{p}_{\mathrm{e}}^{\mathrm{s}} \cos^2\theta + \mathbf{p}_{\mathrm{m}}^{\mathrm{s}} \sin^2\theta + \frac{1}{4\omega c} \nabla \times \mathbf{P}_{\mathrm{i}} \sin 2\theta, \tag{5.22}$$

and the electric SAM density,

$$\mathbf{S}_{\mathrm{e}}' = \mathbf{S}_{\mathrm{e}} \cos^2\theta + \mathbf{S}_{\mathrm{m}} \sin^2\theta + \frac{1}{2\omega c} \mathbf{P}_{\mathrm{i}} \sin 2\theta. \tag{5.23}$$

Given an electric dark spot $\mathbf{E}(\mathbf{r}_{\mathrm{z}}) = \mathbf{0}$ these vectors, which are zero for $\theta = 0$, obtain non-zero flux from the magnetic field after a duality transformation so that the vector singularity no longer exists at $\mathbf{r}_{\mathrm{z}}$. Some quantities emerging in Eqs. (5.19)-(5.23) such as reactive spin [130] (the difference between electric and magnetic spins $\mathbf{S}_{\mathrm{e}} - \mathbf{S}_{\mathrm{m}}$) are scarcely (if at all) recognised in the literature though our very recent work (in preparation) proposes a framework unifying them and other better-known quadratic quantities in light [37]. This work has greatly helped to develop our original comments on duality and dark spots in [20]. Further study could identify how vector singularities behave in the volume of space around $\mathbf{r}_{\mathrm{z}}$ after a duality transform, particularly how the intersection of electric polarisation singularities dissociates and reforms in $\mathbf{H}$ (and again in $\mathbf{E}$) during transformation.

Singularities which are invariant to the transformation Eq. (5.18) can be achieved in a perfectly dual point-like zero where $\mathbf{E} = \mathbf{H} = \mathbf{0}$ in non-paraxial light (note that in paraxial fields there is a more symmetric relationship between $\mathbf{E}$ and $\mathbf{H}$ in that if one field vanishes, the other must also vanish to obey Maxwell's equations. This is not the case in the non-paraxial regime where fields are freely polarisable in 3D, for instance in the centre of an azimuthal beam or in the offset $\mathbf{E}$ and $\mathbf{H}$ field nodes of a linearly polarised standing wave). For then the *total* canonical momentum density, *total* spin momentum density and *total* spin angular momentum densities, all of which are dual-symmetric, are suppressed too. A dual dark spot is, however, an even more unstable entity that demands twelve real scalar conditions, six per $\mathbf{E} = \mathbf{0}$ and $\mathbf{H} = \mathbf{0}$.

5.4 Chapter summary

Non-paraxial point-like dark spots and their coupled polarisation and vector singularities have been treated in this chapter and the characterisation of these singularities is summarised in Tab. 5.1. A key result of this chapter is that a first-order electric field dark spot is an intersection point for one of six possible combinations of lines of circular and linear polarisation. Based on these polarisation singularity combinations, and the possible permutations of eigenvalue signs of the dyadics of the Poynting vector $\mathbf{P}$ (2), the imaginary Poynting vector $\mathbf{P}_\mathrm{i}$ (3), the electric spin current $\mathbf{p}_\mathrm{e}^\mathrm{s}$ (2), and the electric canonical momentum $\mathbf{p}_\mathrm{e}$ (1) that can occur independently, we can infer that there are 72 possible distinct incarnations of an electric field dark spot (in our framework).

Being a point-like, 3D-confined singularity the dark spot has skyrmionic features both in terms of field vectors like the instantaneous electric field or the Poynting

	dyadic at $\mathbf{r}_z$	associated singularity	singularity type	dyadic characteristic
	$\mathbf{J}_E$	**E**	saddle	electric field Jacobian
1.	$\Im\{\mathbf{J}_E\}^{-1}\mathrm{Re}\{\mathbf{J}_E\}$	L lines	n/a	one or three real eigenvectors are directions of L lines
2.	$\Re\{\mathbf{J}_E^T\mathbf{J}_E\}$	C lines	n/a	dyadics 2 and 3 define quadric surfaces M and N, respectively. Intersection lines of M and N are C lines
3.	$\Im\{\mathbf{J}_E^T\mathbf{J}_E\}$	C lines	n/a	
4.	$\Im\{\mathbf{J}_E^T\mathbf{J}_E^*\}$	$\mathbf{p}_e$	circulation	real eigenvector gives the axis of $\mathbf{p}_e$ vortex
5.	$-\Im\{\mathbf{J}_E\mathbf{J}_E^*\}$	$\mathbf{p}_e^s$	saddle	eigenvalues signs give exact topology of minimum
6.	$\Im\{(\mathbf{J}_E^T-\mathbf{J}_E)\mathbf{J}_E^*\}$	**P**	saddle	
7.	$-\Re\{(\mathbf{J}_E^T-\mathbf{J}_E)\mathbf{J}_E^*\}$	$\mathbf{P}_i$	saddle or sink	

Table 5.1: Classification of a point-like electric field dark spot based on its coupled polarisation and vector singularities, summarised in seven matrices (numbered). The first three matrices relate to the number of C lines and L lines that intersect at $\mathbf{r}_z$. Matrices 4-7 are proportional to the dyadics (Jacobian matrices) of electromagnetic vectors that were discussed in this chapter, evaluated at $\mathbf{r}_z$. The table is adapted from [20].

vector and in also in terms of polarisation. Point-like vector singularities cause, on a closed surface where the vector is well-defined containing the singularity, the vector in question to point in every 3D direction at least once in the same way as an optical skyrmion in, say, the spin vector **S**, realises every 3D orientation of **S** on a 2D surface which can be wrapped over a sphere surface in 3D parameter space‖ [106, 131]. Meanwhile as the point-like dark spot can be crossed simultaneously by C lines and L lines, on which are the extremes of the polarisation ellipse, a smooth transition from circular to linear polarisation in the volume of the dark spot must be provided by nested surfaces of constant-ellipticity polarisation. However, three-dimensional polarisation ellipses have *four* degrees of freedom as angles—two angles specifying the 3D direction of the ellipse normal **n**, and two further angles for the tilt and ellipticity of the ellipse within the plane normal to **n** [92]—so it is not true that all possible polarisation ellipse shapes in all orientations manifest in the span of *three* spatial dimensions about the dark spot; this is only possible in a higher-dimensional

‖Spin skyrmions can be generated in non paraxial fields which admit transverse components to the SAM density vector **S**. By specially structuring evanescent waves, for example, **S** can be made to point in every 3D direction, organising certain types of skyrmion [131].

parameter space. In a six-dimensional parameter space (in which $\mathbf{E}(\mathbf{r}_z^{6D}) = \mathbf{0}$ is stable) the six-vector $(\mathbf{p}, \mathbf{q})^T$, a concatenation of the real $\mathbf{p}$ and imaginary $\mathbf{q}$ parts of the electric field phasor $\mathbf{E} = \mathbf{p} + i\mathbf{q}$, winds over a hypersphere enclosing the singularity indicating a realisation of every 3D polarisation ellipse and every phase in 6D space. Electromagnetic fields in 'higher-dimensional parameter spaces' may sound hypothetical but have in fact been probed experimentally, for instance in [117] where the topological properties and response to perturbation of a point-like singularity created from a metasurface was determined in a four-dimensional parameter space, (x, y, z, λ).

What motivated this study was largely the theoretical interest, given that there was at the time no clear approach to classify point-like dark spots and their field imprint, particularly in polarisation structure, was not understood. Although point-like dark spots are not naturally occurring they can and have been deliberately created experimentally [117, 132] which given the findings of this chapter, presents the possibility for the topological control of electromagnetic fields, the capacity to engineer complicated polarisation and other vector structures beyond what light is capable of producing organically. Among their topological significance point-like dark spots could serve as a (as shall be discussed in the next chapter) controllable point-trap for matter. Optical traps usually rely on gradient force which as long as a particle has a positive polarisability, points in the direction of increasing energy density (electric energy density for electric particles). But at certain wavelengths for some particles polarisabilty can become negative, switching the direction of gradient force experienced by the particle, and it is in this way that a non-paraxial dark spot could serve as a fully confined trap with no escape channels. Gradient force is not the only force that particles are subject to, however—there are force terms in the dipole approximation that couple to the canonical momentum, Poynting vector, imaginary

Poynting vector and spin angular momentum vectors [42, 43], all of which are stirred into topological structures by the point-like zero as we showed—so it is important to have a comprehensive understanding of the flux of these force terms in the dark spot's neighbourhood as we have attempted to deliver here. We will attempt to further argue the experimental viability of dark spots in the next chapter, where we will present a simple technique for how dark spots can be position-controlled by modulating the polarisation of far field illumination.

5.5 Appendix: finding dyadics

Our analysis of the vector singularities that couple to electric dark spots has hinged on each vector's first-order dyadic evaluated in the position of the dark spot, $\mathbf{r}_{\mathrm{z}}$. We remind the reader that the dyadic of a vector $\mathbf{F}$, $D(\mathbf{F})$, is equivalent to that vector's Jacobian matrix,

$$D(\mathbf{F}) = \begin{pmatrix} \frac{\partial F_x}{\partial x} & \frac{\partial F_x}{\partial y} & \frac{\partial F_x}{\partial z} \\ \frac{\partial F_y}{\partial x} & \frac{\partial F_y}{\partial y} & \frac{\partial F_y}{\partial z} \\ \frac{\partial F_z}{\partial x} & \frac{\partial F_z}{\partial y} & \frac{\partial F_z}{\partial z} \end{pmatrix}, \tag{5.24}$$

although throughout this chapter we have reserved the term 'Jacobian matrix' mainly for those of the electric and magnetic field vectors ($\mathbf{J}_{\mathrm{E}}$ and $\mathbf{J}_{\mathrm{H}}$). The two matrices $\mathbf{J}_{\mathrm{E}}$ and $\mathbf{J}_{\mathrm{H}}$ we used as building blocks in the definitions of the dyadic of the Poynting vector Eq. (5.7), the imaginary Poynting vector Eq. (5.10), canonical momentum Eq. (5.12), spin momentum Eq. (5.15) and spin angular momentum Eq. (5.17). To produce these definitions we first wrote relevant vector operations between $\mathbf{E}$ and $\mathbf{H}$ as matrix-vector multiplications, usually after a substitution via Maxwell's equations

Eq. (2.3). For example, we can write:

$$\frac{1}{2}\mathbf{E}^* \times \mathbf{H} = -\frac{i}{2\omega\mu_0}\mathbf{E}^* \times (\nabla \times \mathbf{E}), \tag{5.25}$$

$$= -i\frac{c^2}{2\omega}\epsilon_0 \begin{pmatrix} E_y^*\left(\frac{\partial E_y}{\partial x} - \frac{\partial E_x}{\partial y}\right) - E_z^*\left(\frac{\partial E_x}{\partial z} - \frac{\partial E_z}{\partial x}\right) \\ E_z^*\left(\frac{\partial E_z}{\partial y} - \frac{\partial E_y}{\partial z}\right) - E_x^*\left(\frac{\partial E_y}{\partial x} - \frac{\partial E_x}{\partial y}\right) \\ E_x^*\left(\frac{\partial E_x}{\partial z} - \frac{\partial E_z}{\partial x}\right) - E_y^*\left(\frac{\partial E_z}{\partial y} - \frac{\partial E_y}{\partial z}\right) \end{pmatrix}, \tag{5.26}$$

$$= -i\frac{c^2}{2\omega}\epsilon_0 \left[\begin{pmatrix} \frac{\partial E_x}{\partial x} & \frac{\partial E_y}{\partial x} & \frac{\partial E_z}{\partial x} \\ \frac{\partial E_x}{\partial y} & \frac{\partial E_y}{\partial y} & \frac{\partial E_z}{\partial y} \\ \frac{\partial E_x}{\partial z} & \frac{\partial E_y}{\partial z} & \frac{\partial E_z}{\partial z} \end{pmatrix} - \begin{pmatrix} \frac{\partial E_x}{\partial x} & \frac{\partial E_x}{\partial y} & \frac{\partial E_x}{\partial z} \\ \frac{\partial E_y}{\partial x} & \frac{\partial E_y}{\partial y} & \frac{\partial E_y}{\partial z} \\ \frac{\partial E_z}{\partial x} & \frac{\partial E_z}{\partial y} & \frac{\partial E_z}{\partial z} \end{pmatrix} \right] \begin{pmatrix} E_x^* \\ E_y^* \\ E_z^* \end{pmatrix}, \tag{5.27}$$

$$= -i\frac{c^2}{2\omega}\epsilon_0(\mathbf{J}_{\mathrm{E}}^T - \mathbf{J}_{\mathrm{E}})\mathbf{E}^*. \tag{5.28}$$

Taking the real and imaginary parts of the final equality Eq. (5.28) obtains exact electric representations of the Poynting vector Eq. (5.6) and imaginary Poynting vector Eq. (5.8)—even though they are expressed using the electric Jacobian $\mathbf{J}_{\mathrm{E}}$ they are three-component vectors. What we have in fact achieved in Eq. (5.28) is an equivalent expression of the decomposition of the Poynting vector [to be seen later in Eq. (7.3)] as well as the imaginary Poynting vector [20, 37] because, of the individual terms found after expanding $(\mathbf{J}_{\mathrm{E}}^T - \mathbf{J}_{\mathrm{E}})\mathbf{E}^*$ into $\mathbf{J}_{\mathrm{E}}^T\mathbf{E}^* - \mathbf{J}_{\mathrm{E}}\mathbf{E}^*$, the first is the (electric) orbital contribution to the vector $(1/2)\mathbf{E}^* \times \mathbf{H}$ while the second term is the spin contribution. We see this because $\mathbf{J}_{\mathrm{E}}^T\mathbf{E}^*$ is equivalent to $\mathbf{E}^* \cdot (\nabla)\mathbf{E}$ and likewise $-2i\Im\{\mathbf{J}_{\mathrm{E}}\mathbf{E}^*\} \equiv \nabla \times (\mathbf{E}^* \times \mathbf{E})$, the latter holding as long as $\nabla \cdot \mathbf{E} = 0$. By alternatively substituting $\mathbf{E}^* = -i\nabla \times \mathbf{H}^*/(\omega\epsilon_0)$ in the first step Eq. (5.26) a magnetic representation of Eq. (5.28) can be found that uses $\mathbf{J}_{\mathrm{H}}$ and $\mathbf{H}$.

We find the dyadic of Eq. (5.28) by applying the product rule, namely,

$$D\left(\frac{1}{2}\mathbf{E}^*\times\mathbf{H}\right)=-i\frac{c^2}{2\omega}\epsilon_0\left[D(\mathbf{J}_{\mathrm{E}}^T-\mathbf{J}_{\mathrm{E}})\cdot\mathbf{E}^*+(\mathbf{J}_{\mathrm{E}}^T-\mathbf{J}_{\mathrm{E}})D(\mathbf{E}^*)\right] \tag{5.29}$$

where, adopting Einstein notation, $D(\mathbf{J}_{\mathrm{E}}^T-\mathbf{J}_{\mathrm{E}})=D(\mathbf{M})$ is a $3\times3\times3$ tensor $\partial_k M_{ij}$ that multiplies into $\mathbf{E}^*$ via $(\partial_k M_{ij})E_j^*$:

$$D\left(\frac{1}{2}\mathbf{E}^*\times\mathbf{H}\right)=-i\frac{c^2}{2\omega}\epsilon_0\left[(\partial_k M_{ij})E_j^*+(\mathbf{J}_{\mathrm{E}}^T-\mathbf{J}_{\mathrm{E}})\mathbf{J}_{\mathrm{E}}^*\right]. \tag{5.30}$$

While the second term of Eq. (5.30) $\propto(\mathbf{J}_{\mathrm{E}}^T-\mathbf{J}_{\mathrm{E}})\mathbf{J}_{\mathrm{E}}^*$ multiplies only first-order derivatives of $\mathbf{E}$, the first term multiplies second-order spatial derivatives of $\mathbf{E}$ with the zero-order electric field components E_j^*, which are by definition zero in the location of a dark spot $\mathbf{E}(\mathbf{r}_{\mathrm{z}})=E_j(\mathbf{r}_{\mathrm{z}})=\mathbf{0}$. Evaluated at an electric dark spot's position, then, only the second term of Eq. (5.30) survives and we arrive at,

$$D\left(\frac{1}{2}\mathbf{E}^*\times\mathbf{H}\right)\Big|_{\mathbf{r}_{\mathrm{z}}}=-i\frac{c^2}{2\omega}\epsilon_0(\mathbf{J}_{\mathrm{E}}^T-\mathbf{J}_{\mathrm{E}})\mathbf{J}_{\mathrm{E}}^*, \tag{5.31}$$

$$=\frac{c^2}{2\omega}\epsilon_0\Im\{(\mathbf{J}_{\mathrm{E}}^T-\mathbf{J}_{\mathrm{E}})\mathbf{J}_{\mathrm{E}}^*\}-i\frac{c^2}{2\omega}\epsilon_0\Re\{(\mathbf{J}_{\mathrm{E}}^T-\mathbf{J}_{\mathrm{E}})\mathbf{J}_{\mathrm{E}}^*\}, \tag{5.32}$$

whose real and imaginary parts are the dyadics of the Poynting vector Eq. (5.7) and imaginary Poynting vector Eq. (5.10) in an electric dark spot and in electric representation [hence the factor of two difference with the electric part of Eq. (5.10)]. Expanding the brackets within the $\Im\{*\}$ term one can arrive at the electric canonical and spin momentum density dyadics Eq. (5.12) and Eq. (5.15), up to a c^2 constant. With very similar steps to Eq. (5.26)-(5.28) applied to electric spin angular momentum density [beginning by substituting $\mathbf{E}=i\nabla\times\mathbf{H}/(\omega\epsilon_0)$] the dyadic Eq. (5.17), which is zero at $\mathbf{r}_{\mathrm{z}}$, can be calculated.

Chapter 6

Controlling dark spots

Neither a paraxial nor non-paraxial time-fixed dark spot is topologically protected and it is due to its instability that permanent pockets of pitch dark are not normally found in the wild. Zeros in two or three electric phasor components, which satisfy at least four scalar conditions, must be created artificially because three spatial dimensions do not provide enough scope to spontaneously proffer a co-ordinate where all necessary conditions are met at the same time. Though the reader might be very familiar with vector vortex beams (and many other possible examples), no dark-spot-containing field is strictly ordinary and often has a certain amount of spatial symmetry that makes it possible for the dark spot to exist.

The question of how we can make a dark spot appear at its most basic level is clearly very important, not only for experimental measurement but also in the interest of theory, to confirm or discover their general properties and impact on the surrounding polarisation structure. Recent work [13, 117, 132] has attempted to address this problem, as has our own proposed technique [133] which is the main focus of this chapter. What any technique for creating dark spots must do is add

more, controllable degrees of freedom to a light field, extra parameters engaged in producing the field which can be subsequently changed to tune the electric field phasor at a chosen position.

A group at Harvard University successfully achieved this in one way using a metasurface specially designed to sculpt non-paraxial fields [13, 117, 132]. The metasurface is divided into pixels which each contain an array of nanostructures whose dimensions can be tailored pixel-by-pixel using an optimisation technique, garnering an enormous number of degrees of freedom (DOFs). By designing the metasurface to maximise the local phase gradient of the field at a desired position the intensity is automatically suppressed and a zero is created and ensured to be well-confined (the field intensity grows quickly when moving away from the zero) after illuminating the metasurface. Having a surplus of DOFs means one can target the phase gradient in multiple locations [132] or even across entire 2D surfaces [13].

We proposed a dark-spot-making technique through modulating the polarisation and relative phase of incident plane waves using a minimum number of DOFs, hinging on the linear relationship between the polarisation of illumination and the field components a given point in space. Though this scheme is relatively simplistic it has some clear advantages in theoretical modelling and the possibility to move the zero around in real time—something which has not yet been demonstrated using a metasurface custom-designed to construct a dark spot at an exact location in a non-evolving field. In the following sections we outline basic theory supported by analytical and numerical simulations, with discussion on experimental challenges and possible applications of the technique.

6.1 Making a dark spot using plane waves

A recurring notion in this thesis is that a number of real mathematical conditions, larger than the number of spatial dimensions, must be met so that a dark spot appears somewhere in real space. In this chapter we will be concerned with a non-paraxial 3D dark spot satisfying $\mathbf{E}(\mathbf{r}_\mathrm{z}) = \mathbf{0}$, that is $E_x = E_y = E_z = 0$ in the complex phasor, and therefore imposing a total of six real constraints, one per real and imaginary part of three complex components, on the electric field at the zero's position $\mathbf{r}_\mathrm{z}$. Crucially, though, we will now be *choosing* where the zero emerges, selecting and fixing its (x, y, z) co-ordinates and losing the ability to spend spatial DOFs on the six conditions $\mathbf{E} = \mathbf{0}$. All necessary DOFs will be instead obtained from the polarisation components of interfering plane waves. One plane wave's electric field phasor can be expressed simply as,

$$\mathbf{E}_\mathrm{pw}(\mathbf{r}) = (a\hat{\mathbf{e}}_a + b\hat{\mathbf{e}}_b)\,\mathrm{e}^{i\mathbf{k}_\mathrm{pw}\cdot\mathbf{r}}, \tag{6.1}$$

where a and b are complex amplitudes, offering two real DOFs each, and $\hat{\mathbf{e}}_{a,b}$ are unit vectors orthogonal to each other and the wavevector $\mathbf{k}_\mathrm{pw}$. A single plane wave, then, returns four real DOFs: two from the location of the wave's polarisation on the Poincaré sphere, and one each from the external amplitude ratio and relative phase between the plane wave and other interfering fields (identically, one DOF from each of $\Re\{a\}$, $\Im\{a\}$, $\Re\{b\}$, $\Im\{b\}$). If we have control of the polarisation and relative phase of two plane waves, we have enough DOFs at our disposal to force the incident field $\mathbf{E}_\mathrm{inc}(\mathbf{r}_\mathrm{z}) = \mathbf{0}$ at some position $\mathbf{r}_\mathrm{z}$. Though two plane waves may at first glance appear to offer eight real DOFs, only six are actually tangible because two DOFs are carried mutually by both plane waves (these DOFs are the plane waves' relative

phase and amplitude. Of the eight apparent DOFs, two are lost because the plane waves can be globally multiplied by a complex number to scale their amplitudes or change their phases by the same amount without disturbing a zero at $\mathbf{r}_\mathrm{z}$). Still, six DOFs are sufficient to meet six real scalar conditions.

Happily in the interference of two plane waves (or any number of plane waves for that matter), the linearity of Maxwell's equations gives four terms in the total field phasor at $\mathbf{r}_\mathrm{z}$ that are individually proportional to one of a and b of Eq. (6.1), or one of the component amplitudes of the second plane wave c and d. Mathematically we have at $\mathbf{r}_\mathrm{z}$,

$$\mathbf{E}_\mathrm{inc}(\mathbf{r}_\mathrm{z}) = \underbrace{a\hat{\mathbf{e}}_a \mathrm{e}^{i\mathbf{k}_1\cdot\mathbf{r}_\mathrm{z}} + b\hat{\mathbf{e}}_b \mathrm{e}^{i\mathbf{k}_1\cdot\mathbf{r}_\mathrm{z}}}_{\mathbf{E}_1(\mathbf{r})} + \underbrace{c\hat{\mathbf{e}}_c \mathrm{e}^{i\mathbf{k}_2\cdot\mathbf{r}_\mathrm{z}} + d\hat{\mathbf{e}}_d \mathrm{e}^{i\mathbf{k}_2\cdot\mathbf{r}_\mathrm{z}}}_{\mathbf{E}_2(\mathbf{r})}. \tag{6.2}$$

where we have adopted subscripts $_1$ and $_2$ to distinguish the different wavevectors of plane wave 1 and 2 (meanwhile the transversality condition is also satisfied by plane wave 2 in $\hat{\mathbf{e}}_c \cdot \hat{\mathbf{e}}_d = 0, \hat{\mathbf{e}}_c \cdot \mathbf{k}_2 = 0, \hat{\mathbf{e}}_d \cdot \mathbf{k}_2 = 0$). Equation (6.2)'s form, though non-threatening, turns out to be rather powerful as the proportionality of the terms of $\mathbf{E}_\mathrm{inc}$ to a, b, c, d is preserved even when introducing matter to the two-wave interference [we shall see this later in Eq. (6.5)]. To create a dark spot at $\mathbf{r}_\mathrm{z}$ we solve what in Eq. (6.2) is a linear system of three complex scalar equations in four complex variables a, b, c, d after setting $\mathbf{E}_\mathrm{inc}(\mathbf{r}_\mathrm{z}) = \mathbf{0}$ (equivalent to finding the nullspace of Eq. (6.2)'s coefficient matrix). Then, polarising the two plane waves according to the solution of $\mathbf{E}_\mathrm{inc}(\mathbf{r}_\mathrm{z}) = \mathbf{0}$ (assigning a, b, c, d their solved-for values) the dark spot is realised at position $\mathbf{r}_\mathrm{z}$. One might alternatively construct and solve a linear system of six real scalar equations by segregating the real and imaginary parts of $\mathbf{E}$ and a, b, c, d—in either case, to solve a real or complex linear system of equations is rudimentary for a language like *MATLAB*. Note that we have placed no restrictions

on the wavevector of either plane wave besides that they do not point in the same direction, $\mathbf{k}_1 \neq \mathbf{k}_2$, otherwise Eq. (6.2) is not monochromatic two-plane-wave interference (as in every chapter in this thesis, we have limited the plane waves to having the same wavenumber, $\sqrt{\mathbf{k}_1 \cdot \mathbf{k}_1} = \sqrt{\mathbf{k}_2 \cdot \mathbf{k}_2}$, so that the resulting superposition is time-harmonic and can contain time-fixed nodes when the electric field phasor is zero).

There are some immediate issues stemming from the low spatial complexity of two-plane wave interference. Any zero we successfully induce, while in one sense three-dimensional by having suppressed all three field components, is in fact only one-dimensional in confinement, residing in a planar node of the interference standing wave. Although planar standing wave nodes are sometimes desirable, our goal is to create a fully localised, point-like dark spot and there is more than one way to accomplish this. Perhaps the two most obvious are either to add more plane waves or to introduce a scatterer.

6.1.1 Adding more plane waves

Interference of N plane waves sets up a summation of plane wave fields evaluated at $\mathbf{r}_\mathrm{z}$ over the index j,

$$\mathbf{E}_\mathrm{inc}(\mathbf{r}_\mathrm{z}) = \sum_{j=1}^{j=N} \left(x_{2j-1}\hat{\mathbf{e}}_{2j-1} + x_{2j}\hat{\mathbf{e}}_{2j}\right) \mathrm{e}^{i\mathbf{k}_j \cdot \mathbf{r}_\mathrm{z}}, \tag{6.3}$$

which is a linear system of three complex scalar equations in $2N$ complex variables. With a large number of plane waves we have a significant surplus of DOFs that can be used to impose more conditions on the total field $\mathbf{E}$, such as creating more than one dark spot simultaneously, suppressing the field derivatives or maximising the

field phase gradient (this would require an optimisation process because the field's local phase gradient is not linear with respect to the variables $x_{1,2,\ldots,2N}$).

Point-like dark spots can be produced in the interference if $N \geq 4$ assuming that $\mathbf{k}_j$ are chosen randomly (once chosen, the basis vectors $\hat{\mathbf{e}}_{2j-1}$ and $\hat{\mathbf{e}}_{2j}$ can be chosen and the complex amplitudes x_{2j-1} and x_{2j} found). This assumption of randomness avoids symmetric wavevectors which impact the dimension of the zero, for example if for all j, each of $\mathbf{k}_j$ lies in the same plane then the resulting interference is only two-dimensional, being uniform in the direction orthogonal to the common wavevector plane (zeros become line-like structures). Likewise randomness ensures that the polarisation components of all plane waves are able to engage and interfere with each other and avoid non-interfering plane wave superpositions [134]. A three-dimensionally confined dark spot generated in the interference of plane waves with random wavevectors is most useful in a theoretical context and was critical in our in-depth study of non-paraxial zeros in chapter 5. To use randomly generated wavevectors is to set up the most generic and asymmetric environment in which to create the zero, allowing its basic features to be probed such as the intersecting polarisation singularities we learned in chapter 5 (of course, the combined field is not totally random because the plane waves are polarised specially to force a zero to exist). Equally, semi-random or fully random plane wave interference helps to discover, confirm or debunk topological properties like singularity indices or, in a prelude to some of the findings in the next chapter, geometrical links between fundamental vector quantities in light. Primarily the need to precisely control the relative phase of many interfering fields would, unfortunately, make recreating this method of making dark spots very difficult experimentally since each field must be derived from the same laser so that their relative phases can be defined. It is experimentally more promising to return to two-plane-wave interference while introducing a scattering

particle.

6.1.2 Adding a particle in two-plane-wave interference

In the search for experimental viability of our dark-spot-making method we will now revert back to the interference of two plane waves that, this time, interact with matter. Matter, responding to excitation and radiating its own field, establishes a near field region which is non-paraxial and can accommodate three-dimensionally confined, three-component zeros. This way we can passively inject structure to our original two-plane wave standing wave and realise suitable dark spots using a minimum number of DOFs. Equation (6.2) can actually be generalised to incorporate particles amid the interference. Consider a particle with arbitrary geometry and unspecified material illuminated by two plane waves like in Fig. (6.1). Recall from Eq. (6.2) that the two plane waves both have two complex components a, b and c, d in the direction of the basis vectors $\hat{\mathbf{e}}_{a,b}$ and $\hat{\mathbf{e}}_{c,d}$ respectively; the particle scatters power supplied by each polarisation component differently. Assume, for instance, that the $\hat{\mathbf{e}}_a$ component of plane wave 1 has unit amplitude ($a = 1$): depending on its geometry and material the particle is excited and radiates a field $\mathbf{E}_a^{\text{scat}}$ that sums with plane wave 1's unit amplitude $\hat{\mathbf{e}}_a$ component to give a total interaction field $\mathbf{E}_a$

$$\mathbf{E}_a(\mathbf{r}) = \mathbf{E}_a^{\text{scat}}(\mathbf{r}) + \hat{\mathbf{e}}_a \mathrm{e}^{i\mathbf{k}_1 \cdot \mathbf{r}}. \tag{6.4}$$

What is significant about Eq. (6.4) is that because of Maxwell's equations' linearity the total interaction field *scales linearly* with the $\hat{\mathbf{e}}_a$ component amplitude, that is, if plane wave 1's $\hat{\mathbf{e}}_a$ component has amplitude a, then the total interaction field is $a\mathbf{E}_a$. Likewise should we instead illuminate the particle with a different plane wave component, say the $\hat{\mathbf{e}}_c$ component of plane wave 2, a different interaction field $c\mathbf{E}_c$ is

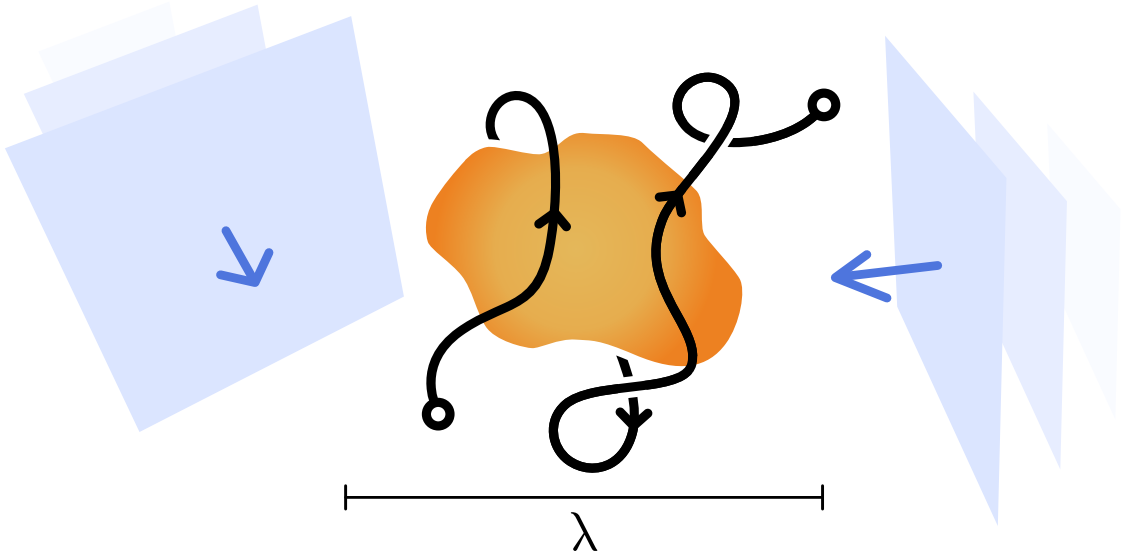

Figure 6.1: The dark spot position control concept. By controlling the polarisation and relative phase and amplitude of two plane waves it is possible to enforce the conditions $\mathbf{E}(\mathbf{r}_z) = \mathbf{0}$ at any desired position $\mathbf{r}_z$. By introducing a particle with arbitrary geometry, a 3D near field is established after excitation by the plane waves which enables 3D-confined, point-like dark spots to be created. Smoothly tuning the complex component amplitudes of the two plane waves allows the dark spot to move along a desired trajectory.

developed and thus, if we immerse the particle in the entire incident two-plane-wave interference Eq. (6.2), the total field $\mathbf{E}$ is simply,

$$\mathbf{E}(\mathbf{r}) = a\mathbf{E}_a(\mathbf{r}) + b\mathbf{E}_b(\mathbf{r}) + c\mathbf{E}_c(\mathbf{r}) + d\mathbf{E}_d(\mathbf{r}). \tag{6.5}$$

Once more, we have obtained a linear system of three complex scalar equations (one per component) in the complex amplitudes a, b, c, d, though the vector fields $\mathbf{E}_{a,b,c,d}$ are considerably more complicated than the plane wave components of Eq. (6.2). Again, by controlling the two plane waves' polarisation and relative phase with one another, point-like dark spots can be enforced in the particle's near field but it is worth noting that no manipulation of the particle is required (the particle only serves as a means to disrupt the two-plane-wave interference and establish a non-paraxial

field). However, the interaction fields $\mathbf{E}_{a,b,c,d}$ depend on the particle properties and must be known if we wish to solve $\mathbf{E}(\mathbf{r}_z) = \mathbf{0}$ at a position $\mathbf{r}_z$. They may be found analytically for simple particles (e.g., small dipolar particles) or can be found by numerical simulation for more complex geometries as we shall soon demonstrate.

It is important to remark on how the properties of the particle can affect the quality of any dark spot that can be created in its near field. For well-confined dark spots the field scattered by the particle must be sufficiently strong so as not to be dominated by the two-plane-wave incident field, which is only capable of making planar zeros. Two factors that determine the particle's scattering strength are its nearness to a resonance at the chosen wavelength and size (the particle in Fig. 6.1 was labelled as being large compared to the incident wavelength for this reason). Additionally if the particle is too small compared to the incident wavelength it can occupy a node of the two-plane-wave interference such that, for some dark spot positions $\mathbf{r}_z$, the particle is not excited and the zero loses its 3D confinement, exploding into a dark plane. A dark spot's quality of confinement—specifically how sharply the field intensity rises out of $\mathbf{r}_z$—is also position-dependent, in that zeros created nearer to the particle where its near field is much stronger compared to the incident field are normally more point-like. An assessment can be made using the field Jacobian matrix as we show next.

6.1.3 Dark spot confinement

Confinement of a point-like zero can be characterised by the first-order field derivatives contained in the electric field Jacobian matrix, evaluated at $\mathbf{r}_z$. The Jacobian matrix $\mathbf{J}$ is a powerful recurring concept in this thesis that captures the immediate behaviour of the electric field at a given point since $\mathbf{E}$, smoothly varying, appears

linear over small distances,

$$\mathbf{J} = \begin{pmatrix} \frac{\partial E_x}{\partial x} & \frac{\partial E_x}{\partial y} & \frac{\partial E_x}{\partial z} \\ \frac{\partial E_y}{\partial x} & \frac{\partial E_y}{\partial y} & \frac{\partial E_y}{\partial z} \\ \frac{\partial E_z}{\partial x} & \frac{\partial E_z}{\partial y} & \frac{\partial E_z}{\partial z} \end{pmatrix}. \tag{6.6}$$

Using a first-order approximation of $\mathbf{E}$ near to a dark spot at position $\mathbf{r}_z$ the electric field intensity is a quadratic function of space that can be written in matrix representation,

$$\mathbf{E}^* \cdot \mathbf{E} \approx \mathbf{v}^T \Re\{\mathbf{J}^T \mathbf{J}^*\} \mathbf{v}, \tag{6.7}$$

where $\mathbf{v} = \mathbf{r} - \mathbf{r}_z$. Since intensity is an always real, always positive quantity, the quadratic equation of space Eq. (6.7) increases on every outward direction from the dark spot which, therefore, has an ellipsoidal shape (the dark spot, at zero intensity, is enclosed by ellipsoidal surfaces of constant intensity). The three semi-axes $d_{1,2,3}$ of the ellipsoid defined by an iso-intensity surface of value δ are related to the eigenvalues $e_{1,2,3}$ of the 3×3 positive-definite matrix $\Re\{\mathbf{J}^T \mathbf{J}^*\}$ in the following way,

$$d_i = \sqrt{\frac{\delta}{e_i}} \tag{6.8}$$

Since the determinant of a matrix is equal to the product of its eigenvalues, $\det \Re\{\mathbf{J}^T \mathbf{J}^*\} = e_1 e_2 e_3$ provides a measure of the confinement of the dark spot (a larger value means an overall smaller ellipsoid in Eq. (6.7) and hence better confinement).

6.2 Moving dark spot examples

With our proposed methodology point-like dark spots can be made in any location near to a particle under illumination by two plane waves, and to change the dark spot's position, we need only adjust the polarisation and relative phase between the plane waves. By smoothly modulating polarisation it is possible to send a dark spot along a chosen trajectory—no modifications to the particle or plane wave wavevectors are necessary. In this section we will provide two examples demonstrating how dark spots can be created and moved in any desired path around particles with arbitrary geometry using numerical simulations.

In practice as polarisation is tuned to change the dark spot's position, there is a certain delay before the desired interference field, including the newly positioned dark spot, is set up as the re-polarised plane waves propagate across the particle before being scattered. This propagation delay is so far not accounted for by our equations which are time-harmonic but we can provide a simple proof-of-concept in Fig. 6.2, where a dark spot is moved in a circular path in the yz plane around a doughnut-shaped particle. We assume in this example that as the two plane waves' polarisations are varied the field changes instantaneously throughout the whole of space which is, of course, not physical especially because the particle and surrounding space plotted in Fig. 6.2(a) is larger than the incident wavelength as indicated. However as we will show in the next subsection, as long as the dark spot moves 'relatively slowly' (in our second example it completes its path in about 500 fs) the penalty of this assumption in the dark spot's sharpness is manageable.

The silver torus particle (its perimittivity obtained at the incident wavelength using Palik [135]) in Fig. 6.2(a) is illuminated at $\lambda = 800\,\text{nm}$ by two plane waves with wavevectors $\mathbf{k}_1 = k(\sqrt{3}/2\,\hat{\mathbf{y}} + 1/2\,\hat{\mathbf{z}})$ and $\mathbf{k}_2 = k(\sqrt{2/7}\,\hat{\mathbf{x}} + 1/\sqrt{7}\,\hat{\mathbf{y}} - 1/\sqrt{7}\,\hat{\mathbf{z}})$,

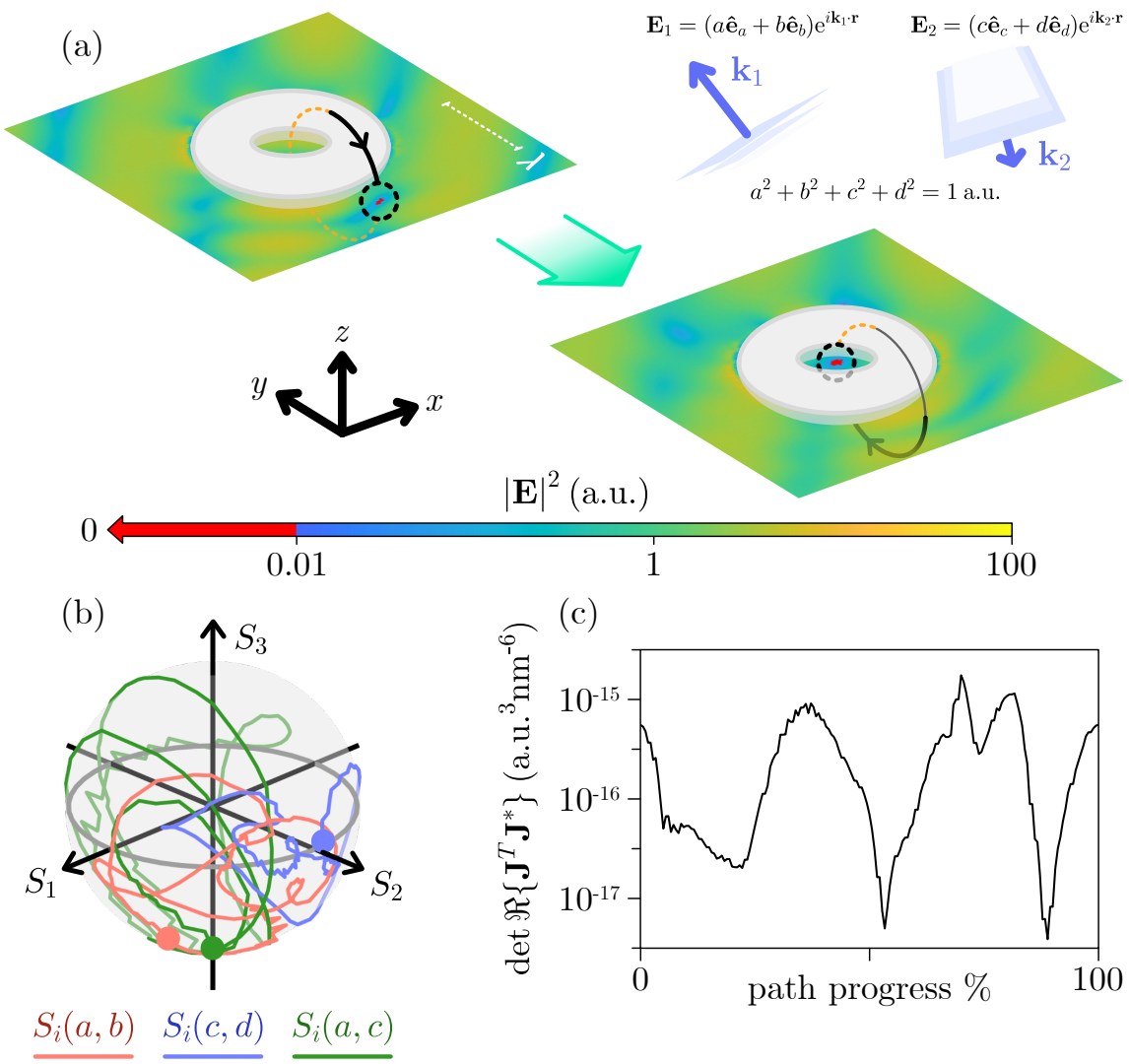

Figure 6.2: Position control of a dark spot using two plane waves and a nanoparticle, in this case a silver torus illuminated at $\lambda = 800$ nm. By controlling the complex degrees of two plane waves (variables a, b, c, d) in (a), a dark spot is moved in a circular path around and threading the torus (two snapshots are provided, where the field intensity is plotted. Note that $a^2 + b^2 + c^2 + d^2 = 1$ a.u.). Below 0.01 a.u. the colour saturates in red to highlight the dark spot position. In moving the dark spot, the required change in polarisation and relative phase of the two plane waves can be encoded on the Poincaré as in (b) (red line corresponds to $\mathbf{E}_1$, blue to $\mathbf{E}_2$, and green to the plane waves' relative phase on a superimposed Bloch sphere. All three lines begin and end in the same place—the solid circle). Confinement of the dark spot over the course of its journey is characterised in (c).

and with amplitudes a, b and c, d as labeled which are gradually changed to move the dark spot from its starting point (the top of the circle) anticlockwise with respect to the yz plane, threading the torus before returning to its initial position. On a xy cut plane the total electric field intensity $|\mathbf{E}|^2$ is plotted in arbitrary units where 1 a.u. is equal to the incident field intensity at the origin ($a^2 + b^2 + c^2 + d^2 = 1$ a.u.). Below 0.01 a.u. the colour is saturated red to highlight the dark spot's location. Meanwhile in Fig. 6.2(b), traces of the polarisation of the two plane waves are plotted on the Poincaré sphere as they are modulated as the dark spot progresses along the circular path, with the red line corresponding to plane wave 1's amplitudes (a, b) and the blue line to the second plane wave's (c, d) component amplitudes (since the dark spot returns to its starting position, all traces begin and end in the same place indicated by the solid circle). A third, green trace accounts for the relationship between the two plane waves by calculating the Stokes parameters using the amplitudes a and c. We should not understate the importance of the green trace as it represents the precise control of the relative amplitude and phase of the two waves which could be challenging to implement experimentally (the waves must be coherent). While the two plane waves have 3D orientation meaning the azimuth position (with respect to the S_3 axis) of each trace on the Poincaré sphere is arbitrary, dependent on the choice of basis vectors for each plane wave, what Fig. 6.2(b) demonstrates is that the dark spot's path is fully encoded in polarisation by three, 1D closed curves in Stokes space relative to each plane wave's plane of polarisation. Finally in Fig 6.2(c) the quantity $\det \Re\{\mathbf{J}^T \mathbf{J}^*\}$, which is related to the volume of the ellipsoidal shape of the dark spot defined at a fixed intensity value, is plotted as a measure of confinement of the dark spot as it follows the circular trajectory. The dark spot's size varies as it moves around the doughnut particle, through regions where the particle's scattered field would be naturally larger and able to dominate the incident field, and vice

versa. A larger value of $\det \Re\{\mathbf{J}^T\mathbf{J}^*\}$ corresponds to a relatively smaller dark spot. The singular nature of the dark spot, being an exact zero in the electric field, means its *absolute* size is difficult to quantify, certainly compared to measuring the size of a local maximum for example. Knowing that the incident field in Fig. 6.2 has an intensity of 1 a.u. at $\mathbf{r} = \mathbf{0}$ we can select a small total field intensity near to the dark spot, say 0.01 a.u. as highlighted red in Fig. 6.2(a), and use Eq. (6.8) with $\delta = 0.01$ to calculate the zero's ellipsoid volume. In Fig. 6.2(c) the largest and smallest values of $\det \Re\{\mathbf{J}^T\mathbf{J}^*\}$ are 1.75×10^{-15} a.u.^{3}nm^{-6} and 3.89×10^{-18} a.u.^{3}nm^{-6} leading to ellipsoid volumes of $1.00 \times 10^5\,\mathrm{nm}^3$ and $2.12 \times 10^6\,\mathrm{nm}^3$ at $\delta = 0.01$ a.u.. For reference spheres of these volumes have radii of $28.8\,\mathrm{nm} \approx 0.04\lambda$ and $79.7\,\mathrm{nm} \approx 0.1\lambda$ (though in reality the dark spot's ellipsoid semi-axes are not always similar in length).

6.2.1 Using pulses

In a more realistic scenario a dark spot could be sent along an arbitrary trajectory by designing four time-varying pulses (one per polarisation DOF) with the required amplitude and phase modulation at each instant calculated in a time-harmonic approximation, which when simultaneously incident on a particle, realise an approximately zero-intensity dark spot. We demonstrate this in Fig. 6.3, where instead a dark spot moves in a circular path that intersects with a cylindrical nanoparticle as shown in Fig. 6.3(a) (it is perfectly possible to create dark spots inside particles as internal fields can be calculated in numerical simulations). Once more two plane waves, this time propagating along $\mathbf{k}_1 = k\hat{\mathbf{x}}$ and $\mathbf{k}_2 = k\hat{\mathbf{z}}$ with carrier wavelength $\lambda = 500\,\mathrm{nm}$, deliver pre-encoded pulses shown in Fig. 6.4 that move the dark spot over the course of about 500 fs. While the pulses are calculated using our time-harmonic expressions the field resulting from interaction with the nanocylinder is

calculated in a full time-domain numerical simulation. Three snapshots of the dark spot at the indicated times after the pulses enter the simulation domain are shown in Fig. 6.3(b), plotting the instantaneous electric field magnitude on the xz plane (the plane of the dark spot's trajectory). Although the dark spot is only approximately zero in intensity due to propagation delay, it remains clear amongst the rest of the field in the plotting plane and would be sharper still using pulses with a longer duration (the slower the pulses vary in time relative to the carrier period, the closer we approach the time-harmonic approximation that we used to calculate the necessary pulse modulation).

Each of the four pulses in Fig. 6.4 correspond to the plane wave component amplitudes a, b, c, and d, and would be challenging to implement in an experiment since both the polarisation and amplitude of each plane wave must be modulated within the $\sim 500\,\mathrm{fs}$ pulse duration. But in order to move the dark spot in the time-domain, what is important is that we have access to adjusting four complex DOFs which do not necessarily need to be divided between two plane waves. Four separate, linearly polarised plane waves offer an equally valid method of controlling the dark spot's position via pulses.

6.3 A dark spot as a sensor

Our focus so far on the freedom to move dark spots along arbitrary paths around matter motivates their potential application in these experimental techniques that might benefit from position control of an electric field. But in fact a static dark spot could be equally useful as a probe to sense a particle's properties because of one of the 3D-confined, three-component dark spot's special characteristics, namely that $\mathbf{E} = \mathbf{0}$ is unstable in three spatial dimensions. For reasons discussed earlier

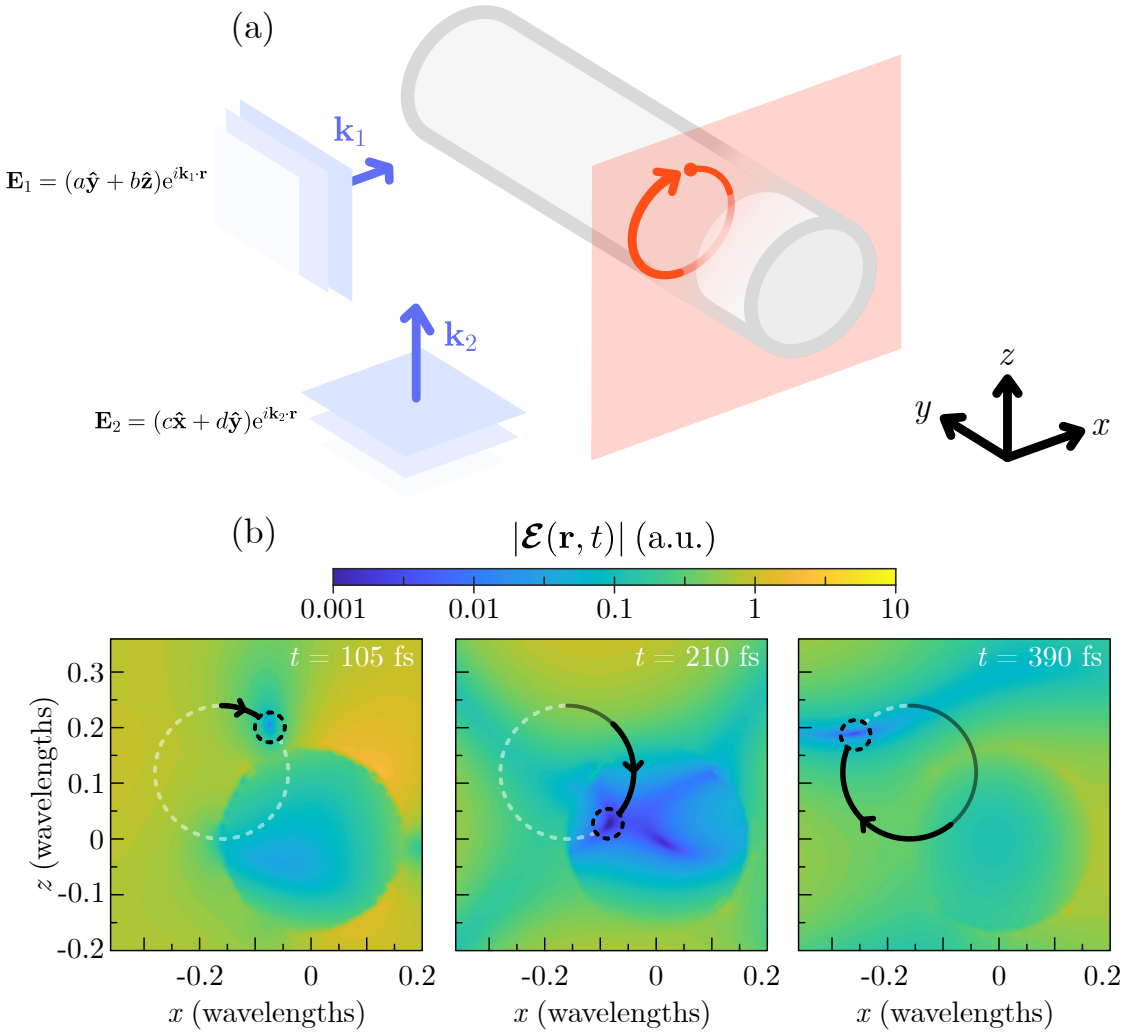

Figure 6.3: Control of a 3D-confined dark spot ($\mathbf{E} = \mathbf{0}$) using four pulses in a time-domain numerical simulation. In (a) is the simulation geometry. Two plane waves with wavevectors $\mathbf{k}_1 = k\hat{\mathbf{x}}$ and $\mathbf{k}_2 = k\hat{\mathbf{z}}$ are incident on a silver nanocylinder (600 nm long, 160 nm diameter) and move a dark spot in a circular, cylinder-intersecting path, by modulation of the plane wave 1's $\hat{\mathbf{y}}$ and $\hat{\mathbf{z}}$ component amplitudes a and b, and the $\hat{\mathbf{x}}$ and $\hat{\mathbf{y}}$ amplitudes c and d of the second plane wave according to the pulse waveforms given in Fig. 6.4. The dark spot completes its trajectory in about 500 fs, the length of the pulses. In (b), three snapshots at indicated times are given of the instantaneous field magnitude in the plane of the dark spot's circular path. Results obtained in numerical simulations using *CST Microwave Studio*.

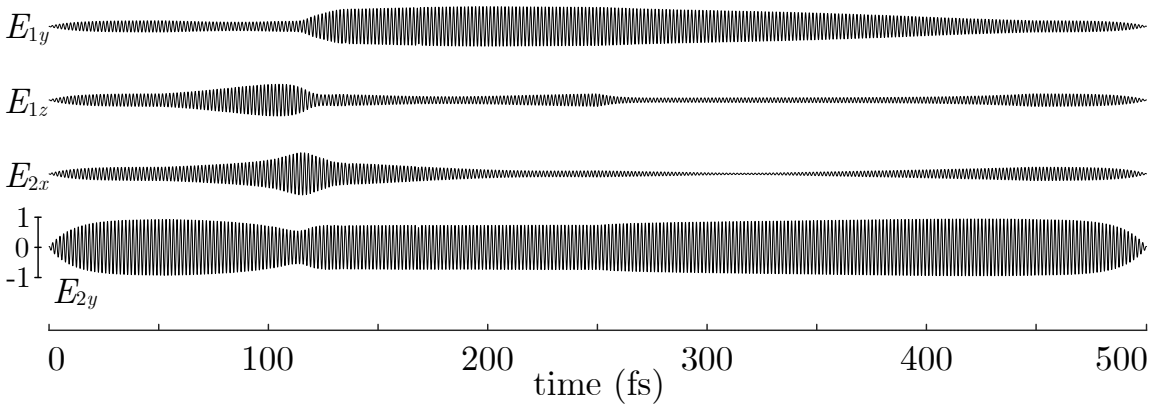

Figure 6.4: Pulse waveforms of a, b, c, and d, the component amplitudes of the two plane waves in Fig. 6.3 that move a dark spot in a circular path around a silver nanocylinder. The combined intensity of the pulses is constant at 1 a.u..

in this chapter's underlying dark-spot-making theory, to create a dark spot in any particle scenario needs prior knowledge of the total electric field that is developed when each plane wave component interacts with the particle, that is, we need to know the fields $\mathbf{E}_{a-d}$ of Eq. (6.5) (these fields were completely different between the doughnut particle and nanocylinder of the last section because of their different geometries and the different plane wave propagation directions). Suppose that we wish to create a zero at position $\mathbf{r}_\mathrm{z}$ near to a particle with geometry A and are able to obtain the fields $\mathbf{E}_{a-d}$ (analytically or by numerical simulations), leading to the required complex amplitudes $a_\mathrm{z}, b_\mathrm{z}, c_\mathrm{z}, d_\mathrm{z}$ that force the dark spot into existence. If, after setting up an experiment, we find that the physical particle differs slightly from the geometry A then after illuminating the particle with polarisations defined by $a_\mathrm{z}, b_\mathrm{z}, c_\mathrm{z}, d_\mathrm{z}$ the intended dark spot will be perturbed, and may not materialise at all if the particle is too different to what was originally expected. This is also true of the particle's material (including permittivity ϵ) and its position or orientation. Though concerning at first glance, the instability of the dark spot with respect to

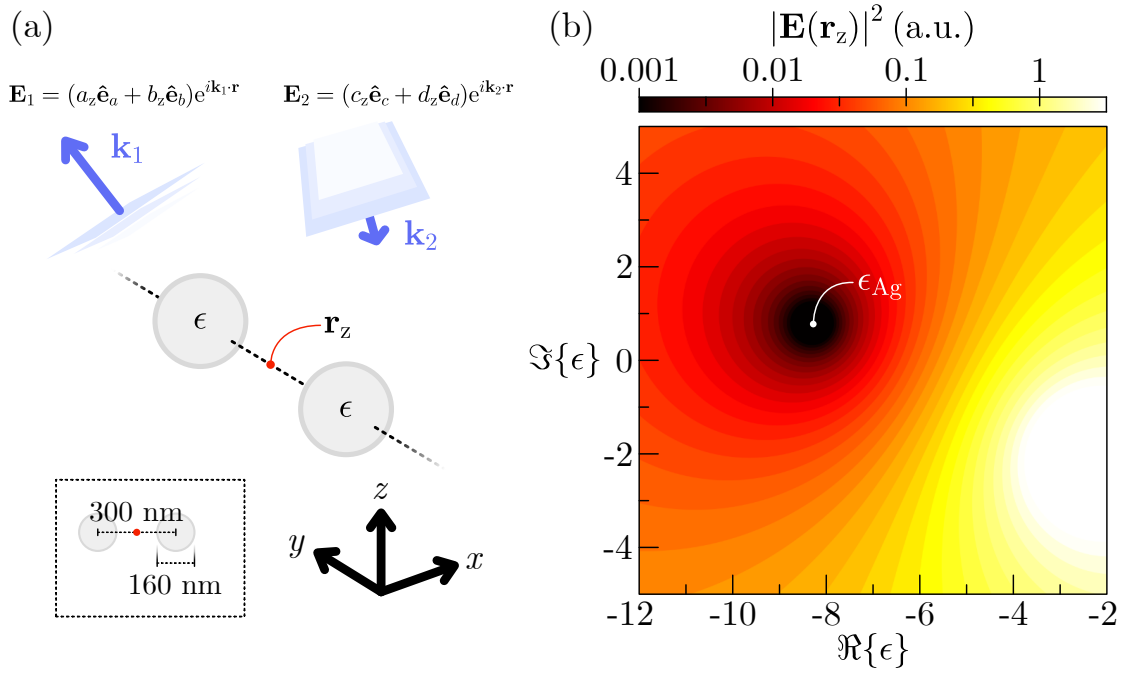

Figure 6.5: A dark spot in the ϵ-space of two spherical particles, modelled as electric dipoles. Subfigure (a) shows the physical system of the two particles (dipoles), separated by 300 nm and both with 160 nm diameter which informs their polarisability. Assuming the particles are silver ($\epsilon = -8.28 + 0.78i$ at $\lambda = 500$ nm), two plane waves with wavevectors $\mathbf{k}_1 = k(\sqrt{3}/2\,\hat{\mathbf{y}} + 1/2\,\hat{\mathbf{z}})$ and $\mathbf{k}_2 = k(\sqrt{2/7}\,\hat{\mathbf{x}} + 1/\sqrt{7}\,\hat{\mathbf{y}} - 1/\sqrt{7}\,\hat{\mathbf{z}})$ are polarised (amplitudes a_z, b_z, c_z, d_z) in such a way as to create a dark spot at $\mathbf{r}_z$ exactly between the particles. Once again the incident field has an intensity of 1 a.u. at the origin. In (b) the electric intensity is probed at $\mathbf{r}_z$ under the same fixed incident field while varying the actual permittivity of the two particles together, producing a plot in complex ϵ space. The dark spot is visible at $\mathbf{r}_z$ when the particle permittivity is the same as what was assumed when polarising the plane waves ($\epsilon = -8.28 + 0.78i$), while disappearing if ϵ differs too much, even becoming a region of enhanced field relative to the incident field for some values of ϵ. Adapted from [133].

the characteristics of the particle could act as a way to sense, for example, the particle's permittivity after a parameter sweep of the plane waves' polarisation states. Permittivity is a complex scalar spanning two real dimensions ($\Re\{\epsilon\}$ and $\Im\{\epsilon\}$)—probing the electric field at a position in space while changing the permittivity of a particle we can produce a plot of $\mathbf{E}$ in 'ϵ-space'.

To see the effect of displacements in ϵ-space of a particle (or particle*s*) on the

exactness of a dark spot we produced an analytical model of two spherical particles, illuminated again by two plane waves with the same $\mathbf{k}$ vectors as in Fig. 6.2. The particles, shown in Fig. 6.5(a), have a 160 nm diameter which is small enough compared to the incident wavelength of 500 nm to be modelled simply as coupled electric dipoles initially excited by the two plane waves, allowing a completely analytical simulation to be set up (we chose not to model a single dipolar scatterer as it is too simple a system to reliably create point-like zeros). The two plane waves are polarised with component amplitudes a_z, b_z, c_z, and d_z to produce a dark spot at a location $\mathbf{r}_z$ in the middle of the 300 nm gap between the particle centres, *assuming* that both particles are silver with $\epsilon = -8.28 + 0.78i$ at $\lambda = 500$ nm [135]. Then, by fixing the polarisation of the two plane waves, a dark spot will only emerge at $\mathbf{r}_z$ if both particles truly have silver's permittivity. In Fig. 6.5(b) the electric field intensity is probed at the single position $\mathbf{r}_z$ while changing only the permittivity of the two particles together, producing a map of $|\mathbf{E}(\mathbf{r}_z)|^2$ in complex ϵ-space. A dark spot exists at $\epsilon = -8.28 + 0.78i$ but grows brighter in intensity if ϵ changes too much [in fact, the electric field at $\mathbf{r}_z$ is enhanced relative to the incident field amplitudes if ϵ strays into the lower-right region of Fig. 6.5(b)]. Last section we showed that by adjusting the complex amplitudes a, b, c, d in Eq. (6.5) a dark spot can be moved along a chosen path in real space near to a particle with fixed ϵ. With identical methodology a dark spot at a target real-space position can be swept across the ϵ-space of a particle of unknown material by modulating two plane waves. To observe the dark spot in real space under a certain incident field indicates that the material properties of the particle assumed by a, b, c, and d correctly match that of the physical particle. Then, the corresponding location of the dark spot in ϵ-space reveals the particle permittivity.

Permittivity is not the only particle property to which a point-like dark spot is

sensitive. If in practice we wish to synthesise a dark spot in some position relative to a particle (like in the last section) then, once polarised appropriately, the phase of the plane waves would need to be tuned until the dark spot materialises since it would be impossible to know the exact location of the particle beforehand. Subsequent real-space displacement of the particle would then destroy the dark spot, certainly in its absolute position, and likely in its relative position to the particle (though re-tuning the phase of the plane waves could recover the zero). In Fig. 6.6 we probe the electric field magnitude in a fixed position $\mathbf{r}'_{\rm z} = \mathbf{r}_{\rm z} + \Delta\mathbf{r}$ relative to a nanocylinder after it is displaced in the xz plane by a vector $\Delta\mathbf{r} = \Delta x\hat{\mathbf{x}} + \Delta z\hat{\mathbf{z}}$, keeping the phase and polarisation of two plane waves (wavevectors $\mathbf{k}_1 = k\hat{\mathbf{x}}$ and $\mathbf{k}_2 = k\hat{\mathbf{z}}$), designed

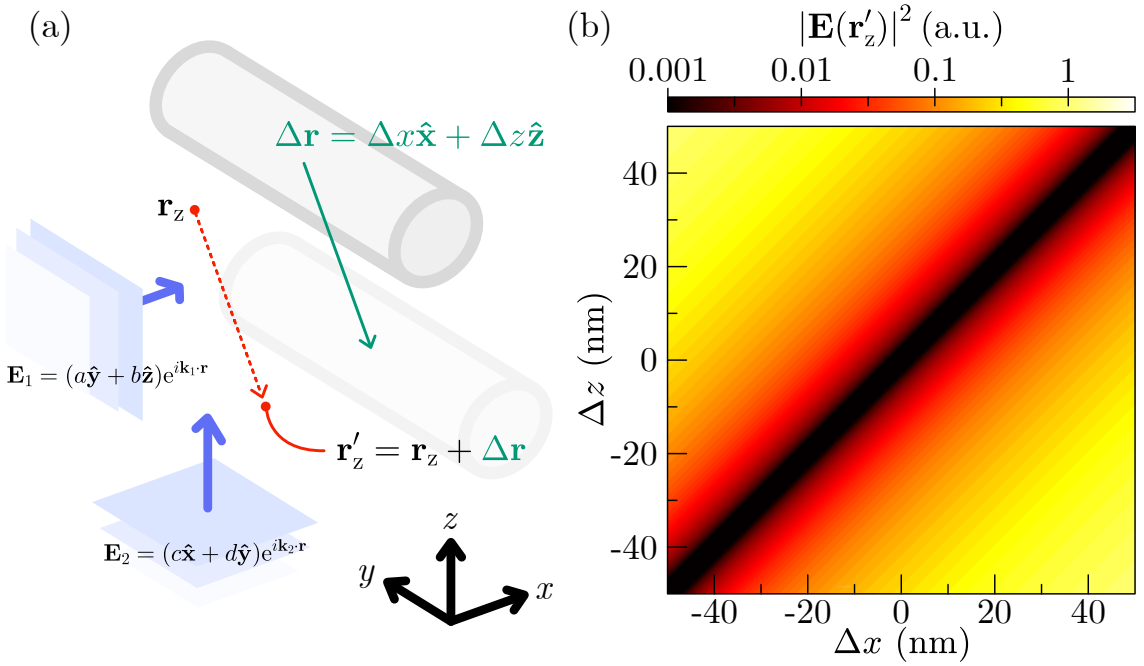

Figure 6.6: Sensitivity of a dark spot created near to a cylindrical nanoparticle after displacement of the nanoparticle along the vector $\Delta\mathbf{r}$ in the xz plane. The dark spot is originally synthesised at position $\mathbf{r}_{\rm z}$ by two plane waves with wavevectors $\mathbf{k}_1 = k\hat{\mathbf{x}}$ and $\mathbf{k}_2 = k\hat{\mathbf{z}}$ with the complex components a, b, c, d that stay fixed. The electric field is measured in the relative position of the dark spot $\mathbf{r}'_{\rm z} = \mathbf{r}_{\rm z} + \Delta\mathbf{r}$ and a $(\Delta x, \Delta z)$-space plot is produced. Adapted from [133].

to create a dark spot at position $\mathbf{r}_z$, constant. Nuances in symmetry of the particle and plane wave arrangement play a significant role in the sensitivity of the dark spot to the particle orientation and position; for instance in Fig. 6.6 the dark spot in its relative position $\mathbf{r}'_z$ is not affected by displacements along the y axis or parallel to the vector $\hat{\mathbf{x}} + \hat{\mathbf{z}}$ due to the plane waves' wavevectors. These have no $\hat{\mathbf{y}}$ components, and are orthogonal such that for displacements $\Delta\mathbf{r}||(\hat{\mathbf{x}} + \hat{\mathbf{z}})$ through the wavefronts of both plane waves an equal increase or decrease in phase is accrued. Considering more than simple translations, on the other hand, should the cylindrical particle rotate about a non-symmetric axis then the plane waves would need to be polarised differently to reconstruct the dark spot. Like its permittivity, a particle's position and even orientation could be sensed by pre-modulating two plane waves' complex component amplitudes and observing (or not observing) a dark spot at an intended location.

6.4 Other applications

We have discussed the possibility of using a dark spot as a sensor for particle permittivity or position but besides this, perhaps the two most plausible fields of study in which a moving point-like zero could be an extremely useful experimental asset are optical microscopy and trapping. Earlier in this thesis we suggested that non-paraxial, point-like dark spots could be used as 3D-confined optical traps for particles in a certain wavelength regime where gradient forces reverse direction. Dark (blue-detuned) trapping [22] has been performed using various dark-spot-containing beams [24, 26] and even optical lattices [27] where traps are 3D-confined. By position-controlling point-like dark spots with our proposed technique it could be possible to move trapped particles precisely in 3D and at relatively high speeds.

Some of the most powerful optical-frequency microscopes use dark spots to break the diffraction barrier and achieve single-nanometre resolutions (well below $\lambda/2$). We mentioned in chapter 1 that, by switching 'on' and 'off' collections of fluorescent particles by shining on them two different-frequency beams (an 'on' beam and an 'off' beam) in sequence, techniques like stimulated-emission-depletion microscopy (STED) [29] can image single particles if the 'off' beam contains a dark spot. This way a particle coinciding with the dark spot escapes being switched off by the second beam. A STED-like methodology could be combined with our point-like dark spot control, supposing that we wished to image something in the near field of an appropriate scatterer. Using two plane waves we could illuminate at an exciting frequency to switch on a group of nearby fluorophores (assuming that intensity is sufficiently high), then illuminate again at a de-exciting frequency while specially polarising the plane waves to synthesise a dark spot at the location of a selected fluorophore, which would remain in the measurable on state. The key advantage of this chapter's proposal is that unlike that of a doughnut beam, our dark spots are point-like and could resolve sub-wavelength detail in three dimensions to offer an alternative mechanism for 3D STED or similar miscroscopy methods. Meanwhile MINFLUX [30], such as it is named, is another microscopy technique that uses a single, position-controlled doughnut beam driven at an exciting frequency to precisely locate, track and image fluorophores while minimising the number of emitted photons. Given that we do not consider the 3D intensity distribution of the field beyond a single position (the dark spot) it would be challenging to minimise photon emission using our methodology. However, it should be possible to use similar post-processing steps (counting emitted photons against the tracked position of the dark spot) to locate and image single particles, again with the advantage of 3D dark spot confinement.

Suitability for these techniques of our controllable dark spots also depends

on the ease with which they can be synthesised experimentally. Since in addition to polarisation, accurate control of the relative phase between the minimum two monochromatic plane waves is crucial to form a dark spot, then experimentally both plane waves must be coherent and derive from the same laser. Whatever the design of the optical set up that has the two plane waves propagating in different directions any delay lines between the plane waves must not exceed the laser's coherence length, and to precisely know the relative phase between the two plane waves at a desired dark spot position will require careful calibration (this also means that, if we wished for more degrees of freedom, it would be difficult to scale up the number of illuminating plane waves).

6.5 Chapter summary

Following two very theory-oriented chapters on electromagnetic dark spots, this chapter has proposed a conceptually simple technique for synthesising dark spots experimentally using a minimum of two plane waves. Our technique hinges on the linearity of Maxwell's equations; that the complex component amplitudes of the two plane waves can be taken as variables in a linear system of equations describing the electric field components at a chosen position $\mathbf{r}_z$. By solving this system of equations evaluated to $\mathbf{E}(\mathbf{r}_z) = \mathbf{0}$ one obtains the plane wave complex amplitudes that force a dark spot into existence at the desired location, and by carefully adjusting these complex amplitudes, the dark spot can be freely moved in space. The low complexity of plane waves and spatial symmetry arguments means that perhaps the best way (i.e., using the minimum number of plane waves) to ensure that synthesised dark spots are point-like is to illuminate a particle which passively sets up a non-paraxial near field. To use our technique in this way requires that the field scattered by the

particle, which can be calculated analytically or in numerical simulations, is known.

The act of engineering the electric field in a subwavelength region near to a particle is one purpose of plasmonic nanoantenna design [136, 137], a field responsible for specially designed nanoparticle geometries (e.g., bowties, dimers) that strongly enhance light intensity in tightly confined pockets called 'hot spots' [138, 139]. Some work has been dedicated to creating the hot spot's opposite, a 'cold spot' [140, 141], near to nanoantennae often showing ways of interchanging the two [142–144], though in this context a 'cold spot' is a relatively loose term that is not intended to mean a region of exactly zero electric field, rather a local minimum. Our original work which inspired the chapter of this thesis was titled, *Creating and moving nanoantenna cold spots anywhere* [133] which does not make immediately obvious that an exactly zero electric field, our 'cold spot', is a singularity with all of the rich topological properties described in chapter 5.

Chapter 7

Re-interpreting spin angular momentum density

Now is this thesis' final chapter which departs somewhat from the specific dark-spot theme of chapters 3, 4 and 5; electromagnetic field zeros though not completely absent playing a much reduced, supporting role. For here our topic is the familiar equation for light's total spin angular momentum density (acronym SAM, as a reminder) first given in chapter 1 [Eq. (2.24)],

$$\mathbf{S} = \frac{1}{4\omega}\Im\{\epsilon_0\mathbf{E}^* \times \mathbf{E} + \mu_0\mathbf{H}^* \times \mathbf{H}\} = \mathbf{S}_\mathrm{e} + \mathbf{S}_\mathrm{m}, \tag{7.1}$$

which is the vector addition of SAM carried by the electric and magnetic field, each of these SAM vectors pointing in the direction of the respective field polarisation ellipse. As the name suggests Eq. (7.1) is an *angular* momentum density expressing, according to the right-hand rule, how and in which direction local rotation of the electric and magnetic field vectors over time could cause matter to experience torque and (importantly) chiral forces (chiral because if, say, in a region of at least elliptical

electric polarisation the electric field's phase increases in the direction of $\mathbf{S}_\mathrm{e}$, then over space the rotating $\boldsymbol{\mathcal{E}}$ field vector creates rotating helical structures, which are chiral [82–84]). Spin AM density is an intrinsic angular momentum which means that if it is non-zero for an electromagnetic field, then no choice of co-ordinate origin can eliminate it, unlike for the extrinsic orbital angular momentum (OAM) density $\mathbf{L} = \mathbf{r} \times \mathbf{p}$ of light that does not contain vortices [34, 54, 61, 62]. This chapter's principle point of discussion is an alternative representation of total spin $\mathbf{S}$, a decomposition of $\mathbf{S}$ into two terms that are not separate electric and magnetic contributions $\mathbf{S}_\mathrm{e} + \mathbf{S}_\mathrm{m}$, rather two vectors $\mathbf{s}_\mathrm{c}$ and $\mathbf{s}_\mathrm{p}$ (to be named later) that as we will discover are related to the linear momentum that can be imparted in a chiral light-matter interaction.

When originally calculating the Jacobian matrix of $\mathbf{S}_\mathrm{e}$ as presented in chapter 5 it was noticed that the total SAM density vector could be recast by substitution of Maxwell's equations for monochromatic waves, with two vector identities, into a different form:

$$\mathbf{S} = \frac{1}{4\omega^2}\Re\{\mathbf{E}^* \cdot (\nabla)\mathbf{H} - \mathbf{H}^* \cdot (\nabla)\mathbf{E}\} + \frac{1}{2\omega^2}\nabla \times \frac{1}{2}\Re\{\mathbf{E}^* \times \mathbf{H}\}. \tag{7.2}$$

What Eq. (7.2) presents is a decomposed version of $\mathbf{S}$, a sum of two vector terms, the first quite obscure and the second immediately recognisable as proportional to the curl of the Poynting vector, $(1/2)\,\Re\{\mathbf{E}^* \times \mathbf{H}\}$. Specifically this spin decomposition is obtained by substituting $\mathbf{E} = i(\omega\epsilon_0)^{-1}\nabla \times \mathbf{H}$ and $\mathbf{H} = -i(\omega\mu_0)^{-1}\nabla \times \mathbf{E}$ for the un-conjugated phasors in the original expression Eq. (7.1), followed by the identities $\mathbf{a}\times(\nabla\times\mathbf{b}) = \mathbf{a}\cdot(\nabla)\mathbf{b} - (\mathbf{a}\cdot\nabla)\mathbf{b}$ and $\nabla\times(\mathbf{a}\times\mathbf{b}) = \mathbf{a}(\nabla\cdot\mathbf{b}) - \mathbf{b}(\nabla\cdot\mathbf{a}) + (\mathbf{b}\cdot\nabla)\mathbf{a} - (\mathbf{a}\cdot\nabla)\mathbf{b}$ and $\nabla\cdot\mathbf{E} = \nabla\cdot\mathbf{H} = 0$ (so the form Eq. (7.2) is only valid in free space). Some fifteen years ago Berry [33] showed that the Poynting vector could be decomposed in 3D in the very same way using Maxwell's equations and vector manipulation. Unlike

the time-averaged Poynting vector, which since Berry's work is widely known to be decomposed in free space monochromatic waves according to,

$$\mathbf{P} = \frac{1}{2}\Re\{\mathbf{E}^* \times \mathbf{H}\} = \frac{c^2}{4\omega}\Im\{\epsilon_0 \mathbf{E}^* \cdot (\nabla)\mathbf{E} + \mu_0 \mathbf{H}^* \cdot (\nabla)\mathbf{H}\} + \frac{c^2}{2}\nabla \times (\mathbf{S}_\mathrm{e} + \mathbf{S}_\mathrm{m}), \quad (7.3)$$

the decomposition of SAM density Eq. (7.2) cannot be expressed by a sum of exclusively electric and magnetic contributions to the two terms—each term contains multiplication (under a vector operation) between the **E** and **H** phasors, while in Eq. (7.3) only **E** multiplies **E** and **H** multiplies **H** (e.g., $\mathbf{E}^* \cdot (\nabla)\mathbf{E}$).

We expect that many readers will recognise Eq. (7.3), but very few (if any) will have seen the alternative form of spin Eq. (7.2). This is not to say that the core relation in Eq. (7.2) is not at all known. Bliokh et. al [53] understood the coupling between chiral momentum (the first term of Eq. (7.2), $(1/4\omega^2)\Re\{\mathbf{E}^* \cdot (\nabla)\mathbf{H} - \mathbf{H}^* \cdot (\nabla)\mathbf{E}\}$, up to a prefactor converting to units of linear momentum density) and **S** and the curl of the Poynting vector by calculating the force exerted on a dipole *directly* by a field in a chiral interaction. Despite this the authors did not appear to explore the relation further, nor provide any deeper physical significance. More recently, meanwhile, Shi et. al [145] without arriving at Eq. (7.2) uncovered the proportionality between the helicity-independent transverse spin of a linearly polarised evanescent wave and the curl of the Poynting vector, term two of Eq. (7.2), before proposing a rather tenuously linked set of Maxwell-esque spin-momentum equations. Scrutinising some of these claims Bekshaev [146] demonstrated that transverse spin is in general more strongly connected geometrically to the curl of the canonical momentum vector (a part of the Poynting vector), while Shi and co-authors have since further explored the relation between components of total spin and the curl of the Poynting vector [147, 148]. Very recently Golat, a coauthor of our work inspiring this chapter, much

more convincingly formulated four spin-momentum Maxwell-like equations in a quite comprehensive framework that links quadratic quantities in light by representing the electromagnetic bispinor in different bases [37].

Amid sparse coverage of the spin decomposition Eq. (7.2) in the literature we in our publication [31] had two main objectives. First was to clarify the physical significance of the two vectors, particularly in terms of light-matter interactions, and any geometrical significance of the vectors as originally suggested by Shi [145], that the curl of the Poynting vector corresponds to helicity-independent transverse spin. Second was to promote the decomposition's intuitive value and its fitness as a tool to reveal striking hidden features in structured light—one such feature which we identified in the centre of a linearly polarised vortex beam; a thesis-unifying dark spot. The value of the Poynting vector's (kinetic momentum) representation as the sum of orbital and spin currents (canonical and spin momentum) is already clear: not only does it help to visualise light's linear momentum, given that matter responds differently to $\mathbf{p}$ and $\mathbf{p}^{\mathrm{s}}$ which may point in independent directions (such as in evanescent waves), but it even underpins the famous Abraham-Minkowski dilemma [45]. In attempting to achieve these objectives we chose to name the two spin terms of Eq. (7.2) *canonical spin* $\mathbf{s}_{\mathrm{c}}$ and *Poynting spin* $\mathbf{s}_{\mathrm{p}}$ for reasons we shall next address as well as the terms' physical meanings. A depiction of total spin, electric spin, magnetic spin, canonical spin and Poynting spin vectors is given in Fig. 7.1.

7.1 Canonical and Poynting spin

From Eq. (7.2) the canonical spin is defined as

$$\mathbf{s}_{\mathrm{c}} = \frac{1}{4\omega^2}\Re\{\mathbf{E}^* \cdot (\nabla)\mathbf{H} - \mathbf{H}^* \cdot (\nabla)\mathbf{E}\}, \tag{7.4}$$

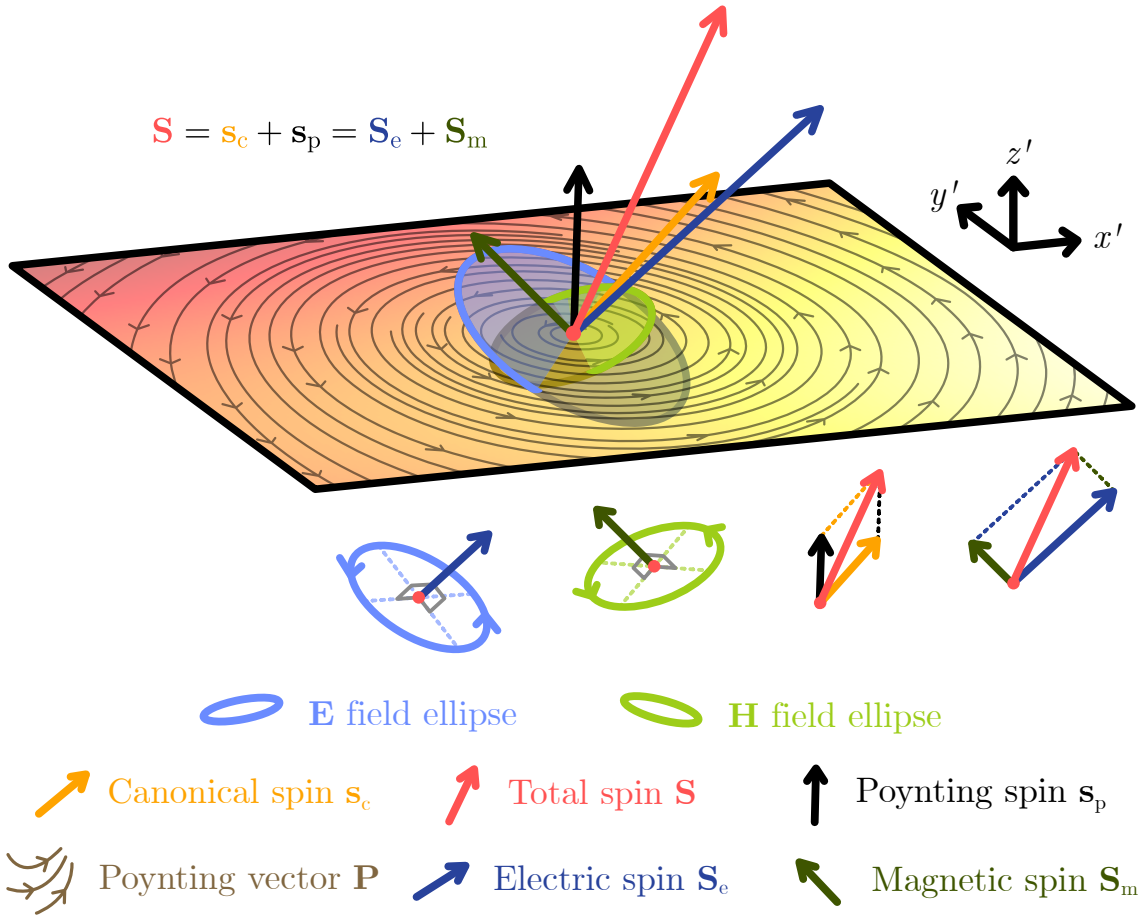

Figure 7.1: Illustration of the geometry of certain vectors with respect to electric and magnetic polarisation in a generic non-paraxial field, developed in random plane wave interference (note that the field is three-dimensional but has been projected into a 2D page and is inevitably distorted). As a visual aid the diagram is oriented specially so that Poynting spin is parallel to the z' axis which, on an $x'y'$ cut plane, reveals some circulation of the Poynting vector streamlines (though the amplitude and 3D variation of $\mathbf{P}$ truly informs the direction of $\mathbf{s}_\mathrm{p}$). Electric (blue) and magnetic (green) polarisation ellipses are drawn along with their normals, the electric and magnetic spin vectors $\mathbf{S}_\mathrm{e}$ and $\mathbf{S}_\mathrm{m}$, being oriented freely in 3D because of the field's non-paraxiality. Total spin is the vector sum of $\mathbf{S}_\mathrm{e}$ and $\mathbf{S}_\mathrm{m}$ and canonical and Poynting spin $\mathbf{s}_\mathrm{c} + \mathbf{s}_\mathrm{p}$ and in this very generic depiction, $\mathbf{s}_\mathrm{c}$ and $\mathbf{s}_\mathrm{p}$ have no geometric relation to polarisation ellipses. Adapted from [31].

and Poynting spin,

$$\mathbf{s}_\mathrm{p} = \frac{1}{2\omega^2}\nabla \times \frac{1}{2}\Re\{\mathbf{E}^* \times \mathbf{H}\}. \tag{7.5}$$

For the avoidance of confusion, any time we in this chapter mention 'canonical spin', we are referring to $\mathbf{s}_\mathrm{c}$ Eq. (7.4), any time we mention 'Poynting spin' we refer to $\mathbf{s}_\mathrm{p}$ Eq. (7.5), and any time we use the term 'total spin' we mean the total SAM density $\mathbf{S}$ Eq. (7.1), equal to the sum of the two terms above $\mathbf{S} = \mathbf{s}_\mathrm{c} + \mathbf{s}_\mathrm{p}$. Upon seeing these expressions for the first time it is virtually impossible to tell which of light's properties canonical spin $\mathbf{s}_\mathrm{c}$ represents while Poynting spin, containing the curl of the Poynting vector, could be viewed as an incorporation of light's OAM into the total spin vector, reflecting how the curl of $\mathbf{S}$ generates spin momentum $\mathbf{p}^\mathrm{s}$ in Eq. (7.3). There are ways to better understand the physical significance of the two terms, particularly by calculation of optical forces on Rayleigh particles.

7.1.1 Chiral force

The beauty of the sum of the two spin terms and the fact that Poynting spin mirrors the role of the curl of the total spin in the Poynting vector $\mathbf{P}$ might suggest that $\mathbf{s}_\mathrm{c}$ and $\mathbf{s}_\mathrm{p}$, their sum $\mathbf{S}$ being an axial vector, are chiral analogies to canonical and spin momenta, a notion which is strongly supported when calculating the total force exerted by light on dipolar particles, a sum of force terms that are each classed either as achiral (felt in the same direction by enantiomers) or chiral (felt in different directions by enantiomers). Ignoring non-reciprocal terms the achiral force exerted

on a particle in the Rayleigh limit (size $<< \lambda$) is given by [43],

$$\begin{aligned}\mathbf{F}_{\text{achiral}} =& \underbrace{\nabla(\Re\{\alpha_{\text{e}}\}W_{\text{e}} + \Re\{\alpha_{\text{m}}\}W_{\text{m}})}_{\text{gradient force}} \\ &+ \underbrace{2\omega\Im\{\alpha_{\text{e}}\}\mathbf{p}_{\text{e}} + 2\omega\Im\{\alpha_{\text{m}}\}\mathbf{p}_{\text{m}}}_{\text{radiation pressure}} \\ &\underbrace{- \frac{k^4}{6\pi c}\left(\Re\{\alpha_{\text{e}}^*\alpha_{\text{m}}\} + |\alpha_{\text{c}}|^2\right)\mathbf{P} + \frac{k^4}{6\pi c}\Im\{\alpha_{\text{e}}^*\alpha_{\text{m}}\}\mathbf{P}_{\text{i}}}_{\text{recoil}},\end{aligned} \tag{7.6}$$

where α_{e}, α_{m} and α_{c} are electric, magnetic and chiral dipole polarisabilities (although the inclusion of $|\alpha_{\text{c}}|^2$ in Eq. (7.6) might be surprising, it—no longer a pseudoscalar due to squaring—accounts for an achiral recoil force term experienced by chiral particles, here grouped into the total achiral force $\mathbf{F}_{\text{achiral}}$), W_{e} and W_{m} are electric and magnetic energy densities, $\mathbf{p}_{\text{e}}$ and $\mathbf{p}_{\text{m}}$ are electric and magnetic contributions to canonical momentum $\mathbf{p} = \mathbf{p}_{\text{e}} + \mathbf{p}_{\text{m}}$, and $\mathbf{P} = (1/2)\Re\{\mathbf{E}^* \times \mathbf{H}\}$ and $\mathbf{P}_{\text{i}} = (1/2)\Im\{\mathbf{E}^* \times \mathbf{H}\}$. In Eq. (7.6) terms are grouped to distinguish gradient forces (related to the field energy density gradient), radiation pressure (a direct interaction between the field and matter) and recoil forces (caused by matter recoiling from its own radiation after excitation). Grouping similarly the terms of the total *chiral* force that can be induced by an electromagnetic field we find that the canonical spin emerges proportional to chiral pressure:

$$\mathbf{F}_{\text{chiral}} = \underbrace{\omega\nabla(\Re\{\alpha_{\text{c}}\}h)}_{\text{helicity gradient}} + \underbrace{2\omega k\Im\{\alpha_{\text{c}}\}\mathbf{s}_{\text{c}}}_{\text{chiral pressure}} \underbrace{- \omega\frac{k^4}{3\pi}(\Re\{\alpha_{\text{e}}^*\alpha_{\text{c}}\}\mathbf{S}_{\text{e}} + \Re\{\alpha_{\text{m}}^*\alpha_{\text{c}}\}\mathbf{S}_{\text{m}})}_{\text{spin recoil}}. \tag{7.7}$$

while the helicity density $h = -\Im\{\mathbf{E}^* \cdot \mathbf{H}\}/(2\omega c)$ is responsible for gradient force [149] and electric and magnetic parts $\mathbf{S}_{\text{e}}$ and $\mathbf{S}_{\text{m}}$ of total spin induce chiral recoil forces.

In fact Eq. (7.7) differentiates between the way that canonical and Poynting spin can communicate with matter because unlike canonical spin, Poynting spin can only couple to relatively weaker recoil forces (compared to radiation pressure). Comparing Eq. (7.6) and Eq. (7.7) we can conclude that for a small particle with non-zero chiral polarisability, canonical spin and Poynting spin couple to forces that are directly analogous to those coupled to by canonical momentum and spin momentum*.

By nature both Eq. (7.6) and Eq. (7.7) have broad scope for manipulation and for this reason the optical force literature tends to write equations inconsistently, sometimes using cross sections σ_*, sometimes polarisabilities α_*, and in many cases using different vectors that do not separate interaction and recoil terms (Golat [43] recently clarified these different force representations). Rarely (if ever besides [53]) is the chiral pressure term in Eq. (7.7) given as a single vector; often instead (for instance [150, 151]) given proportional to the subtraction $\mathbf{S} - \nabla \times \mathbf{P}/(2\omega^2)$. Understanding that there is a fundamental link between spin, the curl of the Poynting vector $\mathbf{s}_\mathrm{p}$ and a third physically meaningful vector $\mathbf{s}_\mathrm{c}$ simplifies matters.

7.1.2 In a helicity basis

To solidify our claim that canonical $\mathbf{s}_\mathrm{c}$ and Poynting spins $\mathbf{s}_\mathrm{p}$ are essentially chiral incarnations of light's orbital and spin currents [33] we can perform what turns out to be a remarkably simple substitution of fields written in a helicity basis. While some core results in this subsection were reported in our original publication [31] our

*We emphasise that Eq. (7.7)is a general expression of chiral force separated into gradient, pressure and recoil terms. While, as we shall see, it is possible for canonical and Poynting spins to be equal and opposite in some specific situations, meaning chiral pressure becomes proportional to $\mathbf{s}_\mathrm{p}$, only canonical spin can be associated generally with chiral pressure, in the same way as canonical momentum is associated with radiation pressure in Eq. (7.6) even though it may be possible circumstantially for canonical and spin momenta to be equal and opposite.

understanding has broadened significantly through recent research [37].

Instead of the traditional electric-magnetic representation of light, a description using an electric field $\mathbf{E}$ and magnetic field $\mathbf{H}$, we may express monochromatic light as a right handed field [comprised of the pair $(\mathbf{E}_\mathrm{R}, \mathbf{H}_\mathrm{R})$] and a left handed field [the pair$(\mathbf{E}_\mathrm{L}, \mathbf{H}_\mathrm{L})$], coupled together by a modified set of Maxwell equations. Within the right and left handed fields the electric and magnetic fields are specially linked via $\mathbf{H}_\mathrm{R}(\mathbf{r}) = (-i/\eta)\mathbf{E}_\mathrm{R}(\mathbf{r})$ and $\mathbf{H}_\mathrm{L}(\mathbf{r}) = (+i/\eta)\mathbf{E}_\mathrm{L}(\mathbf{r})$ [152] where $\eta = \sqrt{\mu_0\epsilon_0}$, a feature arising after applying Faraday's law to the angular spectrum representation of right- and left-circular plane waves:

$$\begin{aligned}\mathbf{E}(\mathbf{r}) =& \iiint \tilde{\mathbf{E}}(\mathbf{k})\mathrm{e}^{i\mathbf{k}\cdot\mathbf{r}}\mathrm{d}^3k \\ =& \iiint [\tilde{E}_\mathrm{R}(\mathbf{k})\hat{\mathbf{e}}_\mathrm{R}(\mathbf{k}) + \tilde{E}_\mathrm{L}(\mathbf{k})\hat{\mathbf{e}}_\mathrm{L}(\mathbf{k})]\mathrm{e}^{i\mathbf{k}\cdot\mathbf{r}}\mathrm{d}^3k \\ =& \mathbf{E}_\mathrm{R}(\mathbf{r}) + \mathbf{E}_\mathrm{L}(\mathbf{r}),\end{aligned} \tag{7.8}$$

$$\begin{aligned}\mathbf{H}(\mathbf{r}) =& \frac{1}{\eta}\iiint \frac{\mathbf{k}}{k} \times \tilde{\mathbf{E}}(\mathbf{k})\mathrm{e}^{i\mathbf{k}\cdot\mathbf{r}}\mathrm{d}^3k \\ =& \frac{1}{\eta}\iiint [-i\tilde{E}_\mathrm{R}(\mathbf{k})\hat{\mathbf{e}}_\mathrm{R}(\mathbf{k}) + i\tilde{E}_\mathrm{L}(\mathbf{k})\hat{\mathbf{e}}_\mathrm{L}(\mathbf{k})]\mathrm{e}^{i\mathbf{k}\cdot\mathbf{r}}\mathrm{d}^3k \\ =& \mathbf{H}_\mathrm{R}(\mathbf{r}) + \mathbf{H}_\mathrm{L}(\mathbf{r}).\end{aligned} \tag{7.9}$$

We have used $(\mathbf{k}/k) \times \hat{\mathbf{e}}_\mathrm{R} = -i\hat{\mathbf{e}}_\mathrm{R}$ and $(\mathbf{k}/k) \times \hat{\mathbf{e}}_\mathrm{L} = +i\hat{\mathbf{e}}_\mathrm{L}$ to obtain Eq. (7.9), with $\hat{\mathbf{e}}_{\mathrm{R/L}}(\mathbf{k})$ representing the right- and left-handed circular basis vectors for a plane wave with wavevector $\mathbf{k}$ (see for example [153]). Note that the relations between $(\mathbf{E}_\mathrm{R}, \mathbf{H}_\mathrm{R})$ and $(\mathbf{E}_\mathrm{L}, \mathbf{H}_\mathrm{L})$ imply that in a pure-helicity field (which is physically realisable) the electric and magnetic field phasors are proportional everywhere in space, sharing the same polarisation structure in agreement with the known fact that C lines of pairs of right and left handed $\mathbf{E}$ and $\mathbf{H}$ fields coincide with each other [154] and

Riemann-Silberstein vortices [155, 156]. Now, to substitute $\mathbf{E} = \mathbf{E}_\mathrm{R} + \mathbf{E}_\mathrm{L}$ and $\mathbf{H} = -i\left(\mathbf{E}_\mathrm{R} - \mathbf{E}_\mathrm{L}\right)/\eta$ into a certain quantity is to separate that quantity into right- and left- handed photon contributions. Doing this for the dual canonical momentum density, for example, reads [128]

$$\begin{aligned}
\mathbf{p} &= \frac{1}{4\omega}\Im\{\epsilon_0\mathbf{E}^*\cdot(\nabla)\mathbf{E} + \mu_0\mathbf{H}^*\cdot(\nabla)\mathbf{H}\} \\
&= \frac{1}{4\omega}\Im\{\epsilon_0[\mathbf{E}_\mathrm{R}^* + \mathbf{E}_\mathrm{L}^*]\cdot(\nabla)[\mathbf{E}_\mathrm{R} + \mathbf{E}_\mathrm{L}] + \frac{\mu_0}{\eta^2}[i\mathbf{E}_\mathrm{R}^* - i\mathbf{E}_\mathrm{L}^*]\cdot(\nabla)[-i\mathbf{E}_\mathrm{R} + i\mathbf{E}_\mathrm{L}]\} \\
&= \frac{\epsilon_0}{2\omega}\Im\{\mathbf{E}_\mathrm{R}^*\cdot(\nabla)\mathbf{E}_\mathrm{R} + \mathbf{E}_\mathrm{L}^*\cdot(\nabla)\mathbf{E}_\mathrm{L}\} \\
&= \mathbf{p}_\mathrm{R} + \mathbf{p}_\mathrm{L}.
\end{aligned} \tag{7.10}$$

With similar algebra we can simplify the same substitution made in the definitions of spin momentum, canonical spin and Poynting spin, and find striking connections between them,

$$\mathbf{p}^\mathrm{s} = \mathbf{p}_\mathrm{R}^\mathrm{s} + \mathbf{p}_\mathrm{L}^\mathrm{s}, \tag{7.11}$$

$$\mathbf{s}_\mathrm{c} = \frac{1}{k}(\mathbf{p}_\mathrm{R} - \mathbf{p}_\mathrm{L}), \tag{7.12}$$

$$\mathbf{s}_\mathrm{p} = \frac{1}{k}(\mathbf{p}_\mathrm{R}^\mathrm{s} - \mathbf{p}_\mathrm{L}^\mathrm{s}). \tag{7.13}$$

Equation (7.12) shows that canonical spin arises if there is a non-zero difference between the canonical momentum carried by right- and left-handed photons, and similarly, Poynting spin is generated when there is a discrepancy in left-/right-handed spin momentum Eq. (7.13).

We can draw geometric conclusions from Eqs. (7.12) and (7.13), too. Often in an evanescent wave or a beam it is simple to define 'longitudinal' and 'transverse' directions based on the field's direction of propagation (hence the significance of transverse spin and spin momentum [2, 52]). From the discussions of [145] (and

as we shall soon see) it is tempting to associate $\mathbf{s}_\mathrm{c}$ and $\mathbf{s}_\mathrm{p}$ with longitudinal and transverse components of total spin $\mathbf{S}$. Yet, it is not possible to define longitudinal and transverse directions in general interference because phasefronts may become complicated surfaces requiring that the direction of phase increase needs to be defined locally, usually via a local wavevector [56, 57] that is proportional to canonical momentum Eq. (7.10). Since $\mathbf{p}_\mathrm{R} - \mathbf{p}_\mathrm{L}$ is not generally parallel to $\mathbf{p}_\mathrm{R} + \mathbf{p}_\mathrm{L}$ it cannot be a general conclusion that $\mathbf{s}_\mathrm{c}$ always points in a local longitudinal direction with reference to the local wavevector, and likewise for Poynting spin and the transverse direction.

7.1.3 Time-varying light

So far we have only treated time-averaged quantities calculated for monochromatic waves in free space yet, besides a small complication, it is also possible to construct an equivalent time-varying spin decomposition. In truth the spin vector $\mathbf{S}$ which we said in chapter 2 was, according to a continuity equation, the flow of helicity density h, corresponds to just one of an infinite number of conserved quantities discovered and named 'zilches' by Lipkin [72].

One interpretation of why the zilches are infinite in number is that the instantaneous fields $\boldsymbol{\mathcal{E}}$ and $\boldsymbol{\mathcal{H}}$ are simply a pair of rungs on a ladder of infinitely differentiable fields, and each pair of rungs share a set of Maxwell-like equations, symmetric under a continuous transformation that results in a conserved quantity related to the difference in number of right- and left-handed photons [35]. That the zilches and their fluxes tend to be ignored in favour of helicity is in part because of the familiarity of its dimensions, and due in time-harmonic fields to time derivatives simplifying to a multiplication by a constant, $\partial/\partial t \to -i\omega$, making the entire hierarchy of conserved

quantities and flows including helicity density and spin proportional for monochromatic light [73]. But in general the zilches and their fluxes are distinct from each other and arise from different symmetries of the form of Maxwell's equations; the continuous dual symmetry of the equations [invariance to continuous exchange of $\boldsymbol{\mathcal{E}}$ and $\boldsymbol{\mathcal{H}}$ according to a transformation angle θ, Eq. (5.18)] gives rise to the conservation of helicity density while for instance *chirality* density, often colloquially interchanged with helicity density, is conserved from the symmetry of Maxwell's equations to transformations of vector potentials [77, 157][†]. It is in fact the chirality density that is the gauge-independent quantity, whose flow $\boldsymbol{\mathcal{F}}(\mathbf{r}, t)$ is defined as [72, 73, 78, 158]

$$\boldsymbol{\mathcal{F}} = \frac{1}{2}\left(\boldsymbol{\mathcal{E}} \times (\nabla \times \boldsymbol{\mathcal{H}}) - \boldsymbol{\mathcal{H}} \times (\nabla \times \boldsymbol{\mathcal{E}})\right). \tag{7.14}$$

Immediately we may split this expression of chiral flow into terms resembling $\mathbf{s}_\mathrm{c}$ and $\mathbf{s}_\mathrm{p}$ using the same vector identities that obtain Eq. (7.2) and Eq. (7.3):

$$\boldsymbol{\mathcal{F}} = \frac{1}{2}\left[(\boldsymbol{\mathcal{E}} \cdot (\nabla)\boldsymbol{\mathcal{H}} - \boldsymbol{\mathcal{H}} \cdot (\nabla)\boldsymbol{\mathcal{E}}) + \nabla \times (\boldsymbol{\mathcal{E}} \times \boldsymbol{\mathcal{H}})\right]. \tag{7.15}$$

We have arrived at a more general expression of what are chiral-flow-equivalent terms to canonical and Poynting spin in Eq. (7.2), valid for polychromatic light at all instants—though they are not the same as the actual time-dependent versions of $\mathbf{s}_\mathrm{c}$ and $\mathbf{s}_\mathrm{p}$ that relate to the flow of helicity. These we may obtain in the Coulomb gauge by appropriately swapping the fields for vector potentials, $\boldsymbol{\mathcal{E}} \to \boldsymbol{\mathcal{A}}$ and $\boldsymbol{\mathcal{H}} \to \boldsymbol{\mathcal{C}}$. A third term $[\rho/(2\epsilon)]\boldsymbol{\mathcal{H}}$ appended to Eq. (7.15) can account for electric charge which give the electric field divergence, $\nabla \cdot \boldsymbol{\mathcal{E}} = \rho/\epsilon$.

[†]Chirality density C, associated with $\boldsymbol{\mathcal{F}}$ given by Tang and Cohen [78], is $C = [\epsilon_0 \boldsymbol{\mathcal{E}} \cdot (\nabla \times \boldsymbol{\mathcal{E}}) + (1/\mu_0)\boldsymbol{\mathcal{B}} \cdot (\nabla \times \boldsymbol{\mathcal{B}})]/2$, which in monochromatic light simplifies using phasors to $-\omega\Im\{\mathbf{E}^* \cdot \mathbf{H}\}/(2c^2)$ [73]. On the other hand, helicity density in monochromatic light is $h = -\Im\{\mathbf{E}^* \cdot \mathbf{H}\}/(2\omega c) = cC/\omega^2$ [36, 76]. The two are non-proportional, distinct quantities in time-dependent fields.

7.1.4 As 4-vectors

Building further upon our physical understanding of canonical and Poynting spin we shall attempt to appreciate how the spin decomposition transforms between reference frames in the relativistic sense. To do so we must additionally calculate the time components of $\mathbf{S}$, $\mathbf{s}_\mathrm{c}$ and $\mathbf{s}_\mathrm{p}$ and construct a 4-vector version of the spin decomposition which holds across both spatial and temporal components. Each of the total, canonical and Poynting spin vectors can, as we show, be expressed by combining 4-vectors related to the electric and magnetic fields (or rather, the field strength tensor) in some vector operation that acts over four dimensions, but which can no longer be written so conveniently as in three dimensions (e.g., with $\nabla\cdot$, $\nabla\times$).

Instead, we represent a 4-vector by a scalar expression for its μ^{th} component where μ, like any other Greek index used in this section (ν) is free to range from 0 to 3, the 0 index corresponding to the vector's time component. Careful use and repetition of multiple indices with special tensors can encode inter-component multiplication and summation. For example, $\partial_i X_i \equiv \sum \partial_i X_i = \partial_1 X_1 + \partial_2 X_2 + \partial_3 X_3$ where $i = (1,2,3) \equiv (x,y,z)$ is equivalent to $\nabla \cdot \mathbf{X}$ and $\epsilon_{ijk}\partial^j X^k \equiv \nabla \times \mathbf{X}$, where ϵ_{ijk} is the Levi-Civita symbol. Note that there is no sign difference between a 3-vector expressed by raised and lowered indices (i.e., X^i and X_i) but that there is a difference for 4-vectors and 4-tensors in the sign of some elements, in accordance with the Minkowski metric $\eta_{\mu\nu} = \mathrm{diag}(-1,1,1,1)$ that transforms $X_\mu = \eta_{\mu\nu}X^\nu$. More detail may be found in [159] and (specific to this section) in our original work [31].

An electric field in one reference frame is a mixture of both electric and magnetic fields from another reference frame. The mechanics of a Lorentz transform and this mixing of electric and magnetic fields are incorporated into the (phasor-

representation) field strength tensor $F_{\mu\nu}$,

$$F_{\mu\nu} = \begin{pmatrix} 0 & -E_x/c & -E_y/c & -E_z/c \\ E_x/c & 0 & -\mu_0 H_z & \mu_0 H_y \\ E_y/c & \mu_0 H_z & 0 & -\mu_0 H_x \\ E_z/c & -\mu_0 H_y & \mu_0 H_x & 0 \end{pmatrix} = \partial_\mu A_\nu - \partial_\nu A_\mu, \tag{7.16}$$

a 4-tensor defined by the derivatives of the electric 4-potential $A^\mu = (\phi/c, \mathbf{A})^T$ and that may be converted to the instantaneous version via $\mathcal{F}_{\mu\nu} = \Re\{F_{\mu\nu}\exp(-i\omega t)\}$. Similarly defined by the magnetic potential $C^\mu = (\psi, -i\omega\mu_0^{-1}(\nabla \times \mathbf{A}))^T$ is the dual electromagnetic tensor (a pseudo-tensor) $G_\mu\nu = \partial_\mu C_\nu - \partial_\nu C_\mu$.

Already knowing the spatial definitions of the spin decomposition vectors we can use the two 4-tensors and 4-potentials to define the 4-vectors corresponding to total spin $S^\mu = (S^0, \mathbf{S})^T$, $s_{\mathrm{p}}^\mu = (s_{\mathrm{c}}^0, \mathbf{s}_{\mathrm{c}})^T$ and $s_{\mathrm{p}}^\mu = (s_{\mathrm{p}}^0, \mathbf{s}_{\mathrm{p}})^T$ such that the spin decomposition works across all four components, i.e., $S^\mu = s_{\mathrm{c}}^\mu + s_{\mathrm{p}}^\mu$. In the Coulomb gauge for which $\nabla \cdot \mathbf{A} = \phi = 0$ and $\nabla \cdot \mathbf{C} = \psi = 0$, these vectors are:

$$S^\mu = \frac{1}{4}\Re\left\{A_\nu^* G^{\nu\mu} + C_\nu^* F^{\nu\mu}\right\} = \begin{pmatrix} -\Im\{\mathbf{E}^* \cdot \mathbf{H}\}/(2\omega c) \\ \mathbf{S} \end{pmatrix}, \tag{7.17}$$

$$s_{\mathrm{c}}^\mu = \frac{1}{4}\Re\left\{A_\nu^* \left(\partial^\mu C^\nu\right) - C_\nu^* \left(\partial^\mu A^\nu\right)\right\} = \begin{pmatrix} -\Im\{\mathbf{E}^* \cdot \mathbf{H}\}/(2\omega c) \\ \mathbf{s}_{\mathrm{c}} \end{pmatrix}, \tag{7.18}$$

$$s_{\mathrm{p}}^\mu = \frac{1}{4}\Re\left\{C_\nu^* \left(\partial^\nu A^\mu\right) - A_\nu^* \left(\partial^\nu C^\mu\right)\right\} = \begin{pmatrix} 0 \\ \mathbf{s}_{\mathrm{p}} \end{pmatrix}. \tag{7.19}$$

Total spin's time component is the helicity density $h = -\Im\{\mathbf{E}^* \cdot \mathbf{H}\}/(2\omega c)$, whose flux is the familiar spatial portion $\mathbf{S}$ according to a continuity equation [35]. We see,

interestingly, that in the sum $S^\mu = s^\mu_{\rm c} + s^\mu_{\rm p}$ this time component is supplied entirely by canonical spin for Poynting spin's time component is zero.

7.2 Examples of the decomposition

In this section we shall apply Eq. (7.2) to a handful of monochromatic scenarios, first in an evanescent wave where we recreate the finding of [145] for a linearly polarised wave, then in a linearly polarised Gaussian beam, an azimuthal beam and a linearly polarised vortex beam. For each example we contextualise the decomposition by highlighting the direction of the (sometimes orthogonal) pressure and recoil force terms of Eq. (7.7). A particularly surprising result is found in the centre of the linearly polarised vortex where there lies a two-dimensional dark spot.

7.2.1 Evanescent waves

An evanescent wave, polarised with a mixture of TE and TM components, has the following electric and magnetic phasors when propagating in the $+z$ direction and decaying in amplitude in the $+x$ direction with decay constant $\gamma = \sqrt{k_z^2 - k^2}$,

$$\mathbf{E} = \begin{pmatrix} A_p \frac{k_z}{k} \\ A_s \\ -iA_p \frac{\gamma}{k} \end{pmatrix} \mathrm{e}^{ik_z z - \gamma x} \quad \mathbf{H} = \frac{1}{\eta} \begin{pmatrix} -A_s \frac{k_z}{k} \\ A_p \\ iA_s \frac{\gamma}{k} \end{pmatrix} \mathrm{e}^{ik_z z - \gamma x}, \tag{7.20}$$

The complex amplitudes A_s and A_p determine the polarisation of the wave, for example if $(A_s, A_p) = (1, 0)$ then the wave is TE-polarised, if $A_p = \pm iA_s$ then the wave is circularly polarised. Depending on the polarisation of the wave the

orientation of $\mathbf{S}$, $\mathbf{s}_\mathrm{c}$ and $\mathbf{s}_\mathrm{p}$,

$$\frac{\mathbf{S}}{W} = \frac{1}{\omega k_z}\left[\gamma\hat{\mathbf{y}} + k\sigma\hat{\mathbf{z}}\right], \tag{7.21}$$

$$\frac{\mathbf{s}_\mathrm{c}}{W} = \frac{1}{\omega k_z}\left[\frac{k_z^2}{k}\sigma\hat{\mathbf{z}}\right], \tag{7.22}$$

$$\frac{\mathbf{s}_\mathrm{p}}{W} = \frac{1}{\omega k_z}\left[\gamma\hat{\mathbf{y}} - \frac{\gamma^2}{k}\sigma\hat{\mathbf{z}}\right], \tag{7.23}$$

changes; in these expressions the wave's polarisation is accounted for by what is the degree of circular polarisation in the sense of a plane wave, $\sigma = 2\Im\{A_s A_p^*\}/(|A_s|^2 + |A_p|^2)$, equal to 0 when the wave is linearly polarised and $\sigma = \pm 1$ when circularly polarised. We have normalised each vector by the x-dependent energy density W of the evanescent wave,

$$W = \epsilon_0 \frac{k_z^2}{k^2} e^{-2\gamma x}\frac{1}{2}\left(|A_s|^2 + |A_p|^2\right). \tag{7.24}$$

The total spin Eq. (7.21) of the wave carries a polarisation dependent ($\propto \sigma$) $\hat{\mathbf{z}}$ component and a polarisation independent transverse $\hat{\mathbf{y}}$ component which is well-understood [52], but what the authors of [145] identified is that this transverse component is a product only of Poynting spin Eq. (7.23) whose $\hat{\mathbf{y}}$ component is equal to that of $\mathbf{S}$. However for an elliptically polarised wave $\sigma \neq 0$, both canonical and Poynting spins acquire a longitudinal component so it is untrue that Poynting spin directly corresponds to helicity-independent transverse direction, tempting though it may be to suggest. Quite surprisingly the Poynting spin in a circularly polarised wave points backwards, compensating in its sum with the too-large canonical spin that is scaled by k_z/k ($k_z > k$). Referring Eqs. (7.21)-(7.23) to the chiral force equation Eq. (7.7), we see that only relatively weaker chiral recoil forces act in the transverse direction in agreement with [150] while both recoil force and the relatively

stronger chiral pressure ($\propto \mathbf{s}_\mathrm{c}$) can be exerted on a particle parallel to the propagation direction—transverse and longitudinal forces in an evanescent wave are caused by physically distinct light-matter interactions.

7.2.2 Beams

Earlier, we suggested that the Poynting spin term infuses the familiar total spin vector $\mathbf{S}$ with the effects of OAM, that twist the Poynting vector into curling vortices, and those of non-uniform, doughnut-shaped intensity profiles, in a coupling which has striking implications for structured light. That is why in this subsection we will calculate Eq. (7.2) for three linearly polarised, focussed beams: an $\hat{\mathbf{x}}$ polarised Gaussian beam, an azimuthally polarised doughnut beam with planar wavefronts and an $\hat{\mathbf{x}}$ polarised vortex beam with helical wavefronts. Strong focussing in each of these beams introduces out-of-plane, longitudinal $\hat{\mathbf{z}}$ components that oscillate out of phase with the in-plane transverse field, imparting electric and magnetic spin vectors with transverse components. Factors differentiating the three beams—the intensity profile, presence of OAM, electric and magnetic polarisation—drastically influcence the orientation and strength of canonical spin $\mathbf{s}_\mathrm{c}$ and Poynting spin $\mathbf{s}_\mathrm{p}$.

Non-paraxial vortex beams are notoriously challenging to model mathematically because they cannot currently be described by closed-form analytical expressions. All three beams are created numerically using an angular spectrum integration method [160], an approach that can also generate non-paraxial vector vortex beams by first forcing the transverse electric field to match the beam's paraxial description precisely in the focal plane, before calculating the magnetic field and the rest of the electric field (all of its components outside the focal plane, as well as its longitudinal component on the focal plane) using Maxwell's equations. While any beam gener-

ated this way is perfectly physical (satisfying Maxwell's equations), one potential consequence is polarisation asymmetry between the transverse **E** and **H** fields in the focal plane—there, only the magnetic field's transverse components can inherit the effects of strong focussing because, as we said, the transverse electric field components are forced to conform to the paraxial beam expression (we might say the beam is electric-biased). But by use of a discrete duality transform we can superimpose an electric-biased and magnetic-biased beam (where the magnetic field matches the paraxial description in the focal plane) to obtain a combined beam which matches previous expansions of the linearly polarised vortex's fields[‡] [105]. The vectors that are of interest to us, $\mathbf{S}$, $\mathbf{s}_{\mathrm{c}}$, $\mathbf{s}_{\mathrm{p}}$, and $\mathbf{P}$, are all dual-symmetric quantities. In our subsequent discussions each beam propagates in the $\hat{\mathbf{z}}$ direction such that any mention of the 'transverse plane' refers to the xy plane.

First, the Gaussian beam decomposed in Fig. 7.2(a). Gaussian non-uniformity in the magnitude of the Poynting vector across the face of the beam means that even though $\mathbf{P}$ is purely longitudinal, $\nabla \times \mathbf{P}$ is non-zero giving Poynting spin, proportional to this curl, a non-zero component in the transverse plane, consistent with the well-understood presence of $\hat{\mathbf{z}}$ components of the electric and magnetic fields which develop along with azimuthal transverse spin due to focussing. Neither total spin nor its decomposed parts contain longitudinal components because the beam is linearly polarised in the transverse plane. The linearly polarised Gaussian beam's spin decomposition resembles that of the linearly polarised ($\sigma = 0$) evanescent wave, in that $\mathbf{S}$ is entirely transverse and supplied only by $\mathbf{s}_{\mathrm{p}}$ while $\mathbf{s}_{\mathrm{c}} = \mathbf{0}$, but this $\mathbf{s}_{\mathrm{p}}$-transverse-

[‡]In the published version of this work, an electric biased vortex beam is used which, as a consequence, has a non-zero longitudinal component in the total SAM density $\mathbf{S} \cdot \hat{\mathbf{z}}$ (which is equal to longitudinal magnetic SAM density $\mathbf{S}_{\mathrm{m}} \cdot \hat{\mathbf{z}}$). This alternative beam is a perfectly physical—but less symmetric in polarisation—vortex beam and contains the same canonical spin phenomenon that we identify in the vortex beam of this thesis.

spin correspondence does not survive into the next example of the azimuthal beam.

In Fig. 7.2(b) $\mathbf{P}$, $\mathbf{S}$, $\mathbf{s}_\mathrm{c}$, and $\mathbf{s}_\mathrm{p}$ are plotted for the azimuthal beam, the electric field being linearly polarised and oriented azimuthally around the centre of the beam in the xy plane, with the orthogonal magnetic field oriented radially. Once more strong focussing creates a transverse circulation of total spin $\mathbf{S}$, though this time it is only contributed by the magnetic field (elliptically polarised in the ρz plane, radial in the xy plane) because the electric field is in fact completely linearly polarised in 3D. Organised in an enclosing, bright ring, most of the beam's energy density surrounds a dark spot at the centre of the beam, but this dark spot does not embed the beam with OAM and has a topological charge $l = 0$. Like the Gaussian beam, then, it is the variation in the magnitude $|\mathbf{P}|$ alone that creates Poynting spin in the transverse plane. Unlike the Gaussian beam, however, canonical spin $\mathbf{s}_\mathrm{c}$ *also* circulates in the transverse plane around the beam axis, contradicting the notion that could be drawn from the Gaussian beam and evanescent wave examples that Poynting spin is always responsible for transverse components of $\mathbf{S}$.

Finally, the $\hat{\mathbf{x}}$ polarised vortex beam. Only this beam of the three so far simulated in this section possesses OAM with sculpted, helical wavefronts, which impart transverse components to the Poynting vector $\mathbf{P}$ and profoundly influence the geometry of the $\mathbf{s}_\mathrm{c}$ and $\mathbf{s}_\mathrm{p}$ vectors in ways that the Gaussian beam and $l = 0$ azimuthal beam cannot accomplish. Though paraxially the beam is linearly polarised, after focussing both $\mathbf{E}$ and $\mathbf{H}$ fields obtain a slight ellipticity in the transverse plane giving longitudinal components to the electric and magnetic spin densities, $\mathbf{S}_\mathrm{e}$ and $\mathbf{S}_\mathrm{m}$, beside the dark axis of the beam, organised into four lobes with alternating sign. However the dual spin density, $\mathbf{S} = \mathbf{S}_\mathrm{e} + \mathbf{S}_\mathrm{m}$ as plotted in the third row of Fig 7.2(c), has no longitudinal component because those of the electric and magnetic contributions cancel completely as was reported previously [105]. Now that $\mathbf{P}$ twists

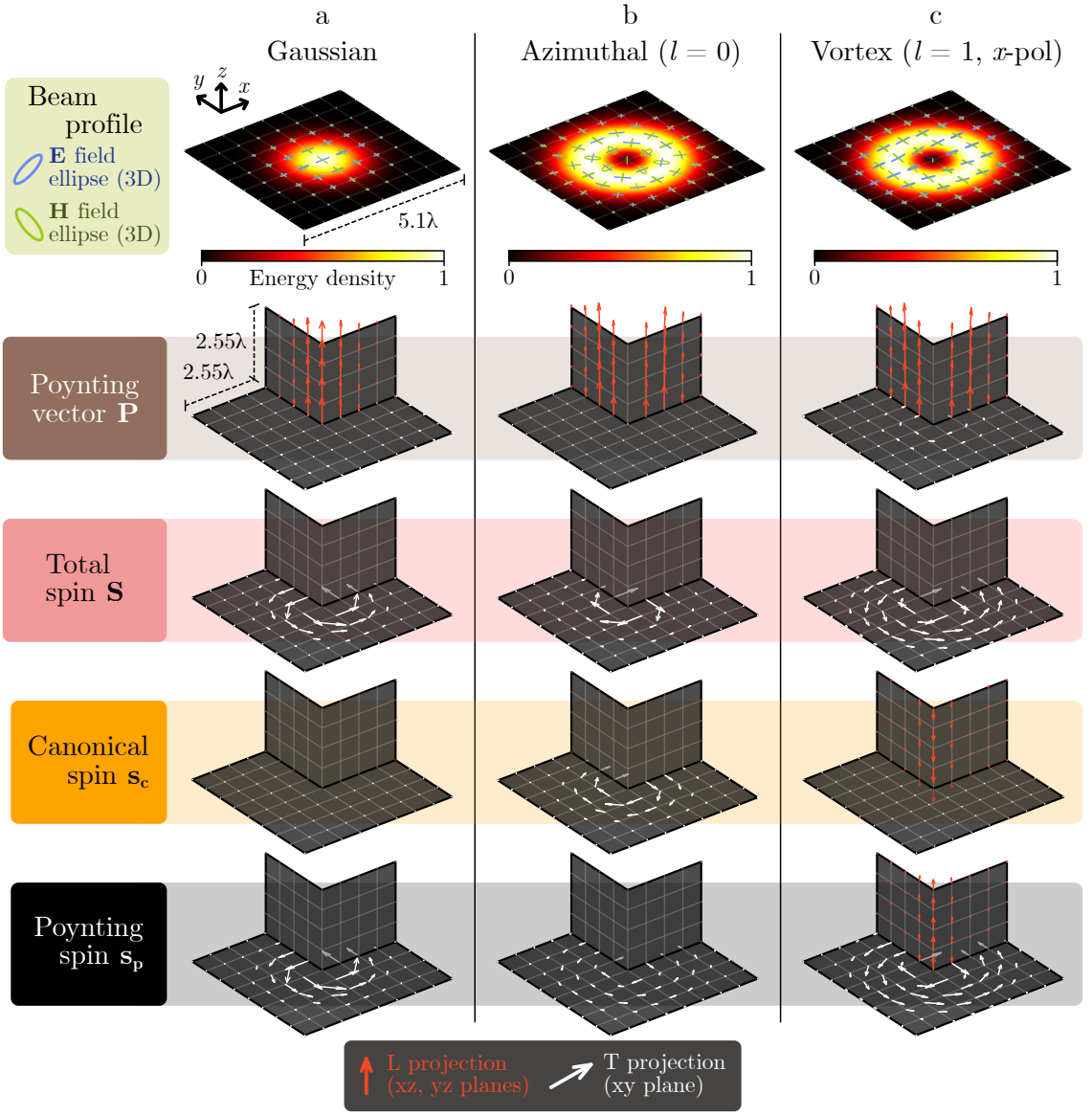

Figure 7.2: Decomposition of the total spin $\mathbf{S}$ of three focussed beams, columns (a)-(c), an $\hat{\mathbf{x}}$-polarised Gaussian beam, an azimuthal beam (topological charge $l = 0$) and an $\hat{\mathbf{x}}$-polarised vortex beam ($l = 1$). Each beam propagates along the z axis. In the first row the beam's normalised energy density in the focal plane (an xy plane) is plotted along with electric (blue) and magnetic (green) polarisation ellipses (which are oriented in 3D and elliptical due to the strong longitudinal polarisation component introduced by focussing). The second, third, fourth, and fifth rows show the Poynting vector $\mathbf{P}$, total spin $\mathbf{S}$, canonical spin $\mathbf{s}_c$, and Poynting spin $\mathbf{s}_p$ plotting separately each vector's transverse components (projected as white arrows on to the xy focal plane) and longitudinal components (projected as red arrows onto the xz and yz planes). Arrows in the final three rows are plotted in a consistent scale [the vector addition of arrows in the fourth and fifth rows would recover the third row in accordance with Eq. (7.2)]. Beams are generated numerically using the method described in [160]. Adapted from [31].

azimuthally around the centre of the vortex its curl and therefore $\mathbf{s}_\mathrm{p} \propto \nabla \times \mathbf{P}$ both gain a $\hat{\mathbf{z}}$ component, longitudinal to the beam according to the right hand rule, which is strongest at the centre of the vortex. Yet there is no longitudinal component to the *total* spin $\mathbf{S}$. The only way that $\mathbf{S} \cdot \hat{\mathbf{z}} = 0$ while $\mathbf{s}_\mathrm{p} \cdot \hat{\mathbf{z}} \neq 0$ is if canonical spin $\mathbf{s}_\mathrm{c}$ points, in the longitudinal direction, equally and opposite to Poynting spin so that $\mathbf{S} \cdot \hat{\mathbf{z}} = (\mathbf{s}_\mathrm{c} + \mathbf{s}_\mathrm{p}) \cdot \hat{\mathbf{z}} = 0$. Recalling the chiral force equation Eq. (7.7) we are reminded that chiral pressure, the interaction term, points in the direction of canonical spin while chiral recoil forces depend on the electric and magnetic parts of total spin, $\mathbf{S} = \mathbf{S}_\mathrm{e} + \mathbf{S}_\mathrm{m}$—the implication being that at the centre of the linearly polarised vortex where $\mathbf{S} \cdot \hat{\mathbf{z}} = 0$ and both electric and magnetic spin densities are zero, a relatively strong axial chiral pressure force is present! Chiral enantiomers with differently signed chiral polarisabilities should experience opposing longitudinal forces in the centre of the linearly polarised vortex which, we might interpret as a conversion of OAM to chiral momentum, $\mathbf{p}_\mathrm{R} - \mathbf{p}_\mathrm{L} = k\mathbf{s}_\mathrm{c}$ from Eq. (7.12), given that $\mathbf{s}_\mathrm{p} \propto \nabla \times \mathbf{P}$, $\mathbf{s}_\mathrm{c}$ and thus chiral pressure all three switch direction in an oppositely handed beam (note that the longitudinal SAM density $\mathbf{S} \cdot \hat{\mathbf{z}}$ of the beam remains zero, so there is not necessarily an orbit-to-spin angular momentum conversion). Chiral interactions between OAM and dipolar particles [an assumption of Eq. (7.7)] have been predicted only relatively recently [76, 97, 161] and these are understood to depend on the strong longitudinal field components brought about through beam focussing. But our identification of an axial chiral pressure force, dependent on the sign of the topological charge of a linearly polarised vortex, seems only to hinge on $\mathbf{P}$ having a non-zero curl parallel to the beam, something which should still persist in the paraxial limit (albeit significantly weakened) even if polarisation is confined to the transverse plane. Although it was shown around twenty years ago that OAM-

dependent *absorption* did not occur in dipolar particles in the paraxial limit[§] [162, 163], forces according to Eq. (7.7) arise due to *extinction*.

7.2.3 Spin-free chiral forces

Subtleties between the force terms in Eq. (7.7) compounded by the geometry of the three vectors $\mathbf{S}$, $\mathbf{s}_\mathrm{c}$, and $\mathbf{s}_\mathrm{p}$ create some scope for confusion, particularly if we claim that the axial chiral force which we predict to exist at the centre of a linearly polarised vortex is 'in the absence of spin'. For instance it is known that a linearly polarised evanescent wave, consistent with our equations in section 7.2.1, exhibits a a lateral chiral force proportional to its transverse spin [150] which could be argued a 'spin-free' force since the wave may be excited by a linearly polarised source. Here we will distinguish this force from what we have predicted in the previous section, in two ways.

Even though it may be excited by a linearly polarised source the TE (TM) evanescent wave itself is elliptically polarised in the magnetic (electric) field, the plane of the polarisation ellipse parallel to the direction of propagation, its spin vector transverse and *parallel* to the direction of the predicted lateral chiral sorting force. What we have predicted in the middle of the linearly vortex beam contrasts sharply because the chiral force, proportional to $\mathbf{s}_\mathrm{c}$, points longitudinally despite the beam being linearly polarised in the transverse plane and $\mathbf{S} = \mathbf{0}$ in the beam's dark centre; we would describe this force as being spin-free in a very literal sense, not simply that the beam can be generated from a linearly polarised source.

Secondly, as the authors of [150] explain the evanescent wave's lateral chiral force is a recoil term and arises from a dipolar particle's unbalanced radiation.

[§]It is very much possible in focussed beams [97].

	Evanescent wave from linearly polarised illumination	**Centre of linearly polarised vortex beam**
Chiral force $\mathbf{F}_{\text{chiral}}$	$\mathbf{F}_{\text{chiral}} \neq 0$ (transverse)	$\mathbf{F}_{\text{chiral}} \neq 0$ (longitudinal)
Type of chiral force	Spin recoil force $\mathbf{F}_{\text{chiral}} \propto \mathbf{S}$ negligible in small particles	Chiral pressure force $\mathbf{F}_{\text{chiral}} \propto \mathbf{s}_{\text{c}}$ dominant in small particles
Total spin $\mathbf{S} = \mathbf{s}_{\text{c}} + \mathbf{s}_{\text{p}}$	$\mathbf{S} \neq 0$	$\mathbf{S} = 0$
Canonical spin $\mathbf{s}_{\text{c}}$	$\mathbf{s}_{\text{c}} = 0$	$\mathbf{s}_{\text{c}} \neq 0$ (longitudinal)
Poynting spin $\mathbf{s}_{\text{p}}$	$\mathbf{s}_{\text{p}} \neq 0$ (transverse)	$\mathbf{s}_{\text{p}} = -\mathbf{s}_{\text{c}}$

Table 7.1: Comparison of the features of predicted chiral forces with reference to the spin decompostion in a linearly polarised evanescent wave [150] and the centre of a linearly polarised vortex. Adapted from [31].

Meanwhile the vortex beam's chiral force derives from the relatively stronger chiral pressure—an enantiomer feels this longitudinal force because, for instance, it experiences more impacts from right-handed photons than left-handed photons (recall that we showed $\mathbf{s}_{\text{c}} \propto \mathbf{p}_{\text{R}} - \mathbf{p}_{\text{L}}$). We summarise this discussion in Table 7.1

7.3 Chapter summary

One of the initial aims of the results of this chapter, published in [31], were to better understand what at current is a little-known decomposition of light's SAM density vector, $\mathbf{S} = \mathbf{s}_{\text{c}} + \mathbf{s}_{\text{p}}$, into two terms which we called canonical spin $\mathbf{s}_{\text{c}}$ and Poynting spin $\mathbf{s}_{\text{p}}$. For it was realised that this decomposition runs parallel to a well-established expression of the Poynting vector $\mathbf{P} = c^2\mathbf{p} + c^2\mathbf{p}^{\text{s}}$ as a sum of canonical momentum $\mathbf{p}$ and spin momentum $\mathbf{p}^{\text{s}}$ [33] which is important in our understanding of achiral optical forces and definitions of momentum density in light that relate to the Abraham-Minkowski dilemma. We showed that canonical spin and Poynting spin are chiral analogies to canonical and spin momentum, in that the two spin terms are proportional to the difference in their achiral linear momentum counterparts carried by right- and left-handed photons, that is $\mathbf{s}_{\text{c}} = (\mathbf{p}_{\text{R}} - \mathbf{p}_{\text{L}})/k$ and $\mathbf{s}_{\text{p}} = (\mathbf{p}^{\text{s}}_{\text{R}} -$

$\mathbf{p}_{\mathrm{L}}^{\mathrm{s}})/k$. Canonical spin gives rise to chiral pressure, a direct field interaction force that enantiomers feel in opposite directions while Poynting spin, proportional to $\nabla \times \mathbf{P}$ and incorporating light's OAM, manifests only in weaker chiral recoil forces felt by particles in the Rayleigh regime [all in accordance with Eq. (7.7)]. It is interesting to ask whether between total spin $\mathbf{S}$ and canonical spin $\mathbf{s}_{\mathrm{c}}$ calculated in free space and dispersive media there also exists an analogy to the Abraham-Minkowski dilemma.

Both canonical and Poynting spins could be measured by detecting their corresponding chiral forces, isolated, in different scenarios. Canonical spin could, we suggest, be detected at the centre of a linearly polarised vortex beam where it induces a longitudinal chiral pressure force while total spin (producing chiral recoil force) is zero in addition to achiral forces being minimal due to vanishing transverse $\mathbf{E}$ and $\mathbf{H}$ components. Careful choice of the beam's wavelength with respect to the chiral particles probing the beam (such that the particle's electric polarisability switches sign) would make it possible for the enantiomers to be trapped in the centre of the vortex by achiral gradient forces that point in the direction of decreasing field intensity, where they may then respond preferentially to chiral pressure. That said, a complete analysis of the total force on a small chiral particle using its polarisability would be needed to determine the feasibility of an experiment. Poynting spin, on the other hand, could be measured in a linearly polarised evanescent wave by detection of its lateral chiral force, predicted by [150], which is a recoil force that is only contributed to by Poynting spin as [145] and we have established. A similar experimental set up to that which detected lateral forces in evanescent waves due to spin momentum [58] could be used.

As well as finding the physical significance of $\mathbf{s}_{\mathrm{c}}$ and $\mathbf{s}_{\mathrm{p}}$ we wished to demonstrate what we believe to be the two primary advantages to the spin decomposition Eq. (7.2), that might benefit the research community. The first relates to the fact

that given the current literature surrounding chiral optical forces, it is difficult to develop a consistent intuition which one can use to judge how an electromagnetic field such as a beam would interact with matter. Conventionally we might plot the spin (via polarisation ellipses) and flow of kinetic momentum (via the Poynting vector) of a beam to gain a fairly good picture of its characteristics, though many crucial details of how matter responds to the beam remain hidden until force calculations are done in full. The decomposition of the linearly polarised vortex is an excellent example as we showed that while total longitudinal spin $\mathbf{S}\cdot\hat{\mathbf{z}} = (\mathbf{s}_\mathrm{c} + \mathbf{s}_\mathrm{p})\cdot\hat{\mathbf{z}} = 0$ is zero in the beam center, canonical and Poynting spins can individually be non zero, satisfying $\mathbf{s}_\mathrm{c}\cdot\hat{\mathbf{z}} = -\mathbf{s}_\mathrm{p}\cdot\hat{\mathbf{z}}$. We were then led to predict the existence of an axial chiral force in the absence of total spin, a fact which is not at all obvious if we naively assume that the field polarisation ellipses are enough to judge whether or not chiral forces are present. We have provided a link between total spin, related to polarisation ellipses, and the vorticity of the Poynting vector (Poynting spin) which are reasonably intuitive quantities that can be used to infer details about chiral interaction forces that stem from the difference in momentum carried by oppositely handed photons.

Besides this intuition, the spin decomposition offers another advantage in simplifying optical force expressions. The literature is perhaps notoriously inconsistent in expressing achiral and chiral forces, tending to be divided between expressions written using cross-sections or with polarisabilities. It is conventional to divide the total force into three terms, constituting a gradient force, an interaction force (non-reciprocal) and a recoil force. However, because the spin decomposition is scarcely known the chiral interaction force is often written by authors in an unnecessarily complicated way (for example Eq. (2) of [150]). Using a definition of chiral momentum $\mathbf{p}_c = k\mathbf{s}_c$ [53] simplifies the term and results in Eq. (17) of [43], where one sees that chiral and achiral force terms mirror each other with a very similar structure.

Our last remark is that the spin decomposition Eq. (7.2) can be formulated in other wave fields including those of linearised acoustics (spin-0) and linearised gravity (spin-2) which both have different vector and tensor structures to light, and may therefore be of interest to a broader community beyond optics. Gravitational waves are tensor waves that, at large distances from their source, may be described by a linear wave theory without self-interaction, governed by expressions which can be made to take a remarkably similar form to Maxwell's equations as Barnett showed [164]. The basis for this formulation is the symmetric metric perturbation tensor $h_{\mu\nu}$ whose time components are zero in the transverse-traceless gauge in far fields [17]. By treating the rows or columns (identical due to symmetry) of the non-zero spatial portion of the perturbation tensor h_{ij} as vector potentials $\mathbf{A}^i = h^{ij}\hat{\mathbf{e}}_j$ we may then define tensor analogues to the electric and magnetic fields whose i^{th} rows (3-vectors) are $\mathbf{E}^i = i\omega(h^{ij}\hat{\mathbf{e}}_j)$ and $\mathbf{H}^i = (1/\mu_0)\nabla \times (h^{ij}\hat{\mathbf{e}}_j)$. Subsequent gravitational analogues of the energy density, Poynting vector, SAM density, helicity density take an almost identical form to the electromagnetic definitions after choosing $\epsilon_0 = 1/(c^2\mu_0) = c^2/(32\pi G)$ except for summation over an additional index, and a factor of two accounting for the wave's spin-2 character in SAM density and helicity density. Acoustic waves, on the other hand, are described in a linearised theory by a scalar pressure field P and a vector velocity field $\mathbf{v}$. A longitudinality condition $\nabla \times \mathbf{v} = \mathbf{0}$ reduces polarisation degrees of freedom to one such that both helicity density and the acoustic wave's canonical spin analogue is zero (presumably acoustic canonical spin would relate to momentum discrepancy between left- and right-handed phonons, though phonons in longitudinal acoustic waves are spin-0 particles and do not have any handedness, hence the canonical spin equaivalent and helicity density are zero). Many geometric relationships between acoustic quantities, including the proportionality between the acoustic analogies of spin and the curl of the Poynting

vector, have been given in [165]. Table 7.2 compares quantities including canonical and Poynting spin equivalents in light, acoustic waves and gravitational waves in linearised theories.

	Linearised Acoustics	**Electromagnetism**	**Linearised gravity**
Field phasors	$P = -i\omega\rho\varphi$ $\mathbf{v} = \nabla\varphi$	$\mathbf{E} = i\omega\mathbf{A}$ $\mathbf{H} = \frac{1}{\mu_0}\nabla \times \mathbf{A}$	$\mathbf{E}^i = i\omega(h^{ij}\hat{\mathbf{e}}_j)$ $\mathbf{H}^i = \frac{1}{\mu_0}\nabla \times (h^{ij}\hat{\mathbf{e}}_j)$
Energy density	$\frac{1}{4}(\beta\lvert P\rvert^2 + \rho\lvert\mathbf{v}\rvert^2)$	$\frac{1}{4}(\epsilon_0\lvert\mathbf{E}\rvert^2 + \mu_0\lvert\mathbf{H}\rvert^2)$	$\frac{1}{4}(\epsilon_0\mathbf{E}_i^* \cdot \mathbf{E}^i + \mu_0\mathbf{H}_i^* \cdot \mathbf{H}^i)$
Helicity density	0	$-\frac{1}{2\omega c}\mathrm{Im}\{\mathbf{E}^* \cdot \mathbf{H}\}$	$-\frac{1}{\omega c}\mathrm{Im}\{\mathbf{E}_i^* \cdot \mathbf{H}^i\}$
Poynting vector	$\frac{1}{2}\mathrm{Re}\{P^*\mathbf{v}\}$	$\frac{1}{2}\mathrm{Re}\{\mathbf{E}^* \times \mathbf{H}\}$	$\frac{1}{2}\mathrm{Re}\{\mathbf{E}_i^* \times \mathbf{H}^i\}$
SAM density	$\frac{1}{2\omega}\mathrm{Im}\{\rho\mathbf{v}^* \times \mathbf{v}\}$	$\frac{1}{4\omega}\mathrm{Im}\{\epsilon_0\mathbf{E}^* \times \mathbf{E} + \mu_0\mathbf{H}^* \times \mathbf{H}\}$	$\frac{1}{2\omega}\mathrm{Im}\{\epsilon_0\mathbf{E}_i^* \times \mathbf{E}^i + \mu_0\mathbf{H}_i^* \times \mathbf{H}^i\}$
Canonical spin	0	$\frac{1}{4\omega^2}\mathrm{Re}\{\mathbf{E}^* \cdot (\nabla)\mathbf{H} - \mathbf{H}^* \cdot (\nabla)\mathbf{E}\}$	$\frac{1}{2\omega^2}\mathrm{Re}\{\mathbf{E}_i^* \cdot (\nabla)\mathbf{H}^i - \mathbf{H}_i^* \cdot (\nabla)\mathbf{E}^i\}$
Poynting spin	$\frac{1}{2\omega^2}\nabla \times \frac{1}{2}\mathrm{Re}\{P^*\mathbf{v}\}$	$\frac{1}{2\omega^2}\nabla \times \frac{1}{2}\mathrm{Re}\{\mathbf{E}^* \times \mathbf{H}\}$	$\frac{1}{\omega^2}\nabla \times \frac{1}{2}\mathrm{Re}\{\mathbf{E}_i^* \times \mathbf{H}^i\}$

Table 7.2: Comparison of time-averaged quantities in monochromatic acoustic, electromagnetic and gravitational waves, adapted from [31] and inspired by [17, 19, 166]. For electromagnetism, the potential is considered to be in the Coulomb gauge. For linearised gravity Einstein's index summation convention is used with h_{ij} being spatial components of the metric perturbation in the transverse-traceless gauge, while $\hat{\mathbf{e}}_i$ are basis vectors. We have specially chosen the parameters $\epsilon_0 = 1/(c^2\mu_0) = c^2/(32\pi G)$ so that the gravitational wave's time-averaged energy density resembles the electromagnetic definition.

Conclusions

This marks the end of this thesis. We began with the two background chapters 2 and 3, the first's broad focus including time-averaged electromagnetic quantities relating to light's energy, linear and angular momentum, and with the second chapter aimed more specifically at the rest of the thesis by developing a picture of light's polarisation structure and topological properties in paraxial and non-paraxial regimes. In chapters 4, 5, and 6, we presented our original findings on the many special features of dark spots in paraxial and non-paraxial fields, including non-diffracting structures that extend infinitely into the far field and intersecting polarisation singularities, and proposed a simple technique to synthesise them experimentally and control their position. We expect our discussions could prove useful in dark trapping, sub-wavelength optical microscopy techniques and in topological control. Lastly in chapter 7 we presented a decomposed representation of monochromatic light's spin angular momentum density. Rather than a sum of separate contributions from the electric and magnetic fields we gave an alternative sum of two terms, called canonical spin and Poynting spin, that relate respectively to the difference in canonical and spin momentum carried by left- and right-handed photons. We predicted using our expressions that a longitudinal chiral pressure force exists at the dark centre of a linearly polarised vortex beam, in absence of dual spin angular momentum density.

Author's merits

Publications

Vernon, A. J. & Rodríguez-Fortuño, F. J. Creating and moving nanoantenna cold spots anywhere. *Light: Science & Applications* **11.** doi:10.1038/s41377-022-00893-7 (1 Aug. 2022)

Vernon, A. J. *et al.* 3D zeros in electromagnetic fields. *Optica* **10,** 1231. doi:10.1364/OPTICA.487333 (9 Sept. 2023)

Vernon, A. J. *et al.* Non-diffracting polarization features around far-field zeros of electromagnetic radiation. *Optica* **11,** 120–127. doi:10.1364/OPTICA.502020 (Jan. 2024)

In press

Vernon, A. J. *et al.* A decomposition of light's spin angular momentum density. *Light: Science & Applications* (in-press, 2024)

Conferences

Vernon, A. J. & Rodríguez-Fortuño, F. J. *Creating and moving nanoantenna cold spots anywhere.* (talk) SPIE Photonics Europe. (Apr. 2022)

Vernon, A. J. *et al. Cold spots: a meeting point for polarisation singularities, and their complete position control.* (poster) ICOAM. (June 2022)

Vernon, A. J. *et al. Controlling light's darkness: tuning near-field cold spots and their properties.* (talk) SPIE Optics + Optoelectronics. (Apr. 2023)

Vernon, A. J. *et al. Electromagnetic vector field zeros: polarisation imprints, diffraction immunity and topological effects.* (talk) Twisted light in quantum and subatomic systems. (Sept. 2023)

Bibliography

1. Young, T. *Philosophical Transactions of the Royal Society of London* **92,** 12–48. doi:10.1098/rstl.1802.0004 (1802).
2. Bekshaev, A. Y., Bliokh, K. Y. & Nori, F. Transverse Spin and Momentum in Two-Wave Interference. *Physical Review X* **5.** doi:10.1103/PhysRevX.5.011039 (2015).
3. Nye, J. F. & Berry, M. V. Dislocations in wave trains. *Proceedings of the Royal Society of London. A. Mathematical and Physical Sciences* **336,** 165–190. doi:10.1098/rspa.1974.0012 (1974).
4. Karman, G. P., Beijersbergen, M. W., van Duijl, A. & Woerdman, J. P. Creation and annihilation of phase singularities in a focal field. *Optics Letters* **22,** 1503. doi:10.1364/OL.22.001503 (1997).
5. Berry, M. V. & Dennis, M. R. Knotted and linked phase singularities in monochromatic waves. *Proceedings of the Royal Society of London. Series A: Mathematical, Physical and Engineering Sciences* **457,** 2251–2263. doi:10.1098/rspa.2001.0826 (2001).
6. Leach, J., Dennis, M. R., Courtial, J. & Padgett, M. J. Knotted threads of darkness. *Nature* **432.** doi:10.1038/432165a (2004).
7. Allen, L., Beijersbergen, M. W., Spreeuw, R. J. C. & Woerdman, J. P. Orbital angular momentum of light and the transformation of Laguerre-Gaussian laser modes. *Physical Review A* **45,** 8185–8189. doi:10.1103/PhysRevA.45.8185 (1992).
8. Wang, J. *et al.* Terabit free-space data transmission employing orbital angular momentum multiplexing. *Nature Photonics* **6.** doi:10.1038/nphoton.2012.138 (2012).
9. Willner, A. E., Pang, K., Song, H., Zou, K. & Zhou, H. Orbital angular momentum of light for communications. *Applied Physics Reviews* **8.** doi:10.1063/5.0054885 (2021).

10. Bliokh, K. Y., Rodríguez-Fortuño, F. J., Nori, F. & Zayats, A. V. Spin–orbit interactions of light. *Nature Photonics* **9,** 796–808. doi:10.1038/nphoton.2015.201 (2015).

11. Tsesses, S. *et al.* Optical skyrmion lattice in evanescent electromagnetic fields. *Science* **361.** doi:10.1126/science.aau0227 (2018).

12. Sugic, D. *et al.* Particle-like topologies in light. *Nature Communications* **12.** doi:10.1038/s41467-021-26171-5 (2021).

13. Lim, S. W. D., Park, J.-S., Meretska, M. L., Dorrah, A. H. & Capasso, F. Engineering phase and polarization singularity sheets. *Nature Communications* **12,** 4190. doi:10.1038/s41467-021-24493-y (2021).

14. Wang, H. & Fan, S. Photonic Spin Hopfions and Monopole Loops. *Physical Review Letters* **131,** 263801. doi:10.1103/PhysRevLett.131.263801 (2023).

15. Ehrmanntraut, D. *et al.* Optical second-order skyrmionic hopfion. *Optica* **10,** 725. doi:10.1364/OPTICA.487989 (2023).

16. Dennis, M. R. *Topological singularities in wave fields* PhD thesis (University of Bristol, 2001).

17. Golat, S., Lim, E. A. & Rodríguez-Fortuño, F. J. Evanescent gravitational waves. *Physical Review D* **101,** 084046. doi:10.1103/PhysRevD.101.084046 (2020).

18. Bliokh, K. Y. *et al.* Polarization singularities and Möbius strips in sound and water-surface waves. *Physics of Fluids* **33.** doi:10.1063/5.0056333 (2021).

19. Bliokh, K. Y., Punzmann, H., Xia, H., Nori, F. & Shats, M. Field theory spin and momentum in water waves. *Science Advances* **8.** doi:10.1126/sciadv.abm1295 (2022).

20. Vernon, A. J., Dennis, M. R. & Rodríguez-Fortuño, F. J. 3D zeros in electromagnetic fields. *Optica* **10,** 1231. doi:10.1364/OPTICA.487333 (2023).

21. Vernon, A. J., Kille, A., Rodríguez-Fortuño, F. J. & Afanasev, A. Non-diffracting polarization features around far-field zeros of electromagnetic radiation. *Optica* **11,** 120–127. doi:10.1364/OPTICA.502020 (2024).

22. Grimm, R., Weidemüller, M. & Ovchinnikov, Y. B. Optical Dipole Traps for Neutral Atoms. *Advances In Atomic, Molecular, and Optical Physics.* doi:10.1016/S1049-250X(08)60186-X (2000).

23. Davidson, N., Lee, H. J., Adams, C. S., Kasevich, M. & Chu, S. Long Atomic Coherence Times in an Optical Dipole Trap. *Physical Review Letters* **74,** 1311–1314. doi:10.1103/PhysRevLett.74.1311 (1995).

24. He, H., Heckenberg, N. & Rubinsztein-Dunlop, H. Optical Particle Trapping with Higher-order Doughnut Beams Produced Using High Efficiency Computer Generated Holograms. *Journal of Modern Optics* **42.** doi:10.1080/09500349514550171 (1995).

25. Zemánek, P. & Foot, C. Atomic dipole trap formed by blue detuned strong Gaussian standing wave. *Optics Communications* **146,** 119–123. doi:10.1016/S0030-4018(97)00526-9 (1998).

26. Xu, P., He, X., Wang, J. & Zhan, M. Trapping a single atom in a blue detuned optical bottle beam trap. *Optics Letters* **35,** 2164. doi:10.1364/OL.35.002164 (2010).

27. Nelson, K. D., Li, X. & Weiss, D. S. Imaging single atoms in a three-dimensional array. *Nature Physics* **3,** 556–560. doi:10.1038/nphys645 (2007).

28. Hell, S. W. Far-Field Optical Nanoscopy. *Science* **316,** 1153–1158. doi:10.1126/science.1137395 (2007).

29. Hell, S. W. & Wichmann, J. Breaking the diffraction resolution limit by stimulated emission: stimulated-emission-depletion fluorescence microscopy. *Opt. Lett.* **19,** 780–782. doi:10.1364/OL.19.000780 (1994).

30. Balzarotti, F. *et al.* Nanometer resolution imaging and tracking of fluorescent molecules with minimal photon fluxes. *Science* **355,** 606–612. doi:10.1126/science.aak9913. eprint: https://www.science.org/doi/pdf/10.1126/science.aak9913 (2017).

31. Vernon, A. J., Golat, S., Rigouzzo, C., Lim, E. A. & Rodríguez-Fortuño, F. J. *A decomposition of light's spin angular momentum density (preprint)* 2023.

32. Jackson, J. D. *Classical Electrodynamics* Third (Wiley, 1998).

33. Berry, M. V. Optical currents. *Journal of Optics A: Pure and Applied Optics* **11.** doi:10.1088/1464-4258/11/9/094001 (2009).

34. Barnett, S. M. Rotation of electromagnetic fields and the nature of optical angular momentum. *Journal of Modern Optics* **57.** doi:10.1080/09500341003654427 (2010).

35. Cameron, R. P. & Barnett, S. M. Electric–magnetic symmetry and Noether's theorem. *New Journal of Physics* **14,** 123019. doi:10.1088/1367-2630/14/12/123019 (2012).

36. Bliokh, K. Y., Bekshaev, A. Y. & Nori, F. Dual electromagnetism: helicity, spin, momentum and angular momentum. *New Journal of Physics* **15.** doi:10.1088/1367-2630/15/3/033026 (2013).

37. Golat, S., Vernon, A. J. & Rodríguez-Fortuño, F. J. *The electromagnetic symmetry sphere: a framework for energy, momentum, spin and other electromagnetic quantities (preprint)* 2024. doi:https://doi.org/10.48550/arXiv.2405.15718.

38. Wei, L., Picardi, M. F., Kingsley-Smith, J. J., Zayats, A. V. & Rodríguez-Fortuño, F. J. Directional scattering from particles under evanescent wave illumination: the role of reactive power. *Optics Letters* **43,** 3393. doi:10.1364/OL.43.003393 (2018).

39. Picardi, M. F., Zayats, A. V. & Rodríguez-Fortuño, F. J. Janus and Huygens Dipoles: Near-Field Directionality Beyond Spin-Momentum Locking. *Physical Review Letters* **120,** 117402. doi:10.1103/PhysRevLett.120.117402 (2018).

40. Xu, X. & Nieto-Vesperinas, M. Azimuthal Imaginary Poynting Momentum Density. *Physical Review Letters* **123,** 233902. doi:10.1103/PhysRevLett.123.233902 (2019).

41. Zhou, Y. *et al.* Observation of high-order imaginary Poynting momentum optomechanics in structured light. *Proceedings of the National Academy of Sciences* **119.** doi:10.1073/pnas.2209721119 (2022).

42. Nieto-Vesperinas, M., Sáenz, J. J., Gómez-Medina, R. & Chantada, L. Optical forces on small magnetodielectric particle. *Optics Express* **18,** 11428. doi:10.1364/OE.18.011428 (2010).

43. Golat, S. *et al.* Optical dipolar chiral sorting forces and their manifestation in evanescent waves and nanofibers. *Physical Review Research* **6,** 023079. doi:10.1103/PhysRevResearch.6.023079 (2024).

44. Barnett, S. M. & Loudon, R. The enigma of optical momentum in a medium. *Philosophical Transactions of the Royal Society A: Mathematical, Physical and Engineering Sciences* **368,** 927–939. doi:10.1098/rsta.2009.0207 (2010).

45. Barnett, S. M. Resolution of the Abraham-Minkowski Dilemma. *Physical Review Letters* **104,** 070401. doi:10.1103/PhysRevLett.104.070401 (2010).

46. Partanen, M., Häyrynen, T., Oksanen, J. & Tulkki, J. Photon mass drag and the momentum of light in a medium. *Physical Review A* **95,** 063850. doi:10.1103/PhysRevA.95.063850 (2017).

47. Partanen, M. & Tulkki, J. Mass-polariton theory of light in dispersive media. *Physical Review A* **96,** 063834. doi:10.1103/PhysRevA.96.063834 (2017).

48. Pfeifer, R. N. C., Nieminen, T. A., Heckenberg, N. R. & Rubinsztein-Dunlop, H. Colloquium: Momentum of an electromagnetic wave in dielectric media. *Reviews of Modern Physics* **79,** 1197–1216. doi:10.1103/RevModPhys.79.1197 (2007).

49. Mansuripur, M. Resolution of the Abraham–Minkowski controversy. *Optics Communications* **283,** 1997–2005. doi:10.1016/j.optcom.2010.01.010 (2010).

50. Silveirinha, M. G. Reexamination of the Abraham-Minkowski dilemma. *Physical Review A* **96,** 033831. doi:10.1103/PhysRevA.96.033831 (2017).

51. Bliokh, K. Y., Bekshaev, A. Y. & Nori, F. Optical momentum and angular momentum in complex media: from the Abraham–Minkowski debate to unusual properties of surface plasmon-polaritons. *New Journal of Physics* **19.** doi:10.1088/1367-2630/aa8913 (2017).

52. Bliokh, K. Y., Bekshaev, A. Y. & Nori, F. Extraordinary momentum and spin in evanescent waves. *Nature Communications* **5.** doi:10.1038/ncomms4300 (2014).

53. Bliokh, K. Y., Kivshar, Y. S. & Nori, F. Magnetoelectric Effects in Local Light-Matter Interactions. *Physical Review Letters* **113.** doi:10.1103/PhysRevLett.113.033601 (2014).

54. Bliokh, K. Y. & Nori, F. Transverse and longitudinal angular momenta of light. *Physics Reports* **592,** 1–38. doi:10.1016/j.physrep.2015.06.003 (2015).

55. Barnett, S. M. & Berry, M. V. Superweak momentum transfer near optical vortices. *Journal of Optics* **15,** 125701. doi:10.1088/2040-8978/15/12/125701 (2013).

56. Berry, M. & Dennis, M. Polarization singularities in isotropic random vector waves. *Proceedings of the Royal Society of London. Series A: Mathematical, Physical and Engineering Sciences* **457,** 141–155. doi:10.1098/rspa.2000.0660 (2001).

57. Berry, M. V. & Shukla, P. Geometry of 3D monochromatic light: local wavevectors, phases, curl forces, and superoscillations. *Journal of Optics* **21.** doi:10.1088/2040-8986/ab14c4 (2019).

58. Antognozzi, M. *et al.* Direct measurements of the extraordinary optical momentum and transverse spin-dependent force using a nano-cantilever. *Nature Physics* **12,** 731–735. doi:10.1038/nphys3732 (2016).

59. John, H. P. The wave motion of a revolving shaft, and a suggestion as to the angular momentum in a beam of circularly polarised light. *Proceedings of the Royal Society of London. Series A, Containing Papers of a Mathematical and Physical Character* **82,** 560–567. doi:10.1098/rspa.1909.0060 (1909).

60. Cameron, R. P., Götte, J. B., Barnett, S. M. & Yao, A. M. Chirality and the angular momentum of light. *Philosophical Transactions of the Royal Society A: Mathematical, Physical and Engineering Sciences* **375,** 20150433. doi:10.1098/rsta.2015.0433 (2017).

61. Barnett, S. M. *et al.* On the natures of the spin and orbital parts of optical angular momentum. *Journal of Optics* **18.** doi:10.1088/2040-8978/18/6/064004 (2016).

62. O'Neil, A. T., MacVicar, I., Allen, L. & Padgett, M. J. Intrinsic and Extrinsic Nature of the Orbital Angular Momentum of a Light Beam. *Physical Review Letters* **88,** 053601. doi:10.1103/PhysRevLett.88.053601 (2002).

63. Bliokh, K. Y., Alonso, M. A., Ostrovskaya, E. A. & Aiello, A. Angular momenta and spin-orbit interaction of nonparaxial light in free space. *Physical Review A* **82,** 063825. doi:10.1103/PhysRevA.82.063825 (2010).

64. Bekshaev, A., Bliokh, K. Y. & Soskin, M. Internal flows and energy circulation in light beams. *Journal of Optics* **13.** doi:10.1088/2040-8978/13/5/053001 (2011).

65. Berry, M. V. *Paraxial beams of spinning light* in (ed Soskin, M. S.) (1998), 6–11. doi:10.1117/12.317704.

66. Zambrini, R. & Barnett, S. M. Quasi-Intrinsic Angular Momentum and the Measurement of Its Spectrum. *Physical Review Letters* **96,** 113901. doi:10.1103/PhysRevLett.96.113901 (2006).

67. Banzer, P. *et al.* The photonic wheel - demonstration of a state of light with purely transverse angular momentum. *Journal of the European Optical Society: Rapid Publications* **8.** doi:10.2971/jeos.2013.13032 (2013).

68. Neugebauer, M., Bauer, T., Aiello, A. & Banzer, P. Measuring the Transverse Spin Density of Light. *Physical Review Letters* **114,** 063901. doi:10.1103/PhysRevLett.114.063901 (2015).

69. Aiello, A., Banzer, P., Neugebauer, M. & Leuchs, G. From transverse angular momentum to photonic wheels. *Nature Photonics* **9,** 789–795. doi:10.1038/nphoton.2015.203 (2015).

70. Eismann, J. S. *et al.* Transverse spinning of unpolarized light. *Nature Photonics* **15.** doi:10.1038/s41566-020-00733-3 (2021).

71. Wang, H., Wojcik, C. C. & Fan, S. Topological spin defects of light. *Optica* **9,** 1417. doi:10.1364/OPTICA.474612 (2022).

72. Lipkin, D. M. Existence of a New Conservation Law in Electromagnetic Theory. *Journal of Mathematical Physics* **5.** doi:10.1063/1.1704165 (1964).

73. Bliokh, K. Y. & Nori, F. Characterizing optical chirality. *Physical Review A* **83.** doi:10.1103/PhysRevA.83.021803 (2011).

74. Nieto-Vesperinas, M. Optical torque: Electromagnetic spin and orbital-angular-momentum conservation laws and their significance. *Physical Review A* **92,** 043843. doi:10.1103/PhysRevA.92.043843 (2015).

75. Nieto-Vesperinas, M. Optical theorem for the conservation of electromagnetic helicity: Significance for molecular energy transfer and enantiomeric discrimination by circular dichroism. *Physical Review A* **92,** 023813. doi:10.1103/PhysRevA.92.023813 (2015).

76. Forbes, K. A. Optical helicity of unpolarized light. *Physical Review A* **105,** 023524. doi:10.1103/PhysRevA.105.023524 (2022).

77. Mackinnon, N. On the differences between helicity and chirality. *Journal of Optics* **21,** 125402. doi:10.1088/2040-8986/ab4db9 (2019).

78. Tang, Y. & Cohen, A. E. Optical Chirality and Its Interaction with Matter. *Physical Review Letters* **104.** doi:10.1103/PhysRevLett.104.163901 (2010).

79. Trueba, J. L. & Rañada, A. F. The electromagnetic helicity. *European Journal of Physics* **17,** 141–144. doi:10.1088/0143-0807/17/3/008 (1996).

80. Afanasiev, G. N. & Stepanovsky, Y. P. The helicity of the free electromagnetic field and its physical meaning. *Il Nuovo Cimento A* **109,** 271–279. doi:10.1007/BF02731014 (1996).

81. Freund, I. Bichromatic optical Lissajous fields. *Optics Communications* **226,** 351–376. doi:10.1016/j.optcom.2003.07.053 (2003).

82. Ayuso, D. *et al.* Synthetic chiral light for efficient control of chiral light–matter interaction. *Nature Photonics* **13.** doi:10.1038/s41566-019-0531-2 (2019).

83. Ayuso, D., Ordonez, A. F., Decleva, P., Ivanov, M. & Smirnova, O. Enantio-sensitive unidirectional light bending. *Nature Communications* **12.** doi:10.1038/s41467-021-24118-4 (2021).

84. Rego, L. & Ayuso, D. Structuring the local handedness of synthetic chiral light: global chirality versus polarization of chirality. *New Journal of Physics* **25,** 093005. doi:10.1088/1367-2630/acf150 (2023).

85. Sugic, D., Dennis, M. R., Nori, F. & Bliokh, K. Y. Knotted polarizations and spin in three-dimensional polychromatic waves. *Physical Review Research* **2,** 042045. doi:10.1103/PhysRevResearch.2.042045 (2020).

86. Angelsky, O. V., Mokhun, I. I., Bekshaev, A. Y., Zenkova, C. Y. & Zheng, J. Polarization singularities: Topological and dynamical aspects. *Frontiers in Physics* **11.** doi:10.3389/fphy.2023.1147788 (2023).

87. Kurzynowski, P., Woźniak, W. A. & Borwińska, M. Regular lattices of polarization singularities: their generation and properties. *Journal of Optics* **12,** 035406. doi:10.1088/2040-8978/12/3/035406 (2010).

88. Ruchi, Senthilkumaran, P. & Pal, S. K. Phase Singularities to Polarization Singularities. *International Journal of Optics* **2020** (ed Bernabeu, E.) 1–33. doi:10.1155/2020/2812803 (2020).

89. Nye, J. Lines of circular polarization in electromagnetic wave fields. *Proceedings of the Royal Society of London. A. Mathematical and Physical Sciences* **389.** doi:10.1098/rspa.1983.0109 (1983).

90. Nye, J. F. & V, H. J. The wave structure of monochromatic electromagnetic radiation. *Proceedings of the Royal Society of London. A. Mathematical and Physical Sciences* **409,** 21–36. doi:10.1098/rspa.1987.0002 (1987).

91. Dennis, M. Polarization singularities in paraxial vector fields: morphology and statistics. *Optics Communications* **213,** 201–221. doi:10.1016/S0030-4018(02)02088-6 (2002).

92. Alonso, M. A. Geometric descriptions for the polarization of nonparaxial light: a tutorial. *Advances in Optics and Photonics* **15,** 176. doi:10.1364/AOP.475491 (2023).

93. Rodríguez-Fortuño, F. J. *et al.* Near-Field Interference for the Unidirectional Excitation of Electromagnetic Guided Modes. *Science* **340,** 328–330. doi:10.1126/science.1233739 (2013).

94. Freund, I. Multitwist optical Möbius strips. *Optics Letters* **35,** 148. doi:10.1364/OL.35.000148 (2010).

95. Bauer, T. *et al.* Observation of optical polarization Möbius strips. *Science* **347,** 964–966. doi:10.1126/science.1260635 (2015).

96. Forbes, K. A. & Andrews, D. L. Spin-orbit interactions and chiroptical effects engaging orbital angular momentum of twisted light in chiral and achiral media. *Physical Review A* **99.** doi:10.1103/PhysRevA.99.023837 (2019).

97. Green, D. & Forbes, K. A. Optical chirality of vortex beams at the nanoscale. *Nanoscale* **15,** 540–552. doi:10.1039/D2NR05426D (2023).

98. Freund, I. Polarization singularity democracy: WYSIWYG. *Optics Letters* **29,** 1715. doi:10.1364/OL.29.001715 (2004).

99. Carozzi, T., Karlsson, R. & Bergman, J. Parameters characterizing electromagnetic wave polarization. *Physical Review E* **61,** 2024–2028. doi:10.1103/PhysRevE.61.2024 (2000).

100. Azzam, R. M. A. Three-dimensional polarization states of monochromatic light fields. *Journal of the Optical Society of America A* **28,** 2279. doi:10.1364/JOSAA.28.002279 (2011).

101. Hannay, J. H. The Majorana representation of polarization, and the Berry phase of light. *Journal of Modern Optics* **45,** 1001–1008. doi:10.1080/09500349808230892 (1998).

102. Bliokh, K. Y., Alonso, M. A. & Dennis, M. R. Geometric phases in 2D and 3D polarized fields: geometrical, dynamical, and topological aspects. *Reports on Progress in Physics* **82,** 122401. doi:10.1088/1361-6633/ab4415 (2019).

103. Berry, M. V. Index formulae for singular lines of polarization. *Journal of Optics A: Pure and Applied Optics* **6,** 675–678. doi:10.1088/1464-4258/6/7/003 (2004).

104. Dennis, M. R. Polarization singularity anisotropy: determining monstardom. *Optics Letters* **33,** 2572. doi:10.1364/OL.33.002572 (2008).

105. Forbes, K. A. & Jones, G. A. Measures of helicity and chirality of optical vortex beams. *Journal of Optics* **23,** 115401. doi:10.1088/2040-8986/ac24bd (2021).

106. Shen, Y. *et al.* Optical skyrmions and other topological quasiparticles of light. *Nature Photonics* **18,** 15–25. doi:10.1038/s41566-023-01325-7 (2023).

107. Barnett, S. M., Speirits, F. C. & Götte, J. B. On lines of constant polarisation in structured light beams. *Europhysics Letters* **143,** 35002. doi:10.1209/0295-5075/ace8b7 (2023).

108. McWilliam, A. *et al.* Topological Approach of Characterizing Optical Skyrmions and Multi-Skyrmions. *Laser & Photonics Reviews* **17.** doi:10.1002/lpor.202300155 (2023).

109. Nagaosa, N. & Tokura, Y. Topological properties and dynamics of magnetic skyrmions. *Nature Nanotechnology* **8,** 899–911. doi:10.1038/nnano.2013.243 (2013).

110. Mühlbauer, S. *et al.* Skyrmion Lattice in a Chiral Magnet. *Science* **323,** 915–919. doi:10.1126/science.1166767 (2009).

111. Yu, X. Z. *et al.* Real-space observation of a two-dimensional skyrmion crystal. *Nature* **465,** 901–904. doi:10.1038/nature09124 (2010).

112. Dennis, M. R., King, R. P., Jack, B., O'Holleran, K. & Padgett, M. J. Isolated optical vortex knots. *Nature Physics* **6.** doi:10.1038/nphys1504 (2010).

113. Larocque, H. *et al.* Reconstructing the topology of optical polarization knots. *Nature Physics* **14.** doi:10.1038/s41567-018-0229-2 (2018).

114. Li, P. *et al.* Optical vortex knots and links via holographic metasurfaces. *Advances in Physics: X* **6.** doi:10.1080/23746149.2020.1843535 (2021).

115. Afanasev, A., Kingsley-Smith, J. J., Rodríguez-Fortuño, F. J. & Zayats, A. V. Nondiffractive three-dimensional polarization features of optical vortex beams. *Advanced Photonics Nexus* **2,** 026001 (2023).

116. Mok, J. & Lee, H.-I. Degrees of circular polarization for the electromagnetic waves induced by electric point dipoles. *Optics Continuum* **1.** doi:10.1364/OPTCON.455018 (2022).

117. Spaegele, C. M. *et al.* Topologically protected optical polarization singularities in four-dimensional space. *Science Advances* **9.** doi:10.1126/sciadv.adh0369 (2023).

118. Betzig, E. *et al.* Imaging Intracellular Fluorescent Proteins at Nanometer Resolution. *Science* **313,** 1642–1645. doi:10.1126/science.1127344. eprint: https://www.science.org/doi/pdf/10.1126/science.1127344 (2006).

119. Rust, M. J., Bates, M. & Zhuang, X. Sub-diffraction-limit imaging by Stochastic Optical Reconstruction Microscopy (STORM). *Nature Methods* **3,** 793–796. doi:10.1038/nmeth929 (2006).

120. Novitsky, A. V. & Barkovsky, L. M. Poynting singularities in optical dynamic systems. *Physical Review A* **79,** 033821. doi:10.1103/PhysRevA.79.033821 (2009).

121. Tribelsky, M. I. & Rubinstein, B. Y. The Poynting Vector Field Generic Singularities in Resonant Scattering of Plane Linearly Polarized Electromagnetic Waves by Subwavelength Particles. *Nanomaterials* **12,** 3164. doi:10.3390/nano12183164 (2022).

122. Tribelsky, M. I. & Rubinstein, B. Y. Nature of the Poynting Vector Field Singularities in Resonant Light Scattering by Nanoparticles. *Nanomaterials* **12,** 1878. doi:10.3390/nano12111878 (2022).

123. Tribelsky, M. I. Effect of the Energy Conservation Law, Space Dimension, and Problem Symmetry on the Poynting Vector Field Singularities. *JETP Letters* **118,** 414–425. doi:10.1134/S0021364023601859 (2023).

124. Mokhun, I., Mokhun, A. & Viktorovskaya, Y. Singularities of the Poynting Vector and the Structure of Optical Fields. *Ukrainian Journal of Physical Optics* **7,** 129–141. doi:10.3116/16091833/7/3/129/2006 (2006).

125. Bekshaev, A. & Soskin, M. Transverse energy flows in vectorial fields of paraxial beams with singularities. *Optics Communications* **271,** 332–348. doi:10.1016/j.optcom.2006.10.057 (2007).

126. Mokhun, I., Galushko, Y., Viktorovskaya, Y., Karabchyivskyi, M. & Bekshaev, A. Transformations of the transverse Poynting vector distribution upon diffraction of a circularly polarized paraxial beam. *Journal of the Optical Society of America A* **41,** 382. doi:10.1364/JOSAA.514186 (2024).

127. Dennis, M. R., Hamilton, A. C. & Courtial, J. Superoscillation in speckle patterns. *Optics Letters* **33,** 2976. doi:10.1364/OL.33.002976 (2008).

128. Aiello, A. & Berry, M. V. Note on the helicity decomposition of spin and orbital optical currents. *Journal of Optics* **17,** 062001. doi:10.1088/2040-8978/17/6/062001 (2015).

129. Alpeggiani, F., Bliokh, K. Y., Nori, F. & Kuipers, L. Electromagnetic Helicity in Complex Media. *Physical Review Letters* **120,** 243605. doi:10.1103/PhysRevLett.120.243605 (2018).

130. Nieto-Vesperinas, M. & Xu, X. Reactive helicity and reactive power in nanoscale optics: Evanescent waves. Kerker conditions. Optical theorems and reactive dichroism. *Physical Review Research* **3,** 043080. doi:10.1103/PhysRevResearch.3.043080 (2021).

131. Du, L., Yang, A., Zayats, A. V. & Yuan, X. Deep-subwavelength features of photonic skyrmions in a confined electromagnetic field with orbital angular momentum. *Nature Physics* **15,** 650–654. doi:10.1038/s41567-019-0487-7 (2019).

132. Lim, S. W. D. *et al.* Point singularity array with metasurfaces. *Nature Communications* **14,** 3237. doi:10.1038/s41467-023-39072-6 (2023).

133. Vernon, A. J. & Rodríguez-Fortuño, F. J. Creating and moving nanoantenna cold spots anywhere. *Light: Science & Applications* **11.** doi:10.1038/s41377-022-00893-7 (2022).

134. Van Kruining, K. C., Cameron, R. P. & Götte, J. B. Superpositions of up to six plane waves without electric-field interference. *Optica* **5,** 1091–1098. doi:10.1364/OPTICA.5.001091 (2018).

135. Palik, E. D. & Ghosh, G. *Handbook of Optical Constants of Solids* (Academic Press, 1985).

136. Bharadwaj, P., Deutsch, B. & Novotny, L. Optical Antennas. *Advances in Optics and Photonics* **1,** 438. doi:10.1364/AOP.1.000438 (2009).

137. Giannini, V., Fernández-Domínguez, A. I., Heck, S. C. & Maier, S. A. Plasmonic Nanoantennas: Fundamentals and Their Use in Controlling the Radiative Properties of Nanoemitters. *Chemical Reviews* **111,** 3888–3912. doi:10.1021/cr1002672 (2011).

138. Maier, S. A. *Plasmonics: Fundamentals and Applications* doi:10.1007/0-387-37825-1 (Springer US, 2007).

139. Novotny, L. & Hecht, B. *Principles of Nano-Optics* doi:10.1017/CBO9780511794193 (Cambridge University Press, 2012).

140. Zito, G., Rusciano, G. & Sasso, A. Dark spots along slowly scaling chains of plasmonic nanoparticles. *Optics Express* **24,** 13584. doi:10.1364/OE.24.013584 (2016).

141. Haggui, M. *et al.* Spatial Confinement of Electromagnetic Hot and Cold Spots in Gold Nanocubes. *ACS Nano* **6,** 1299–1307. doi:10.1021/nn2040389 (2012).

142. Xia, J. *et al.* Turning a hot spot into a cold spot: polarization-controlled Fano-shaped local-field responses probed by a quantum dot. *Light: Science & Applications* **9,** 166. doi:10.1038/s41377-020-00398-1 (2020).

143. Tang, J. *et al.* Selective far-field addressing of coupled quantum dots in a plasmonic nanocavity. *Nature Communications* **9,** 1705. doi:10.1038/s41467-018-04077-z (2018).

144. Blascetta, N. P., Lombardi, P., Toninelli, C. & van Hulst, N. F. Cold and Hot Spots: From Inhibition to Enhancement by Nanoscale Phase Tuning of Optical Nanoantennas. *Nano Letters* **20,** 6756–6762. doi:10.1021/acs.nanolett.0c02607 (2020).

145. Shi, P., Du, L., Li, C., Zayats, A. V. & Yuan, X. Transverse spin dynamics in structured electromagnetic guided waves. *Proceedings of the National Academy of Sciences* **118.** doi:10.1073/pnas.2018816118 (2021).

146. Bekshaev, A. Y. Transverse spin and the hidden vorticity of propagating light fields. *Journal of the Optical Society of America A* **39,** 1577. doi:10.1364/JOSAA.466360 (2022).

147. Shi, P., Li, H., Du, L. & Yuan, X. Spin-Momentum Properties in the Paraxial Optical Systems. *ACS Photonics* **10,** 2332–2343. doi:10.1021/acsphotonics.2c01535 (2023).

148. Shi, P. *et al.* Dynamical and topological properties of the spin angular momenta in general electromagnetic fields. *Communications Physics* **6,** 283. doi:10.1038/s42005-023-01374-y (2023).

149. Cameron, R. P., Barnett, S. M. & Yao, A. M. Discriminatory optical force for chiral molecules. *New Journal of Physics* **16,** 013020. doi:10.1088/1367-2630/16/1/013020 (2014).

150. Hayat, A., Mueller, J. P. B. & Capasso, F. Lateral chirality-sorting optical forces. *Proceedings of the National Academy of Sciences* **112,** 13190–13194. doi:10.1073/pnas.1516704112. eprint: https://www.pnas.org/doi/pdf/10.1073/pnas.1516704112 (2015).

151. Yoo, S. & Park, Q.-H. *Nanophotonics* **8,** 249–261. doi:doi:10.1515/nanoph-2018-0167 (2019).

152. Fernandez-Corbaton, I. *Helicity and duality symmetry in light matter interactions: Theory and applications* PhD thesis (2014).

153. Wei, L. & Rodríguez-Fortuño, F. J. Momentum-Space Geometric Structure of Helical Evanescent Waves and Its Implications on Near-Field Directionality. *Physical Review Applied* **13,** 014008. doi:10.1103/PhysRevApplied.13.014008 (2020).

154. Kaiser, G. Helicity, polarization and Riemann–Silberstein vortices. *Journal of Optics A: Pure and Applied Optics* **6,** S243–S245. doi:10.1088/1464-4258/6/5/018 (2004).

155. Białynicki-Birula, I. On the Wave Function of the Photon. *Acta Physica Polonica A* **86,** 97–116 (1994).

156. Bialynicki-Birula, I. & Bialynicka-Birula, Z. Vortex lines of the electromagnetic field. *Physical Review A* **67,** 062114. doi:10.1103/PhysRevA.67.062114 (2003).

157. Philbin, T. G. Lipkin's conservation law, Noether's theorem, and the relation to optical helicity. *Physical Review A* **87,** 043843. doi:10.1103/PhysRevA.87.043843 (2013).

158. Vázquez-Lozano, J. E. & Martínez, A. Optical Chirality in Dispersive and Lossy Media. *Physical Review Letters* **121,** 043901. doi:10.1103/PhysRevLett.121.043901 (2018).

159. Tyldesley, J. *An Introduction to Tensor Analysis for Engineers and Applied Scientists* (Longman, 1975).

160. Kingsley-Smith, J. J. & Rodríguez-Fortuño, F. J. *Efficient post-processing of electromagnetic plane wave simulations to model arbitrary structured beams incident on axisymmetric structures* 2023. arXiv: 2302.04203.

161. Forbes, K. A. & Andrews, D. L. Orbital angular momentum of twisted light: chirality and optical activity. *Journal of Physics: Photonics* **3.** doi:10.1088/2515-7647/abdb06 (2021).

162. Andrews, D., Romero, L. & Babiker, M. On optical vortex interactions with chiral matter. *Optics Communications* **237.** doi:10.1016/j.optcom.2004.03.093 (2004).

163. Araoka, F., Verbiest, T., Clays, K. & Persoons, A. Interactions of twisted light with chiral molecules: An experimental investigation. *Physical Review A* **71.** doi:10.1103/PhysRevA.71.055401 (2005).

164. Barnett, S. M. Maxwellian theory of gravitational waves and their mechanical properties. *New Journal of Physics* **16.** doi:10.1088/1367-2630/16/2/023027 (2014).

165. Long, Y., Yang, C., Chen, H. & Ren, J. Universal Geometric Relations of Acoustic Spin, Energy Flux, and Reactive Power. *Physical Review Applied* **19,** 064053. doi:10.1103/PhysRevApplied.19.064053 (2023).

166. Bliokh, K. Y. & Nori, F. Spin and orbital angular momenta of acoustic beams. *Physical Review B* **99.** doi:10.1103/PhysRevB.99.174310 (2019).